Remote Sensing of Environment 301 (2024) 113875

Contents lists available at ScienceDirect

Remote Sensing of Environment

journal homepage: www.elsevier.com/locate/rse

Comprehensive accuracy assessment of long-term geostationary SEVIRI-MSG evapotranspiration estimates across Europe

Bagher Bayat *, Rahul Raj, Alexander Graf, Harry Vereecken, Carsten Montzka

Institute of Bio- and Geosciences: Agrosphere (IBG-3), Forschungszentrum Jülich GmbH, 52425 Jülich, Germany

ARTICLE INFO

Keywords:
ET
SEVIRI
Geostationary
Accuracy assessment
Heterogeneity analysis
Intercomparison
Europe

ABSTRACT

This study quantifies the accuracy of evapotranspiration (ET) estimates from the Spinning Enhanced Visible and Infrared Imager (SEVIRI) geostationary sensor onboard the Meteosat Second Generation (MSG) satellites, along seven key dimensions, i.e., diurnal cycle, daily, intra-annual, inter-annual, ecosystem, climate zone, and products intercomparison. In situ measurements were collected at 54 eddy covariance (EC) sites to evaluate the accuracy of SEVIRI actual ET products (diurnal and daily SEVIRI-ET_a) as well as reference ET (daily SEVIRI-ET_0) covering the period from 2004 to 2018 across Europe. SEVIRI-ET_a is produced by the Tiled ECMWF Surface Scheme of Exchange processes at the Land surface (TESSEL) model, while SEVIRI-ET_0 is estimated by a combination of a thermodynamically-based and an atmospheric boundary layer model. This evaluation is further separated according to the land cover heterogeneity of the SEVIRI pixels across all 54 EC sites, using MODIS land cover data. The Root Mean Squared Error (RMSE), along with the Kling-Gupta efficiency (KGE) and their respective decompositions, were employed to quantify the errors.

For diurnal SEVIRI-ET_a estimates, we found that the KGE (RMSE [mm $hour^{-1}$]) varied between −1.6 (0.04) to 0.8 (0.14), with a median value of 0.26 (0.07). Higher accuracy for diurnal SEVIRI-ET_a was obtained in the summer and during the mid-day time. For daily SEVIRI-ET_a, the KGE (RMSE [mm day^{-1}]) varied between −0.88 (0.43) to 0.93 (1.79), with a median value of 0.6 (0.77) and for daily SEVIRI-ET_0 the KGE (RMSE [mm day^{-1}]) varied between 0.51 (0.40) to 0.94 (1.50), with a median value of 0.77 (0.57). For daily SEVIRI-ET_a, intra-annual accuracy was low from January to March, increased in the mid-year, and then began to decline from November to December. Although accuracy remained relatively stable during the middle of the year, it varied considerably in the winter period. In the inter-annual dimension, the mid-year positive KGE values and distributions changed over time from 2004 to 2018. In spatial dimensions, the highest accuracy was in peat and grassland ecosystems, and the lowest in cropland ecosystem, with similar patterns observed in the boreal snow fully humid warm summer and warm temperate fully humid hot summer climate zones. Regarding SEVIRI-ET_0 results, similar to SEVIRI-ET_a, intra-annual accuracy was low in the first quarter of the year and the last one but high in the mid-year. In the inter-annual dimension, unlike SEVIRI-ET_a, almost an identical pattern was observed for the mid-year positive KGE values, demonstrating only a slight change in SEVIRI-ET_0 accuracy during 2004–2018. However, the highest accuracy was found in crop ecosystem, while the lowest was in forest ecosystem, reflecting similar trends in the warm temperate fully humid hot summer and warm temperate summer dry hot summer climate zones. The observed range of median RMSE changed between 0.4 and 1.5 mm day^{-1}, also suggests a reasonable accuracy for SEVIRI-ET estimates in all spatial domains.

Our results showed that the main trends in the accuracies (median KGEs) of SEVIRI-ET (both ET_a and ET_0) remained similar in separated homogeneous and heterogeneous sites and were comparable to combined sites among the dimensions. Through error decomposition, we discerned that SEVIRI-ET estimates performed particularly well in explaining inter-annual and spatial variabilities. Furthermore, the intercomparison of ET products revealed that SEVIRI satellite-derived ET_a exhibited the strongest correlation with in situ ET measurements across all ecosystem types and climate zones, outperforming other products (such as MODIS, PML, GLEAM, and BESS). The ET estimates from other products exhibited lower standard deviation errors and were in closer agreement with the in situ measurements. This study provides the first comprehensive evaluation of the

* Corresponding author.
E-mail addresses: b.bayat@fz-juelich.de, bagher.bayat@gmail.com (B. Bayat).

https://doi.org/10.1016/j.rse.2023.113875
Received 31 July 2023; Received in revised form 16 October 2023; Accepted 18 October 2023
Available online 5 December 2023
0034-4257/© 2023 The Authors. Published by Elsevier Inc. This is an open access article under the CC BY-NC-ND license (http://creativecommons.org/licenses/by-nc-nd/4.0/).

accuracy of SEVIRI diurnal and daily ET products across Europe, which may serve as a stimulus for further optimized selection of these products by potential users for various applications.

1. Introduction

Evapotranspiration (ET) is one of the main climate variables that connects energy, water, and carbon cycles. It is the sum of water evaporated from land surfaces, vegetation and water surfaces, and transpired by the vegetation canopy (Bayat et al., 2018; Hu et al., 2015a; Majozi et al., 2017). Accurate estimates of ET are, therefore, relevant for the study of climate change (meteorology and climatology), ecosystem functioning (ecology), food supply (agriculture), water balance (hydrology), and the interactions between water and ecological systems (ecohydrology). Due to high spatio-temporal variability, ET cannot be measured directly over large domains. Remote sensing spectral observations can overcome direct ET measurement challenges if used appropriately in ET algorithms and models, eventually resulting in spatio-temporal ET estimates. However, proper accuracy assessment and quantification of the errors associated with each ET algorithm and estimate are still challenging.

Widely-used algorithms implementing remotely-sensed optical and thermal observations include (but are not limited to): (i) energy balance (single- and dual-source) approach (Bastiaanssen et al., 1998; Kustas and Norman, 1999; Menenti, 1993; Norman et al., 1995; Su, 2002), (ii) trapezoid (also named triangle) feature space approach (Gallego-Elvira et al., 2013; Garcia et al., 2014; Jiang and Islam, 1999; Merlin et al., 2014; Nemani and Running, 1989; Nishida et al., 2003), (iii) relatively simple physically-based approach utilizing the Penman–Monteith (PM) (Dhungel et al., 2014; Ershadi et al., 2015; Westerhoff, 2015) and Priestley–Taylor (PT) models (Colaizzi et al., 2014; Priestley and Taylor, 1972; Szilagyi et al., 2014), and (iv) simplified empirical methods (Carlson et al., 1995; Glenn et al., 2010, 2007; Nagler et al., 2005; Seguin and Itier, 1983; Wang and Liang, 2008). The above-mentioned algorithms and their potentials and limitations are discussed in the remote sensing community (as reviewed by Glenn et al. (2007), Li et al. (2009), Liou and Kar (2014), Wang and Dickinson (2012), and Zhang et al. (2016)).

These algorithms have been adopted during the last decades to generate various ET global products from satellite data. Available long-term ET products generated from remote sensing observations and their key characteristics have been recently reviewed by Bayat et al. (2021). Among the available products, the Spinning Enhanced Visible and Infrared Imager (SEVIRI) sensor onboard the geostationary orbit Meteosat Second Generation (MSG) satellites provide two types of ET estimates; SEVIRI-actual ET (hereafter called SEVIRI-ET_a) and SEVIRI-reference ET (hereafter called SEVIRI-ET_0). SEVIRI-ET_a indicates the sum of water evaporated from soil, vegetation, and water surfaces, and water transpired from a vegetation canopy. SEVIRI-ET_0 is a kind of potential ET from a hypothetical well-watered green grass having 12 cm height and 0.23 albedo (Allen et al., 1998). SEVIRI-ET products are operationally available and are provided in near real-time at moderate spatial (0.05°) and very high (diurnal and daily) temporal resolutions covering the whole MSG field of view by the EUMETSAT Satellite Application Facility on Land Surface Analysis (LSA-SAF) (https://datalsasaf.lsasvcs.ipma.pt/PRODUCTS/; last access: 1 July 2023). These observation characteristics make SEVIRI an exciting, and ideal candidate for monitoring phenomena particularly in water resources that potentially evolve at a relatively moderate (seasonal cycle), to extremely rapid speed (diurnal cycle) over large (regional to continental) domains. For instance, SEVIRI-ET estimates have been employed for the purposes of sustainable water management (Petropoulos et al., 2016) and agricultural water stress detection (Bayat et al., 2022).

To estimate SEVIRI-ET_a, a simplified Soil-Vegetation-Atmosphere-Transfer (SVAT)-based Tiled ECMWF Surface Scheme of Exchange processes at the Land surface (TESSEL) model (Balsamo et al., 2009; van den Hurk et al., 2000) has been adopted (Ghilain et al., 2011, 2012, 2014). The TESSEL model was mainly fed with LSA-SAF SEVIRI products (i.e., the albedo, the downwelling surface shortwave, and longwave fluxes) and atmospheric model outputs (i.e., air and dew point temperature, humidity, wind speed, atmospheric pressure, and soil moisture). To obtain the SEVIRI-ET_0 estimate, a thermodynamically-based model (Schmidt, 1915) and an atmospheric boundary layer model (applied and evaluated by De Bruin (1983), Jacobs and De Bruin (1992), McNaughton and Spriggs (1986), Van Heerwaarden et al. (2010)) are combined (De Bruin et al., 2016). The combined model was fed with LSA-SAF SEVIRI products (i.e., daily global radiation and downwelling surface shortwave flux) and auxiliary information (i.e., air temperature) to first obtain daily net radiation over the (reference) grass surface and eventually calculate ET_0. Therefore, SEVIRI-ET_0 estimate is based on available radiative energy at the surface (Trigo et al., 2018). For more details information about the adopted methodology in SEVIRI-ET_a and SEVIRI-ET_0 estimates, the readers are referred to Ghilain et al. (2011) and De Bruin et al. (2016), respectively.

Dedicated efforts were made to quantify the accuracy of SEVIRI-ET (both ET_a and ET_0). For instance, a range of acceptable correlations was reported for various sites resulting from the comparison between SEVIRI-ET and in situ ET at hourly time steps in Europe (Ghilain et al., 2011). A further validation exercise, designed to assess the quality of half-hourly SEVIRI-ET_a over 16 sites in Europe distributed in different types of land cover, showed a high correlation for most of the investigated sites, and error values remained within the range of observations uncertainty (Gellens-Meulenberghs et al., 2012). The direct comparison of daily SEVIRI-ET_a and in situ ET_a at six sites in Spain and Italy in 2011 demonstrated a close agreement among all sites (Petropoulos et al., 2015). Moreover, direct validation of SEVIRI-ET_a at daily time steps was initially conducted by EUMETSAT as part of their product development. In situ measurements of ET_a were selected from 48 different sites across Europe and Africa from March 2007 to December 2011. Acceptable accuracy was reported in this validation exercise for SEVIRI-ET_a (Ghilain et al., 2018).

Further, the Penman-Monteith estimated ET_0 was compared to measured ET_0 at the Cabauw grassland site in the Netherlands from 2007 to 2012 (Trigo et al., 2018). The results showed fair agreement between the Penman-Monteith calculated ET_0 and measured ET_0 at Cabauw grass site. A similar strategy was adopted in the EUMETSAT initial validation of SEVIRI-ET_0. The direct validation has been performed by comparison of SEVIRI-ET_0 and local ET_a measurements, mainly in Cabauw, where local measurements of ET_a were considered identical to ET_0 in this site from 2007 to 2012. Their results demonstrated a good agreement between SEVIRI-ET_0 and measured ET_a (which corresponds to ET_0) at Cabauw site (Trigo and DeBruin, 2016).

In the studies described above, the errors associated with SEVIRI-ET were quantified mostly for *old versions* using *limited* in situ measurements independent of site *representativeness* (*heterogeneity analysis*). The new version of SEVIRI-ET estimates at diurnal (sub-daily) and daily steps has just been released (in March 2023) and made available (https://datalsasaf.lsasvcs.ipma.pt/PRODUCTS/; last access: 1 July 2023). However, it is still unclear whether the accuracy of *new* (i.e., *version 3*) *diurnal and daily* products is stable, whether *additionally* available measurements can be used in the assessment, whether 8-day SEVIRI-ET_a performance is *comparable* to widely-used global open-access satellite ET products, and whether the *representativeness* of the in situ sites can affect the accuracy analysis results. Moreover, in most of the previous studies, the SEVIRI-ET accuracies were quantified mainly for a few land cover types. For instance, in the original validation report of SEVIRI-ET_a,

grouping the accuracy results by land cover type, which was performed regardless of the climate and the vegetation fraction, was pointed out as one of the key SEVIRI-ET_a validation limitations (Ghilain et al., 2018).

There is still strong interest in: (i) separating the accuracy of SEVIRI-ET_a and SEVIRI-ET_0 into temporal (intra-annual and inter-annual) and spatial (ecosystem, and climate zones) dimensions, to provide valuable insight into the seasonal, environmental, and climatic conditions leading to stronger (poorer) accuracy, and (ii) conducting an intercomparison between the SEVIRI-ET_a and widely-used existing open access satellite ET products (e.g., MODIS, PML, GLEAM, and BESS) to assess the performance of such satellite ET estimates with in situ measurements across various ecosystem types and climate zones to gain a better understanding of the products (dis)similarities and accuracy. This contribution is required to understand the strengths and weaknesses of the products. Although the main aim of such accuracy assessment of satellite products is usually to inform potential users about the product uncertainty, the modelers can additionally benefit from the results, for instance, by revisiting their underlying models assumptions and parametrization and pave the way for further improvements both in the models and final SEVIRI-ET estimates. The current study is focused particularly on these aspects, in detail, aiming to answer key questions: (i) how does overall diurnal and daily SEVIRI-ET accuracy varies among the sites? (ii) how does the daily SEVIRI-ET accuracy vary along the year (intra-annual dimension) and between years (inter-annual dimension)? (iii) can we observe differences in daily SEVIRI-ET accuracy between the sites considering different ecosystems, and different climate zones? (iv) is the performance of SEVIRI ET_a estimate comparable to other widely-used relevant satellite ET products? and (v) how is the accuracy assessment of SEVIRI-ET affected by the site heterogeneity, and are the results comparable among the separated (homogeneous and heterogeneous) sites?

The main objectives of the current study are: (i) to perform an extensive accuracy assessment of diurnal and daily SEVIRI-ET_a and daily SEVIRI-ET_0 products against in situ measurements at 54 Eddy Covariance (EC) sites across Europe between 2004 and 2018, (ii) to separate the SEVIRI-ET product accuracy into temporal (intra-annual and inter-annual) and spatial (ecosystem, and climate zones) dimensions across Europe, (iii) to compare SEVIRI-ET_a products with four global ET products, i.e., MODIS, PML, GLEAM, BESS, which are freely available for users, and (iv) to perform homogeneity (heterogeneity) analysis of SEVIRI-ET pixels surrounding the in situ sites to understand the representativeness of the site and whether the errors are comparable among the homogeneous and heterogeneous pixels.

2. Data

2.1. SEVIRI Satellite ET data set

All available diurnal (sub-daily) and daily SEVIRI-ET_a and daily SEVIRI-ET_0 data from January 2004 to December 2018 were selected for this study (Table 1). These time-series data are published by LSA SAF with specific names of METv3, MDMETv3, and METREF, respectively.

Table 1
SEVIRI ET satellite observations utilized in this study and their main characteristics.

ET Products	LSA SAF products	Temporal resolution	Number of observations	Temporal coverage
SEVIRI-ET_a	METv3	diurnal (sub-daily)	257,506	21/01/2004 to 31/12/2018
SEVIRI-ET_a	MDMETv3	daily	5412	
SEVIRI-ET_0	METREF	daily	5413	

The data is available in standard Hierarchical Data Format (HDF) and network Common Data Form (netCDF) files (https://datalsasaf.lsasvcs.ipma.pt; last access: 1 July 2023). All three datasets of SEVIRI-ET covered the full MSG disk area (i.e., Europe, Africa, and the eastern part of South America).

In total, 257,506 diurnal SEVIRI-ET_a images and 10,825 daily images (i.e., 5413 SEVIRI-ET_0 and 5412 SEVIRI-ET_a) were analyzed in this study. All the available images collected for the period 2004 to 2018 were used for the accuracy assessment. Processing of SEVIRI-ET satellite data was conducted using the R software program version 3.6.3 (R Core Team, 2020) using relevant packages (see acknowledgment section). SEVIRI-ET data are distributed at 0.05° spatial resolutions. Four samples of the diurnal SEVIRI-ET_a dataset are shown for the MSG disk in Fig. 1 to present an example of the diurnal cycle of ET_a on 15 July 2015.

Further, two sample data sets of daily SEVIRI-ET_0 and SEVIRI-ET_a in 2016 and 2018 are presented for the MSG disk global coverage in Fig. 2 to show the daily variation of ET_0 and ET_a.

2.2. In situ measurements

This study used EC measurements from 54 sites to obtain both diurnal and daily time series of in situ ET_a and calculate in situ ET_0 from 2004 to 2018. The distribution of these sites across Europe is shown in Fig. 3, and their essential characteristics are listed in Table A1 of the Appendix.

As shown in Fig. 3, these EC sites are spread across the European continent. More information about the in situ ET_a and ET_0 measurements and processing are provided in the methods section (section 3.1).

2.3. MODIS land cover data

MODIS land cover data were used in this study to extract land cover fractions of SEVIRI pixels from the EC sites to perform pixel homogeneity analysis. Land cover data for 2016 at 0.004° resolution (Fig. 4a and Table 2) was obtained for the whole of Europe from the global products (MCD12Q1 V6). The land cover product has six classification schemes derived from supervised classifications of MODIS Terra and Aqua spectral data. This study used the classification scheme number six (land cover type six). More information about the MCD12Q1 V6 product can be found at (https://developers.google.com/earth-engine/datasets/catalog/MODIS_006_MCD12Q1; last access: 1 July 2023).

2.4. Climate zone data

This study utilized the reanalysed Köppen-Geiger climate map (Rubel et al., 2017) to extract the climate dimension information for 54 EC sites. This map is the updated version (2017) of the widely-used climate classification map by Wladimir Köppen and Rudolf Geiger presented in 1961. The re-analyzed Köppen-Geiger climate data has global coverage with a higher resolution of 5 arc minutes generated through downscaling algorithms. More information about the re-analyzed Köppen-Geiger climate map data can be found at (http://koeppen-geiger.vu-wien.ac.at/present.htm; last access: 1 July 2023). The extracted climate zone data for Europe is shown in Fig. 4b, and its key characteristics are summarized in Table 3.

2.5. Ecosystem data

Ecosystem dimension information for all EC sites was collected from site principal investigators and the opinions reflected in recent literature. A simplified four-type (forest, grassland, cropland, and peatland) classification of the ecosystems was used for this study, similar to Graf et al. (2020).

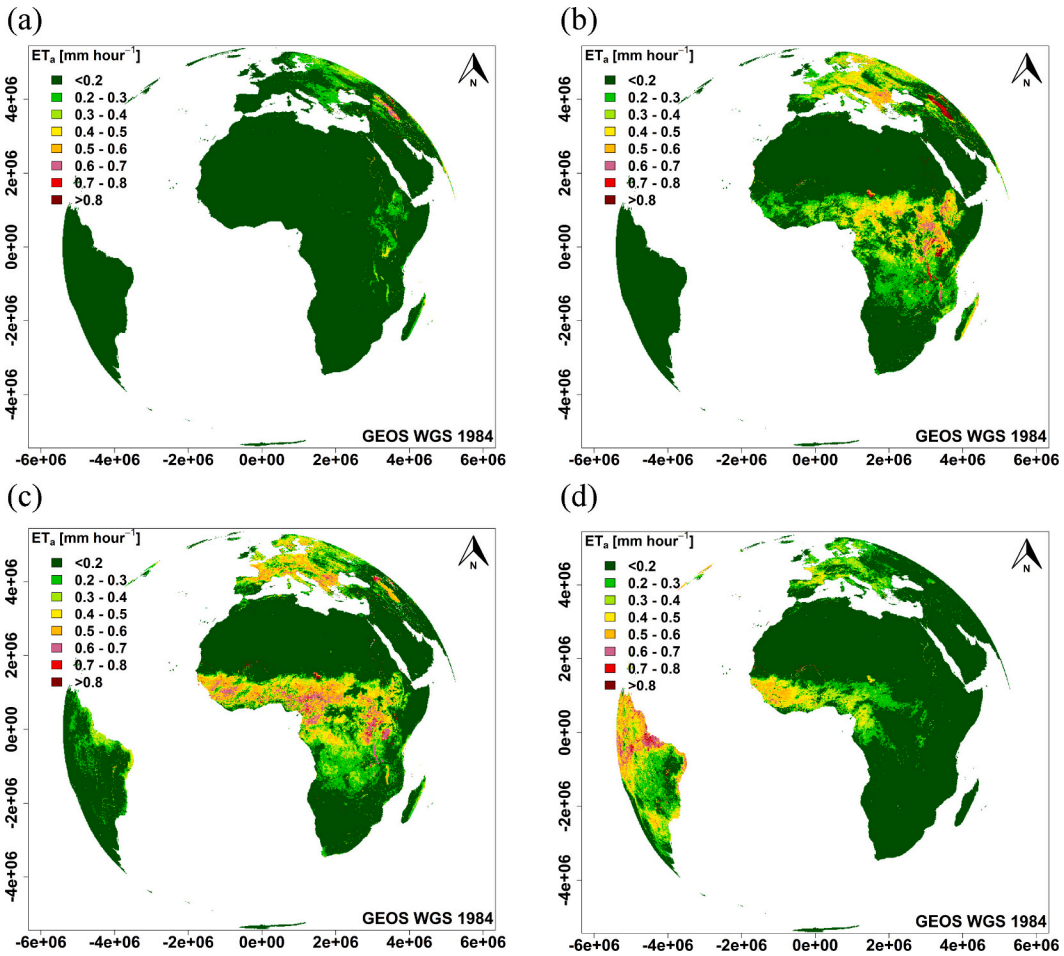

Fig. 1. Diurnal cycle (Sub-daily) SEVIRI-ET$_a$ sample data set on 15 July 2018 with MSG disk global coverage; (a) at 06:00, (b) 09:00, (c) 12:00, (d) 15:00.

2.6. Global satellite ET$_a$ products

Four global ET products were explored in this study beside SEVIRI-ET$_a$ to analyze their performances for the period of 2004 to 2018. Selected ET products are: Moderate Resolution Imaging Spectroradiometer (MODIS) v6 [also known as MOD16A2] (Mu et al., 2011; Running et al., 2021), the Penman-Monteith-Leuning (PML) v2 (Zhang et al., 2019), the Global Land Evaporation Amsterdam Model (GLEAM) v3.7b (Martens et al., 2017; Miralles et al., 2011), and the Breathing Earth System Simulator (BESS) v2 (Li et al., 2023). The main characteristics of these ET products are summarized in Table 3.

MODIS ET v6 product, which has been created by means of the Penman-Monteith approach (Running et al., 2021), is available for the public at the 8-day temporal resolution, 500 m spatial resolution and spans from 2001 until now. This product is provided by NASA Land Processes Distributed Active Archive Center (LP DAAC) at the United States Geological Survey (USGS) Earth Resources Observation and Science (EROS) center and is available at (https://doi.org/10.5067/MODIS/MOD16A2.006; last access: 1 July 2023). MODIS ET product can also be accessed from Earth Engine Data Catalog (https://developers.google.com/earth-engine/datasets/catalog; last access: 1 July 2023) with the Earth Engine Snippet: ee.ImageCollection ("MODIS/061/MOD16A2").

PML ET v2 product is based on Penman-Monteith approach in which a water-carbon coupled canopy conductance model has been employed to estimate canopy transpiration (Zhang et al., 2019). PMLv2 product is available at 500 m spatial and 8-day temporal resolutions covering the period from 2002 to 2020. PML ET v2 product can be accessed from Earth Engine Data Catalog with the Earth Engine Snippet: ee.ImageCollection ("CAS/IGSNRR/PML/V2_v017").

The GLEAM ET v3.7b is produced by means of an algorithm that estimates ET sub-components (i.e., transpiration, interception loss, bare soil evaporation, snow sublimation, and open-water evaporation) separately (Martens et al., 2017; Miralles et al., 2011). Priestley-Taylor has been utilized to estimate potential ET, which later was converted to actual ET by making use of the multiplicative, evaporative stress factor. The stress factor is a function of microwave vegetation optical depth, as a proxy of vegetation water content and simulations of soil moisture at the root zone. The Gash analytical model of rainfall interception has been adopted for interception loss calculation. The GLEAM ET v3.7b data is published at 0.25° spatial and daily temporal resolutions spanning from 2003 until 2022 and can be obtained from GLEAM sever (www.gleam.eu; last access: 1 July 2023).

The BESSv2 ET product is based on an improved process-based coupled model, i.e., BESS, in which a newly developed ecosystem respiration module, and an optimality-based maximum carboxylation rate model are integrated (Li et al., 2023). The BESSv2 data is available for the public at the daily temporal resolution, 0.05° spatial resolution, and spans from 1982 until 2019. This product is provided by the data provider and is available at (https://www.environment.snu.ac.kr/bessv2; last access: 1 July 2023).

It should be noted that MOD16A2 and PML datasets are downloaded from Earth Engine Data Catalog, while the GLEAM and BESS products are obtained from their providers.

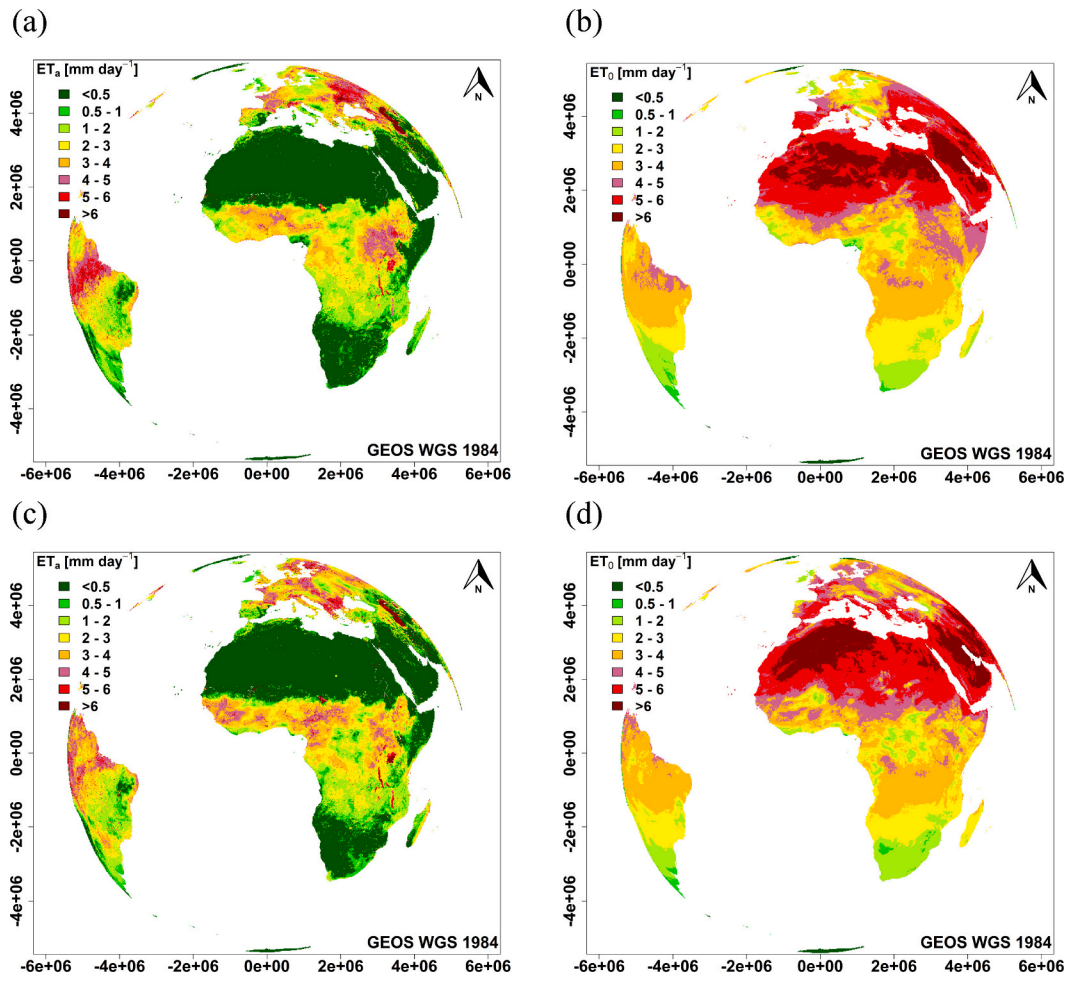

Fig. 2. SEVIRI-ET_a (left panels) and SEVIRI-ET_0 (right panels) sample data set in 2016 and 2018 with MSG disk global coverage; (a) SEVIRI-ET_a on 15 July 2016, (b) SEVIRI-ET_0 on 15 July 2016, (c) SEVIRI-ET_a on 15 July 2018, (d) SEVIRI-ET_0 on 15 July 2018.

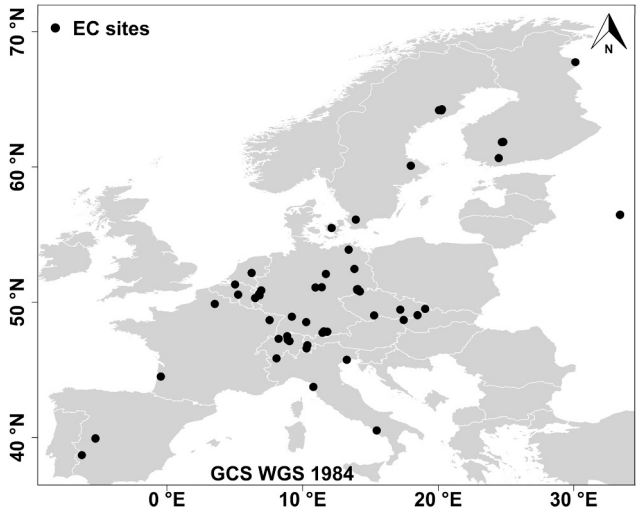

Fig. 3. The spatial distribution of Eddy-Covariance (EC) sites used in this study.

3. Methods

3.1. *In situ ET_a and ET_0 estimates*

The in situ ET_0 and ET_a datasets are identical to the ones used by Graf et al. (2020), except for filtering out all site-years before 2011, to match the temporal extent of the SEVIRI dataset. In-situ ET_a data are based on raw turbulence measurements at the EC sites (resolution 10 or 20 s^{-1}), which each individual site operator used to compute half-hourly fluxes, including the latent heat flux using state-of-the-art protocols (Franz et al., 2016; Mauder et al., 2013), and provided in the framework of the networks TERENO (www.tereno.net; last access: 1 July 2023) and ICOS (www.icos-ri.eu; last access: 1 July 2023). To fill data gaps in ET_a, we used its statistical relation to ET_0 (Fischer et al., 2013; Graf et al., 2014; Sun et al., 2010), which, however, varies with location and time. Beginning with the first data point of the time series of a station, a window was varied in length between 2880 and 5760 (corresponding to 60 and 120 days of half-hourly data) until the RMSE of ET_a predicted from ET_0 by regression through the origin became minimal. This procedure was repeated for the rest of the time series and independently for all stations. A particular issue in using EC ET_a as a reference for model or remote sensing-based ET_a is the energy balance closure problem, where less than the available energy from radiation and ground heat flux is found in the sum of sensible and latent heat EC fluxes, which may or may not indicate an underestimation of EC-based ET_a. For the dataset used here, Graf et al. (2020) found a closure gap, which may serve as a rough indicator of the potential underestimation of 19% to 23%, however in good agreement with global long-term studies (Stoy et al., 2013; Wilson et al., 2002). Due to the ongoing debate on the origin and partitioning between e.g., latent and sensible heat flux of this closure gap, ET_a presented here was not subject to an attempt to correct energy balance closure.

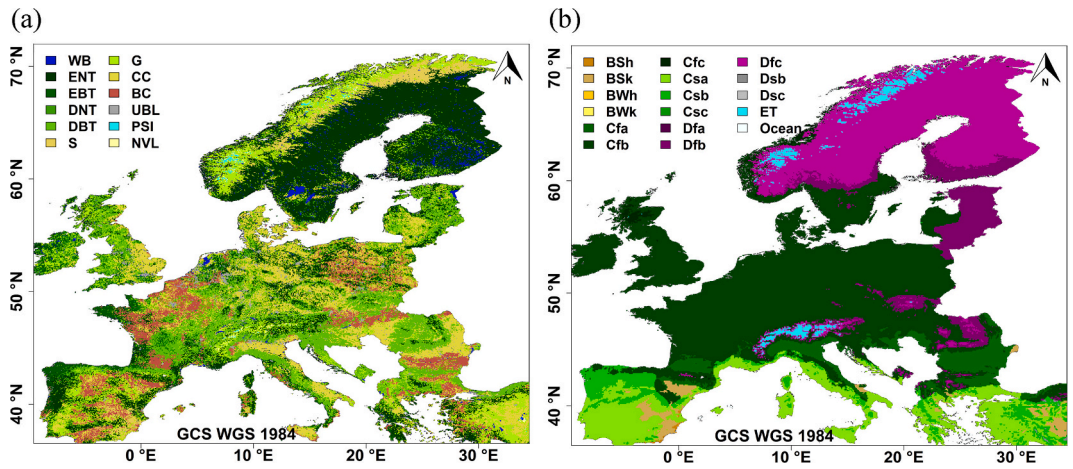

Fig. 4. (a) European land cover data (land cover type six) in 2016 from MODIS global land cover at 500 m resolution (MCD12Q1 V6 product), and (b) European re-analyzed Köppen-Geiger climate data version 2017 extracted from global re-analyzed Köppen-Geiger at five arc minutes resolution. The map legend is described in Table A1 and A2 of the Appendix.

Table 2
Additional data products utilized in this study and their main characteristics.

Product	Theme	Version	Spatial resolution
MCD12Q1 V6	land cover	2016	0.004°
Köppen-Geiger	climate	2017	5 arc minutes

Table 3
Characteristics of global ET products used in this study.

Product	Openly accessible	Temporal coverage	Spatial resolution	Temporal resolution
MOD16A2	Yes	2001-now	500 m	8-day
PMLv2	Yes	2002–2020	500 m	8-day
GLEAM v3.7b	Yes	2003–2022	0.25°	daily
BESS v2	Yes	1982–2019	0.05°	daily

In situ ET_0 was calculated using the Penman-Monteith approach from locally measured meteorological data from the 54 EC sites following the "FAO-56" (Allen et al., 1998) definition for a hypothetical grass reference surface. The meteorological input data for this can also be subject to occasional data gaps, albeit to a lesser extent then ET_a, which requires appropriate micrometeorological conditions for valid measurements. To enable the computation of continuous ET_0 series and thus also the filling of ET_a, such meteorological input data gaps were first filled with proven methods. For the majority of sites provided through the ICOS drought 2018 task force (https://doi.org/10.18160/YVR0-4898, last access: 1 July 2023), meteorological data were filled according to (Pastorello et al., 2020). For some sites (BE-Lon and Vie, DE-BER, EC2, EC4, Fen, Gri, HoH, Kli, Rbw, RuR, RuS, RuW, SfS, Tha, ZRK, FR-EM2 and Hes), meteorological data were filled by the authors. When and where possible, nearby stations were used with an adapted version (Graf, 2017) of the DINEOF method (Beckers and Rixen, 2003); all remaining meteorological gaps were filled with the REddyProc software (Wutzler et al., 2018).

3.2. SEVIRI satellite pixel homogeneity analysis

Quantifying SEVIRI pixel homogeneity can indicate the land cover similarity within the pixel and therefore examine the representativeness of water fluxes measured in a specific pixel. We analyzed the land cover similarity for all SEVIRI pixels surrounding EC flux towers using 0.004° MODIS 2016 land cover data. The fraction of every land cover type within the SEVIRI pixel was calculated, and pixel purity was defined as the fraction of the most dominant land cover type. The key criteria for analyzing the pixel homogeneity were adopted from Martínez et al. (2020); (1) those pixels that include more than two natural land cover types or those with purity index value lower than 65% were considered heterogeneous, (2) the pixel purity value of 65% was defined as the minimum required purity for the site homogeneity in case of two land cover types being present within the pixel, and (3) those pixels with pixel purity values higher than 80% were directly assumed homogeneous. After applying the described criteria, we revisited the outcome of the analysis, particularly for homogeneous sites, to ensure that the MODIS-derived land cover types agree well with the actual reported ecosystem type of the sites. In case of disagreement, we reclassified that particular site from homogeneous to heterogeneous.

Additionally, we compared our land cover heterogeneity results with the widely-used Gini-Simpson Index (GSI; Simpson, 1949) for diversity to understand the link between these two methods. The GSI has been calculated based on land cover types from the MODIS-derived land cover dataset as follows:

$$GSI = 1 - \sum_i p_i^2 \quad (1)$$

where p_i represents the proportion of SEVIRI pixels belonging to MODIS class i and GSI denotes the heterogeneity proxy for the SEVIRI pixels. The value of GSI ranges between 0 and 1. GSI = 0 indicates no diversity, while GSI = 1 suggests a great diversity in the landscape.

3.3. Dimensions information extraction for EC sites

The climate zone dimensions information for all 54 EC site locations were extracted directly from the climate zone map (Fig. 4b). Moreover, for intra-annual and inter-annual dimensions, changes in the accuracy of SEVIRI-ET products were investigated within the year and between the years in two ways; (1) the variations of SEVIRI-ET errors were captured from 2004 to 2018 by visualizing the time series of selected error statistics, (2) the total error statistics were decomposed into spatial and temporal components to identify the pure spatial and temporal accuracies. In the same way, a partial error statistic was computed for each dimension by removing the variability along the other dimensions.

3.4. SEVIRI satellite data set accuracy assessment

Evaluation of earth observation products allows quantifying and understanding errors, making users aware of potential implications for

various applications (Jia et al., 2010; Petropoulos et al., 2015). Without sufficient validation, results derived from earth observation may not be credible and will cause further challenges when used for monitoring purposes (Bayat et al., 2021; Glenn et al., 2011; Mu et al., 2011). In this study, a point-by-point validation approach was used to evaluate the accuracy of diurnal and daily SEVIRI-ET_a and daily SEVIRI-ET_0 from 2004 to 2018 against in situ ET_a and ET_0 in 54 sites across Europe.

Kling-Gupta efficiency (KGE) and Root Mean Square Error (RMSE) statistics were employed to evaluate SEVIRI-ET_a and SEVIRI-ET_0 products against measured ET_a and ET_0.

KGE considers a balanced optimization of product bias, variability, and temporal fit to quantify the error efficiently (Gupta et al., 2009). KGE and RMSE are calculated as follows:

$$\mathrm{KGE} = 1 - \sqrt{(r-1)^2 + \left(\frac{\sigma_s}{\sigma_g} - 1\right)^2 + \left(\frac{\mu_s}{\mu_g} - 1\right)^2} \tag{2}$$

$$\mathrm{RMSE} = \sqrt{\frac{1}{n}\sum_{i=1}^{n}(g_i - s_i)^2} \tag{3}$$

where r is the linear correlation between in situ ET (ground) measurements and SEVIRI-ET (satellite) observations, σ_s the standard deviation in satellite observations, σ_g the standard deviation in ground measurements, μ_s the satellite mean, and μ_g the ground mean. The ratios σ_s/σ_g and μ_s/μ_g describe the variability error and the bias term, which are also called α and β, respectively. The g_i and s_i are the ground measurements and satellite observations, i is the sampling time step, and n is the number of samples (n = 5412 (for daily ET_a), 5413 (for daily ET_0), 257,506 (for diurnal ET_a).

The optimal values of KGE and RMSE are 1 and 0, respectively. KGE = 1 indicates a perfect match between ground measurements and satellite observations. Positive KGE values are considered "good", whereas negative KGE values are labeled as "bad" matches. However, it is shown that $-0.41 < \mathrm{KGE} \leq 1$ can be considered as reasonable performance, and KGE = 0.3 as a threshold for behavioural simulations/estimations (Knoben et al., 2019). Moreover, low values of RMSE indicate high accuracy of the observations. We consider both KGE and RMSE because the latter provides an absolute measure of performance, and KGE a relative measure of performance.

The overall error statistics (KGE and RMSE) for all 54 sites were calculated based on in situ measurements and SEVIRI-ET observations at diurnal and daily steps. This resulted in one set of RMSE and KGE for each site. Such overall error statistics were refined in a further step to means for each ecosystem types, and climate zones. Moreover, to quantify the accuracy at the temporal domain, the time-series of KGE and RMSE was calculated for all individual sites at monthly time steps in the time series (2004–2018). This resulted in monthly time series of KGE and RMSE for all 54 sites under investigation. For the inter-annual dimension accuracy assessment, the mean of KGE and RMSE of all sites were calculated for each month (therefore, we obtained 15 [years] × 12 [months] values for each of KGE and RMSE). By grouping these means for the same months across the time series, we obtained the median intra-annual KGE and RMSE. It should be added that for the error statistics calculations, we always filtered out all rows in the dataset that had at least one missing value either at in situ measurement records or SEVIRI-ET estimates.

In addition to the overall and the time series of error statistics described above, an additional KGE and RMSE were calculated for each dimension by decomposing the data into their spatial and temporal variability. This also enabled to further decompose the latter into a purely spatial, annual, and intra-annual KGE and RMSE. To calculate pure spatial and temporal KGE and RMSE, first, we computed the mean ET over the whole time series for each site (Eq. 4 to 12 [we show the equations only for KGE here]) and used it as input to the RMSE and KGE equations (Eq. 2 and 3) to obtain a purely spatial metric. Second, a total RMSE and KGE were calculated by making use of all the individual in situ and satellite data from all the stations (Eq. 13 to 15) into the RMSE and KGE equations. Third, we removed the means (obtained in the first step) from the original data (Eq. 16 and 17) and used such time series (i.e., g_{ij}^1 and s_{ij}^1) to compute a purely temporal RMSE and KGE by the same sets of questions used in the step 2 (Eq. 13 to 15). Fourth, we aggregated the time series with site means removed to annual averages for the inter-annual metrics (Eq. 18 and 19), and removed them (Eq. 20 and 21) to get an intra-annual metric, once again by making use of Eq. 13 to 15 and finally, we fed the data into Eq. 2 and 3. In other words, the time series of the input data were used to compute site means on the one hand and the deviations from those (or the input data with the site means removed) on the other hand. Each of the resulting datasets was used like an original dataset to calculate one KGE and RMSE for the corresponding dimension.

$$\mu_{gj} = \frac{1}{n}\sum_{i=1}^{n} g_{ij} \qquad i = 1,2,\ldots,n \qquad j = 1,2,\ldots,m \tag{4}$$

$$\mu_{sj} = \frac{1}{n}\sum_{i=1}^{n} s_{ij} \tag{5}$$

$$\sigma_{gj} = \sqrt{\frac{1}{n}\sum_{i=1}^{n}\left(g_{ij} - \mu_{gj}\right)^2} \tag{6}$$

$$\sigma_{sj} = \sqrt{\frac{1}{n}\sum_{i=1}^{n}\left(s_{ij} - \mu_{sj}\right)^2} \tag{7}$$

$$\mu_g = \mu\left(\mu_{g1}, \mu_{g2}, \ldots, \mu_{gm}\right) \tag{8}$$

$$\mu_s = \mu\left(\mu_{s1}, \mu_{s2}, \ldots, \mu_{sm}\right) \tag{9}$$

$$\sigma_g = \sigma\left(\sigma_{g1}, \sigma_{g2}, \ldots, \sigma_{gm}\right) \tag{10}$$

$$\sigma_s = \sigma\left(\sigma_{s1}, \sigma_{s2}, \ldots, \sigma_{sm}\right) \tag{11}$$

$$r = \frac{\sum_{j=1}^{m}\left(\mu_{gj} - \mu_g\right)\left(\mu_{sj} - \mu_s\right)}{\sqrt{\sum_{j=1}^{m}\left(\mu_{gj} - \mu_g\right)^2 \sum_{j=1}^{m}\left(\mu_{sj} - \mu_s\right)^2}} \tag{12}$$

$$\sigma_g = \sqrt{\frac{1}{m \times n}\sum_{i=1}^{n}\sum_{j=1}^{m}\left(g_{ij} - \mu_g\right)^2} \tag{13}$$

$$\sigma_s = \sqrt{\frac{1}{m \times n}\sum_{i=1}^{n}\sum_{j=1}^{m}\left(s_{ij} - \mu_s\right)^2} \tag{14}$$

$$r = \frac{\sum_{i=1}^{n}\sum_{j=1}^{m}\left(g_{ij} - \mu_g\right)\left(s_{ij} - \mu_s\right)}{\sqrt{\sum_{i=1}^{n}\sum_{j=1}^{m}\left(g_{ij} - \mu_g\right)^2 \sum_{i=1}^{n}\sum_{j=1}^{m}\left(s_{ij} - \mu_s\right)^2}} \tag{15}$$

$$g_{ij}^1 = g_{ij} - \mu_{gj} \tag{16}$$

$$s_{ij}^1 = s_{ij} - \mu_{sj} \tag{17}$$

$$g_{yj} = \frac{1}{N}\sum_{1}^{N} g_{ijy}^1 \qquad g_{ijy}^1 \subset g_{ij}^1 \qquad N = 1,2,\ldots,365\ (366) \qquad y = 1,2,\ldots,15 \tag{18}$$

$$s_{yj} = \frac{1}{N}\sum_{1}^{N} s_{ijy}^1 \qquad s_{ijy}^1 \subset s_{ij}^1 \tag{19}$$

$$g_{ij}^{2} = g_{ijy}^{1} - g_{yj} \quad (20)$$

$$s_{ij}^{2} = s_{ijy}^{1} - s_{yj} \quad (21)$$

where i is the sampling time step (similar to Eq. 3), j is the number of in situ stations (from 1 to $m = 54$), y is the years in the series (from 1 to 15), μ_{gj} is the mean of all individual ET values for a given in situ station (g_{ij}), μ_{sj} is the mean of all individual ET values from the satellite at a given in situ station (s_{ij}), σ_{gj} is the standard deviation of all individual ET values of ET values for a given in situ station, σ_{sj} is the standard deviation of all individual ET values from the satellite at a given in situ station, g_{ij}^{1} is in situ measured time series with site means removed, s_{ij}^{1} is satellite observed time series with site means removed, g_{yj} is the annual mean of g_{ijy}^{1} which is the (annual) subset of g_{ij}^{1}, s_{yj} is the annual mean of s_{ijy}^{1} which is the (annual) subset of s_{ij}^{1}, g_{ij}^{2} is in situ measured time series with the site and annual means removed, s_{ij}^{2} is satellite observed time series with the site and annual means removed.

Moreover, it should be noted that in the calculation of inter-annual and intra-annual KGEs, the mean terms should theoretically approach zero (exactly zero if there were no missing data). In such cases, we set the mean ratio of the KGE equal to one due to the fact that there is no mean error contributing to the KGE particularly when both means are equal and identical (Knoben et al., 2019).

3.5. ET products intercomparison

For products intercomparison, ET values have been extracted from BESS, MODIS (MOD16A2) and PML satellite products by considering the weighted mean (based on area fraction) of all the pixels (of the given satellite) falling within the SEVIRI pixel at all 54 sites between 2004 and 2018. However, for GLEAM data, the ET values have been extracted directly from the pixels where the flux towers are located in 54 sites. Moreover, daily SEVIRI, GLEAM, and BESS ET data have been converted to 8-day sum to make them consistent with MOD16A2 and PML data. Taylor diagram (Taylor, 2001), was employed to perform ET products intercomparison and assess the 8-day SEVIRI-ET_a performance with respect to the other four ET products as well as the in situ ET measurements. Taylor diagrams have been drawn for various ecosystems and climate zones, taking the mean values of all the sites belonging to each ecosystem type and climate zone.

4. Results

4.1. SEVIRI satellite pixel homogeneity analysis

SEVIRI pixel homogeneity results are shown in Table A4 of the Appendix. The results showed that 19 of the forest sites, four of the crop sites, and one of the grass sites were identified as relatively homogeneous based on our pixel purity analysis. We identified no homogeneity in any peatland sites. Therefore, we assumed that 24 (44.4%) of the total sites were relatively homogeneous. Moreover, there were a few sites with a pixel purity higher than 80%, and thus initially classified as homogeneous, but they still have to be considered as heterogeneous sites. The reason is that the MODIS-derived dominant land cover types do not agree with the reported actual ecosystem type of such sites. This can partially be attributed to the classification error in the MODIS land cover product.

GSI results showed a variation range of 0 to 0.69, considering all individual sites. We observed that in homogeneous sites (based on our set criteria and pixel purity analysis), the GSI values were lower than 0.44.

4.2. Dimensions information extraction for EC sites

Information on the two spatial dimensions extracted from related sources is shown in Table A5 of the Appendix. Out of 54 (100%) sites, in the ecosystem dimension, there are 30 (55.5%) sites located in the forest ecosystem, 10 (18.5%) sites in the crop ecosystem, nine (16.6%) sites in the grass ecosystem and five (9.2%) sites in the peatland ecosystem. Regarding climate zone dimension, three (5.5%) sites in Alpine (polar tundra) [A-pt], six (11.11%) in Boreal (snow fully humid cool summer) [B-sfhcs], four (7.4%) in Boreal (snow fully humid warm summer) [B-sfhws], one (1.8%) in warm temperate fully humid hot summer [WT-fhhs], 35 (64.8%) in warm temperate fully humid warm summer [WT-fhws], five (9.2%) in warm temperate summer dry hot summer [WT-sdhs].

It should be noted that the widespread use of ET as the standard Köppen-Geiger classification code for Alpine (polar tundra) climate zone may potentially confuse readers, as it is also a known acronym for evapotranspiration. To mitigate this confusion, we have introduced new acronyms specific to different climate zones in our study. One can find both the standard Köppen-Geiger classification codes and their corresponding new acronyms, as used in this study, in Table A5 of the Appendix for reference.

4.3. Diurnal (Sub-daily) SEVIRI-ET accuracy

Time series of diurnal SEVIRI-ET_a observations from 2004 to 2018 were evaluated against available diurnal ET_a measurements at 54 EC sites, respectively. Table 4 shows the statistical error metrics computed between SEVIRI-ET_a and in situ ET at the diurnal time step.

At diurnal products of SEVIRI-ET_a, the KGE varied between −1.6 to 0.8 across different sites, with a median value of 0.26. Considering the RMSE, the variation range obtained from 0.04 to 0.14 mm $hour^{-1}$ with the median value of 0.07 mm $hour^{-1}$. Separating the diurnal SEVIRI-ET_a error statistics based on homogeneous (and heterogeneous) sites showed a KGE range of −0.38 (−1.6) to 0.78 (0.8) with the median value of 0.2 (0.29) and RMSE range of 0.04 mm $hour^{-1}$ (0.04 mm $hour^{-1}$) to 0.08 (0.14) with a median value of 0.07 (0.07). Considering the scatterplots and temporal patterns at the diurnal scale, a fair agreement was found between SEVIRI-ET_a and in situ ET_a at most sites. As representative examples at the diurnal level, the scatterplots between SEVIRI-ET_a and in situ ET_a are shown in Fig. 5 for a grassland (IT-Tor site in Fig. 5a), a forest (RU-Fyo in Fig. 5b), a peatland (CZ-wet in Fig. 5c) and a cropland (BE-Lon in Fig. 5d) site.

Diurnal temporal profiles of SEVIRI-ET_a and in situ ET_a are shown in Fig. 6 for a grassland (IT-Tor site in Fig. 6a), a forest (RU-Fyo in Fig. 6b), a peatland (CZ-wet in Fig. 6c) and a cropland (BE-Lon in Fig. 6d) site. While for most of the shown sites and years agreement was fair, SEVIRI overestimated in situ measurements, especially for the site CZ-wet.

The accuracy change in diurnal SEVIRI-ET_a demonstrated a kind of diurnal cycle behavior during the day (Fig. 7). However, the observed diurnal cycle in the accuracy was not identical across the months of the year and ecosystems. Considering the months of June in the whole time-series, for instance, at IT-Tor grassland (Fig. 7b) and RU-Fyo forest site (Fig. 7d), we observed the highest accuracy (IT-Tor: median KGE ≈ 0.45 and RU-Fyo: KGE ≈ 0.30) in the mid-day time (IT-Tor: around 07:00 to 18:00, and RU-Fyo: around 10:00 to 16:00). Although more fluctuations were observed in the diurnal cycle accuracy at CZ-wet peatland (Fig. 7f) and BE-Lon crop site (Fig. 7h) in the mid-day, the highest accuracy was found later in the afternoon time. In CZ-wet site, the accuracy started increasing (from median KGE ≈ −1.6) at 05:00 and reached the maximum accuracy (up to median KGE ≈ 0.3) around 18:00 in June. In BE-Lon site, almost a similar pattern was observed as in CZ-wet, but the increase in the accuracy was smoother, it started increasing (from median KGE ≈ −1.4) at 06:00, and later in the evening, it reached the maximum accuracy (upto median KGE ≈ 0.5) around 18:00. However, relatively lower (unstable) accuracy (mostly median KGE < 0) were

Table 4
Comparison between diurnal SEVIRI-ET_a observations and in situ diurnal SEVIRI-ET_a measurements over 54 sites.

Site	KGE [−]	RMSE [mm hour^{-1}]
BE-Bra	0.61	0.04
BE-Lon	−0.06	0.07
BE-Vie	0.29	0.05
CH-Aws	0.53	0.05
CH-Cha	0.8	0.05
CH-Dav	0.52	0.08
CH-Fru	0.6	0.06
CH-Lae	0.76	0.08
CH-Oe2	0.39	0.08
CZ-BK1	−0.32	0.08
CZ-Lnz	0.38	0.06
CZ-RAJ	−0.79	0.09
CZ-Stn	−0.14	0.08
CZ-wet	−1.06	0.14
DE-BER	−0.11	0.05
DE-EC2	0.39	0.07
DE-EC4	0.2	0.07
DE-Fen	0.15	0.09
DE-Geb	−0.14	0.08
DE-Gri	0.2	0.06
DE-Hai	0.11	0.07
DE-HoH	0.51	0.06
DE-Kli	0.02	0.08
DE-Obe	0.34	0.07
DE-RbW	–	–
DE-RuR	0.53	0.05
DE-RuS	0.62	0.06
DE-RuW	0.56	0.07
DE-SfS	0.32	0.08
DE-Tha	−0.04	0.09
DE-ZRK	0.44	0.07
DK-Sor	0.26	0.07
ES-Abr	−0.29	0.07
ES-LM1	0	0.08
ES-LM2	−0.26	0.08
FI-Hyy	0.05	0.06
FI-Let	0.02	0.06
FI-Sii	0.63	0.04
FI-Var	−1.6	0.07
FR-Bil	0.78	0.07
FR-EM2	0.01	0.08
FR-Hes	0.34	0.07
IT-BCi	0.7	0.07
IT-Lsn	−0.24	0.09
IT-SR2	0.13	0.07
IT-Tor	0.78	0.05
NL-Loo	0.55	0.06
RU-Fy2	0.2	0.07
RU-Fyo	0.41	0.07
SE-Deg	0.05	0.05
SE-Htm	0.32	0.04
SE-Nor	0.36	0.04
SE-Ros	0.11	0.05
SE-Svb	−0.38	0.06

observed for all four sites in the month of January (left panels of Fig. 7) from 2004 to 2018.

4.4. Daily SEVIRI-ET accuracy

Time series of SEVIRI-ET_a and SEVIRI-ET_0 observations from 2004 to 2018 were evaluated against available daily ET_a and ET_0 measurements at 54 EC sites, respectively. Table 5 shows the statistical error metrics computed between daily SEVIRI-ET (both ET_a and ET_0) and in situ ET (both ET_a and ET_0).

Considering SEVIRI-ET_a, the KGE varied between −0.88 to 0.93 across different sites, with a median value of 0.60. Regarding the RMSE, the variation range was from 0.43 to 1.79 mm day^{-1} with the median value of 0.77 mm day^{-1}. SEVIRI-ET_0 comparison results revealed a range of KGE values from 0.51 to 0.94 with a median value of 0.77 and RMSE ranging between 0.40 mm day^{-1} to 1.50 mm day^{-1} with a median value of 0.57 mm day^{-1}. Separating the SEVIRI-ET_a error statistics based on homogeneous (and heterogeneous) sites showed the KGE range of −0.88 (−0.31) to 0.88 (0.93) with the median value of 0.54 (0.61) and RMSE range of 0.51 (0.43) to 1.25 (1.79) with the median value of 0.76 (0.78). In the case of SEVIRI-ET_0, the results showed the KGE range of 0.51 (0.58) to 0.90 (0.94) with a median value of 0.77 (0.76) and RMSE range of 0.44 (0.4) to 1.51 (1.44) with the median value of 0.56 (0.60).

Considering the SEVIRI-ET_0 error statistics based on homogeneous (and heterogeneous) sites demonstrated the KGE range of 0.51 (0.56) to 0.84 (0.94) with the median value of 0.76 (0.77) and RMSE range of 0.44 (0.40) to 1.09 (1.5) with the median value of 0.57 (0.58). All individual sites in Table 5 with KGE > 0.3 were considered for exploring the accuracy in further spatial and temporal dimensions. At those sites with lower KGE, we mainly observed higher variability error and higher bias. In total, 47 and 54 sites have been utilized to perform dimensional accuracy assessment for SEVIRI-ET_a and SEVIRI-ET_0, respectively.

Furthermore, the long-term comparison of results demonstrated a close agreement in the scatterplots and temporal patterns between SEVIRI-ET and in situ ET at most sites for both ET_a and ET_0. As representative examples, the scatterplots between SEVIRI-ET and in situ ET are shown in Fig. 8 for a grassland (IT-Tor site in Fig. 8a & b), a forest (RU-Fyo in Fig. 8c & d), a peatland (CZ-wet in Fig. 8e & f) and a cropland (BE-Lon in Fig. 8g & h) site.

Corresponding temporal profiles between SEVIRI-ET and in situ ET are shown in Fig. 9 for a grassland (IT-Tor site in Fig. 9a & b), a forest (RU-Fyo in Fig. 9c & d), a peatland (CZ-wet in Fig. 9e & f) and a cropland (BE-Lon in Fig. 9g & h) site.

4.4.1. Intra-annual dimension

Intra-annual dimension analysis showed variations in the accuracy of the SEVIRI-ET_a (Fig. 10: left panels) and SEVIRI-ET_0 (Fig. 10: right panels) along the year. The results demonstrated that the accuracy was low in the first quarter of the year (from January to March), increased in the mid-year (from April to October), and then began to decline in the last quarter (from November to December). However, accuracy remained relatively stable during the mid-year (SEVIRI-ET_a: 0.3 < median KGE < 0.5 and SEVIRI-ET_0: 0.1 < median KGE < 0.65), it varied considerably in the first quarter (SEVIRI-ET_a: −2.3 < median KGE < 0 and SEVIRI-ET_0: −3 < median KGE < 0) and the last quarter (SEVIRI-ET_a: −3 < median KGE < -0.4 and SEVIRI-ET_0: −3.2 < median KGE < -0.7) (Fig. 10a & b). Comparatively short boxplots in mid-year (Fig. 10a & b) confirmed the high levels of agreement between the SEVIRI-ET and in situ ET during this period, while broader distributions of the accuracy were obtained in the first and the last quarter. Almost similar trends in the accuracy of SEVIRI-ET (both ET_a and ET_0) were detected when we considered heterogeneous (Fig. 10c & d) and homogeneous (Fig. 10e & f) pixels separately, albeit with some fluctuations, especially in negative KGE distributions.

4.4.2. Inter-annual dimension

Inter-annual variability of the SEVIRI-ET accuracy is shown in Fig. 11 (SEVIRI-ET_a: left panels and SEVIRI-ET_0: right panels). The results revealed that, for the whole time series from 2004 to 2018, the degree of agreement between SEVIRI-ET and in situ ET was low in the first quarter of the year, increased in the mid-year, and then declined again at the last quarter (Fig. 11a & b). However, this trend varied between SEVIRI-ET_a and SEVIRI-ET_0 considerably. In the SEVIRI-ET_a case, the mid-year positive KGE varied more from one year to another, and one could see a variation between median KGE values and distributions (Fig. 11a). A similar trend was observed in the heterogeneous (Fig. 11c) and homogeneous (Fig. 11e) sub-groups, specifically for positive median KGEs variations during the mid-year. However, in the SEVIRI-ET_0 case, unlike the SEVIRI-ET_a, the mid-year positive KGE values were relatively stable and did not change significantly from one year to another except in the years 2016 and 2017 (Fig. 11b). This demonstrated a slight change in

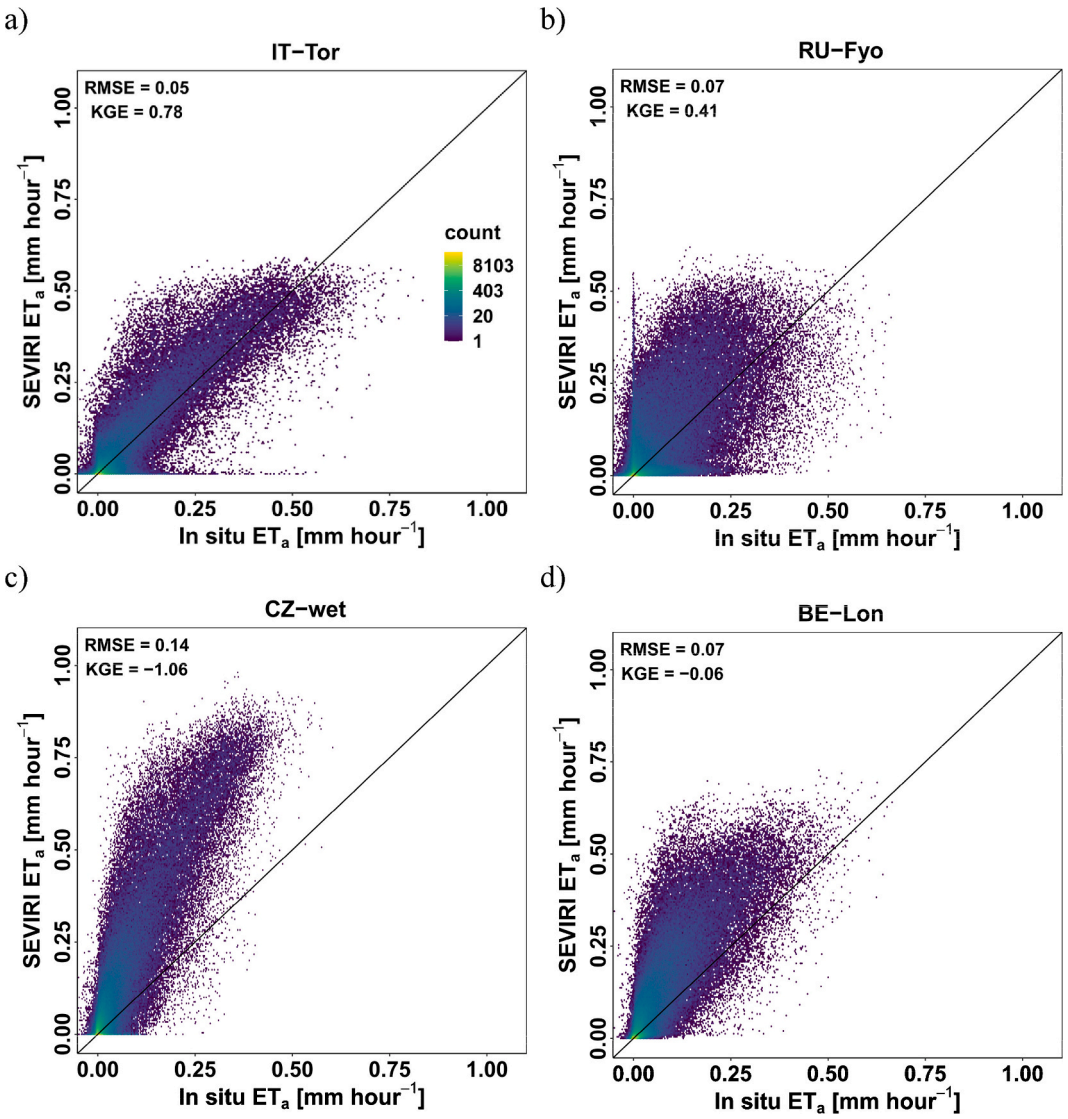

Fig. 5. Density scatterplot comparisons of sub-daily SEVIRI-ET$_a$ and in situ ET$_a$ values over a grassland (IT-Tor site [a]), a forest (RU-Fyo [b]), a peatland (CZ-wet [c]) and a cropland (BE-Lon [d]) site. The color representation is based on logarithmically transformed data, using a hexagonal binning approach with 220 bins and a logarithmic color scale, highlighting density patterns within the data distribution. Note: the shared legend in Fig. 5a applies to all subplots (Fig. 5a-d), as the color scale remains consistent across all subplots. The RMSE, and KGE are shown on the scatterplots.

SEVIRI-ET$_0$ accuracy during the whole period (2004–2018). Such a trend was consistent and repeated in heterogeneous (Fig. 11d) and homogeneous (Fig. 11f) sub-groups, specifically for positive median KGEs variations during the mid-year.

4.4.3. Ecosystem dimension

SEVIRI-ET accuracy results based on ecosystem dimension are shown in Fig. 12 (SEVIRI-ET$_a$: left panels and SEVIRI-ET$_0$: right panels). Considering the median statistics based on the ecosystem type (i.e., the grouping of EC sites based on the type of ecosystem) revealed that the highest agreement between SEVIRI-ET$_a$ and in situ ET$_a$ was found for peat and grassland ecosystems (median KGE $\approx$ 0.72) (Fig. 12a). The second best agreement was observed in forest ecosystems (median KGE $\approx$ 0.68), while the lowest agreement was observed for cropland ecosystems (median KGE $\approx$ 0.52). Although such an order in SEVIRI-ET$_a$ accuracy remained almost similar in homogeneous and heterogeneous sites except for croplands and grasslands (Fig. 12a), a wider distribution was observed for the KGE values in heterogeneous sub-groups.

In SEVIRI-ET$_0$, the highest agreement was observed in crop and grassland ecosystems (0.81 > median KGE > 0.78 (Fig. 12b). The lowest agreement was observed in forest ecosystems (median KGE $\approx$ 0.73). In peatland ecosystems, the median KGE was 0.76 (Fig. 12b). In general, agreement in ET$_0$ was better and differed less between ecosystem types than agreement in ET$_a$ (Fig. 12a). When separating the sites into heterogeneous and homogeneous, the trend of accuracies remained the same; however, certain changes were observed between the absolute values of median KGEs, especially in forest and grass ecosystems (Fig. 12a).

Moreover, variations were observed between the median of RMSE for SEVIRI-ET estimates. For SEVIRI-ET$_a$ (SEVIRI-ET$_0$) an RMSE of about 0.72 (0.45), 0.74 (0.63), 0.65 (0.60), 0.90 (0.54) mm day^{-1} was obtained for peatland, forest, grassland and cropland ecosystems, respectively (Fig. 12c & d). Similar orders of accuracy and trends were detected in heterogeneous and homogeneous sub-groups.

4.4.4. Climate dimension

Different levels of agreement were observed between SEVIRI-ET products and in situ ET in the climate zone (Fig. 13) dimension (SEVIRI-ET$_a$: left panels and SEVIRI-ET$_0$: right panels). For SEVIRI-ET$_a$, a range 0.37 < median KGE < 0.80 was observed in all climate zones

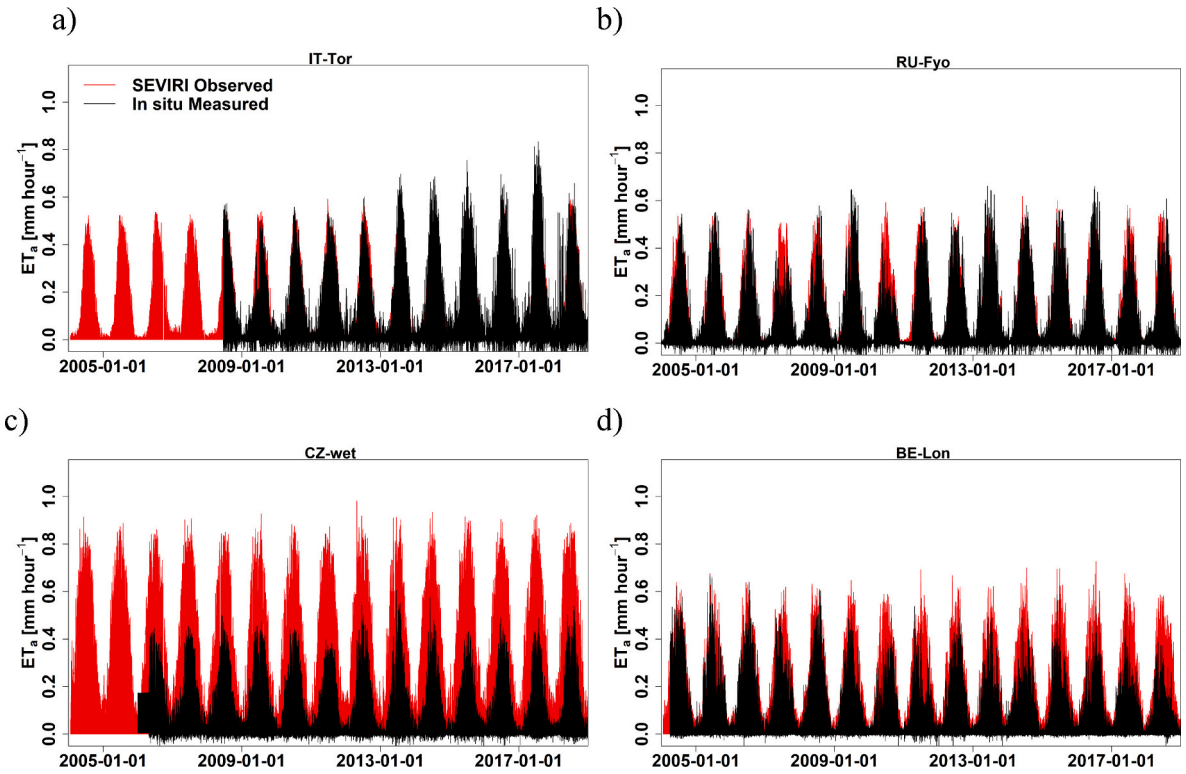

Fig. 6. Temporal profile comparisons of sub-daily SEVIRI-ET$_a$ and in situ ET$_a$ values over a grassland (IT-Tor site [a]), a forest (RU-Fyo [b]), a peatland (CZ-wet [c]), and a cropland (BE-Lon [d]) site.

(Fig. 13a). The highest agreement (KGE ≈ 0.80) was obtained for Boreal Snow fully humid warm summer (B-sfhws) climate zone. However, Warm Temperate fully humid hot summer (WT-fhhs) and Warm Temperate summer dry hot summer (WT-sdhs) were identified as the zones with the lowest median KGE ≈ 0.36–0.39.

The KGE results separated for homogeneous/heterogeneous sites revealed relatively lower agreement in homogeneous Alpine polar tundra (A-pt) with the median KGE ≈ 0.35, and homogeneous Boreal Snow fully humid cool summer (B-sfhcs) with the median KGE ≈ 0.45 (Fig. 13a). For SEVIRI-ET$_0$, the median KGE varied between 0.71 and 0.85 among all climate zones except for WT-sdhs in which the median KGE ≈ 0.58 was obtained (Fig. 13b). Moreover, WT-fhhs was identified as a climate zone with the highest agreement (KGE ≈ 0.85). The separated median KGEs in heterogeneous and homogeneous sites followed similar trends as observed in combined (all) sites KGEs in various climate zones (Fig. 13b). Moreover, the separated KGE values revealed comparable results in homogeneous/heterogeneous sites in most of the sites except some differences observed in A-pt and Boreal Snow fully humid cool summer (B-sfhcs) in which the homogeneous sites showed lower median KGE than heterogeneous ones (Fig. 13b).

Regarding RMSE variations among climate zones, for SEVIRI-ET$_a$, the range 0.6 < median RMSE<1 mm day^{-1} was obtained in all climate zones considering all sites (Fig. 13c). Separating the RMSE values between homogeneous and heterogeneous sites resulted in comparable accuracy among these two sub-groups. The median RMSE<1 mm day^{-1} was obtained in separated homogeneous and heterogeneous sites in all climate zones except for the homogeneous A-pt zone (the median RMSE ≈ 1.25 mm day^{-1}) (Fig. 13c). For SEVIRI-ET$_0$, the range 0.5 < median RMSE < 0.62 mm day^{-1} was obtained in the majority of climate zones for all and heterogeneous sites except in WT-sdhs zone where the highest median RMSE of 1.41 mm day^{-1} was observed (Fig. 13d).

4.5. Decomposition of diurnal and daily SEVIRI-ET accuracies

The decomposition of total accuracy resulted in spatial, temporal, inter-annual, and intra-annual accuracy components for diurnal SEVIRI-ET$_a$ (Fig. 14) and daily SEVIRI-ET (Fig. 15: SEVIRI-ET$_a$: left panels and SEVIRI-ET$_0$: right panels). The accuracy decomposition results at sub-daily (diurnal) level showed that the values of RMSE at single dimensions (i.e., spatial, temporal, inter-annual, and intra-annual) were either lower ("better") than the total RMSE or remained almost the same ("no significant change") (Fig. 14a). Note that due to the nonlinear nature of RMSEs, however, the component values are not strictly additive. This pattern was also preserved in heterogeneous (Fig. 14b) and homogeneous (Fig. 14c) groups. For KGE, the one-dimension values either were higher ("better") than total KGE (i.e., temporal and intra-annual dimensions) or lower ("worse") (i.e., spatial and inter-annual dimensions) than the total one not only in all diurnal SEVIRI-ET$_a$ (Fig. 14a) groups but also in heterogeneous (Fig. 14b) and homogeneous (Fig. 14c) ones.

At the daily level, the results revealed that the single dimension RMSE was always smaller ("better") than the total RMSE in both SEVIRI-ET$_a$ (Fig. 15a) and SEVIRI-ET$_0$ (Fig. 15b). Such a pattern was identically observed in both heterogeneous (Fig. 15c & d) and homogeneous (Fig. 15e & f) groups. For KGE, the one-dimension values either remained almost the same ("no significant change") as total KGE (i.e., temporal and intra-annual dimensions) or were lower ("worse") (i.e., spatial and inter-annual dimensions) than the total one not only in all SEVIRI-ET$_a$ (Fig. 15a) and SEVIRI-ET$_0$ (Fig. 15b) groups but also in heterogeneous (Fig. 15c & d) and homogeneous (Fig. 15e & f) ones.

4.6. ET products intercomparison

The error statistics of the satellite ET products for SEVIRI, MODIS (MOD16A2), PML, BESS, GLEAM are shown in Taylor diagrams in Fig. 16 for selected ecosystem types (left panels) and climate zones (right

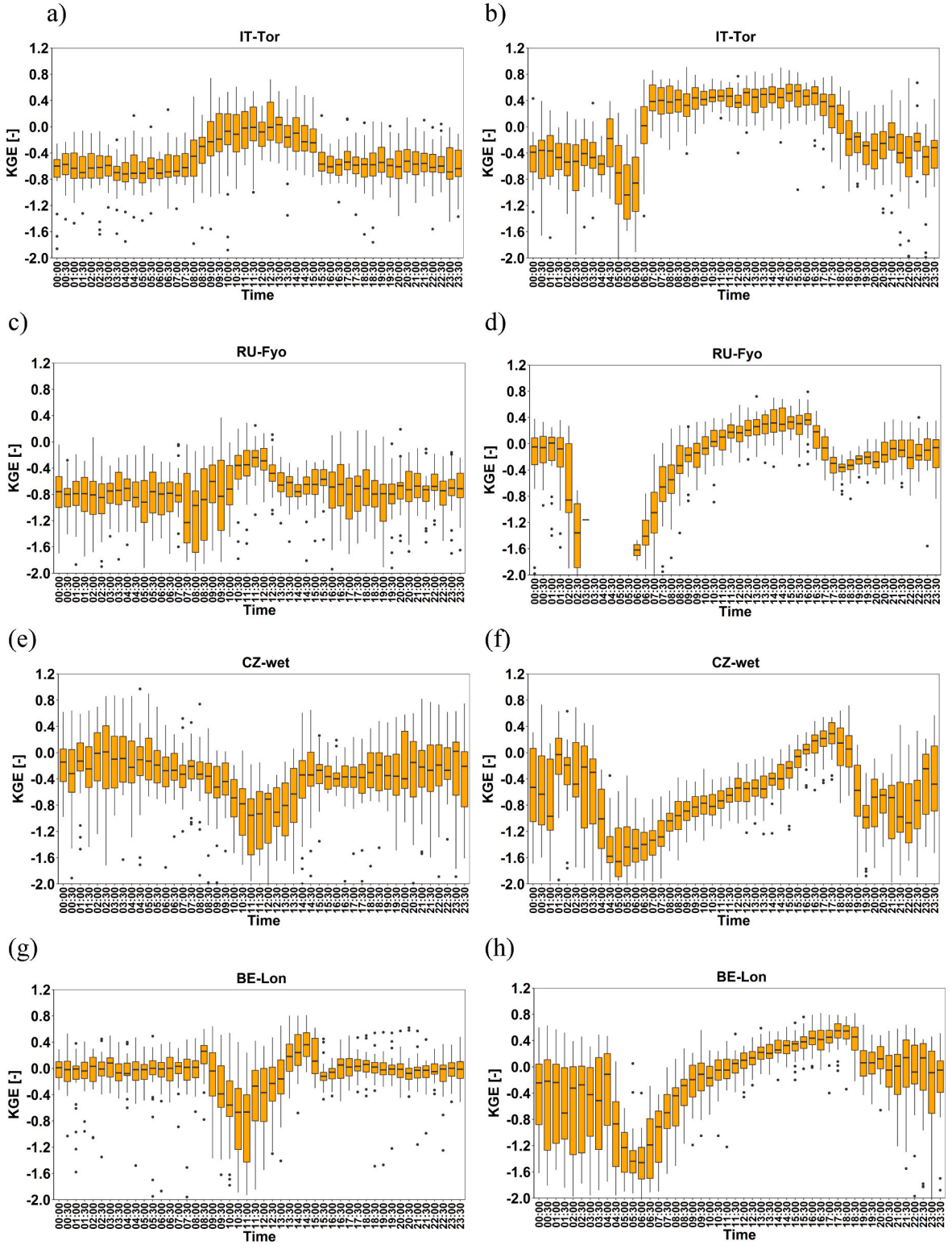

Fig. 7. Sub-daily variation (diurnal cycle) of KGE for January (displayed on the left panels) and June (displayed on the right panels) across the whole time-series (2004–2018), over a grassland (IT-Tor site [a & b]), a forest (RU-Fyo [c & d]), a peatland (CZ-wet [e & f]) and a cropland (BE-Lon [g & h]) site.

panels).

The results of ecosystem types showed that, in crop (Fig. 16a), SEVIRI (PML) ET_a estimates had the highest (lowest) correlation coefficient (R) of 0.91 (0.88) with the in situ ET compared to the other ET products. In terms of the centered root mean square difference (RMSD) and standard deviation (σ), MODIS performed the best (RMSD = 2.76 and σ = 5.79 mm 8-day^{-1}), and the SEVIRI performance decreased considerably (RMSD = 5.11 and σ = 9.86 mm 8-day^{-1}) among all the products. In the Forest ecosystem (Fig. 16c), similar to crop, SEVIRI (PML) ET_a estimates showed the highest (lowest) R of 0.82 (0.79) among the products. SEVIRI ET estimates had the highest RMSD of 5.43 mm 8-day^{-1} and σ of 8.63 mm 8-day^{-1}, while the lowest RMSD (4.53 mm 8-

Table 5
Comparison between daily SEVIRI-ET (both ET_a and ET_0) observations and in situ ET (both ET_a and ET_0) measurements over 54 sites.

Site	KGE [−]		RMSE [mm day^{-1}]	
	SEVIRI-ET_a	SEVIRI-ET_0	SEVIRI-ET_a	SEVIRI-ET_0
BE-Bra	0.42	0.75	0.71	0.62
BE-Lon	0.5	0.84	0.83	0.49
BE-Vie	0.71	0.78	0.54	0.56
CH-Aws	0.36	0.7	1.25	0.64
CH-Cha	0.83	0.82	0.64	0.43
CH-Dav	0.53	0.8	0.97	0.54
CH-Fru	0.93	0.78	0.57	0.6
CH-Lae	0.73	0.77	1.03	0.61
CH-Oe2	0.75	0.8	0.99	0.48
CZ-BK1	0.23	0.77	0.99	0.56
CZ-Lnz	0.76	0.74	0.77	0.7
CZ-RAJ	−0.15	0.72	1.24	0.64
CZ-Stn	0.41	0.75	0.88	0.64
CZ-wet	−0.31	0.84	1.79	0.4
DE-BER	0.38	0.65	0.65	0.91
DE-EC2	0.72	0.8	0.84	0.54
DE-EC4	0.61	0.82	0.86	0.48
DE-Fen	0.46	0.77	1.33	0.87
DE-Geb	0.37	0.77	0.92	0.65
DE-Gri	0.61	0.78	0.65	0.56
DE-Hai	0.56	0.75	0.75	0.63
DE-HoH	0.88	0.68	0.64	0.8
DE-Kli	0.5	0.74	0.97	0.68
DE-Obe	0.71	0.71	0.81	0.69
DE-RbW	0.21	0.75	0.93	0.63
DE-RuR	0.86	0.82	0.45	0.45
DE-RuS	0.8	0.82	0.77	0.47
DE-RuW	0.72	0.79	0.86	0.5
DE-SfS	0.63	0.75	0.82	0.61
DE-Tha	0.26	0.66	1.06	0.85
DE-ZRK	0.81	0.86	0.75	0.44
DK-Sor	0.67	0.83	0.7	0.49
ES-Abr	0.35	0.59	0.75	1.41
ES-LM1	0.57	0.58	0.79	1.44
ES-LM2	0.39	0.56	0.9	1.5
FI-Hyy	0.41	0.7	0.73	0.62
FI-Let	0.84	0.77	0.57	0.48
FI-Sii	0.93	0.76	0.43	0.46
FI-Var	−0.88	0.51	1.09	1.09
FR-Bil	0.88	0.8	0.6	0.65
FR-EM2	0.52	0.8	0.8	0.52
FR-Hes	0.77	0.71	0.71	0.74
IT-BCi	0.36	0.84	1.25	0.77
IT-SR2	0.59	0.94	0.74	0.48
IT-Tor	0.88	0.9	0.55	0.56
NL-Loo	0.7	0.81	0.73	0.47
RU-Fy2	0.64	0.73	0.63	0.58
RU-Fyo	0.8	0.77	0.64	0.49
SE-Deg	0.51	0.74	0.69	0.52
SE-Htm	0.64	0.8	0.51	0.44
SE-Nor	0.68	0.71	0.52	0.61
SE-Ros	0.5	0.72	0.6	0.5
SE-Svb	0.24	0.71	0.83	0.57

day^{-1}) and σ (7.36 mm 8-day^{-1}) were obtained in GLEAM and PML ET products. The grass ecosystem results (Fig. 16e) showed that SEVIRI ET_a and BESS ET estimates had the highest (0.81) and lowest (0.77) R among the products. The PML was the best (RMSD = 4.85 and σ =7.71 mm 8-day^{-1}), and MODIS was the worst (RMSD = 5.72 and σ = 9.30 mm 8-day^{-1}) product in estimating ET in grass ecosystem.

Furthermore, the climate zone results demonstrated that, in WT-sdhs (Fig. 16b), in general, a lower range of variations was obtained for R with the minimum value of 0.38 mm 8-day^{-1} for MODIS and the maximum value of 0.51 for SEVIRI ET_a estimates. Poor performance (RMSD = 8.62 and σ =9.77 mm 8-day^{-1}) was obtained for BESS ET estimates, while MODIS performed well (RMSD = 4.98 and σ =3.80 mm 8-day^{-1}) among others. In WT-fhws climate zone (Fig. 16d), SEVIRI ET_a estimates showed the highest R (0.87), RMSD (5.48 mm 8-day^{-1}), and σ (9.60 mm 8-day^{-1}). In this climate zone, the lowest R (0.84) was obtained for PML, while the lowest RMSD (4.21 mm 8-day^{-1}) and σ (7.87 mm 8-day^{-1}) were observed for the GLEAM ET product. In B-sfhcs climate zone (Fig. 16f), all the error statistics were highest (R = 0.86, RMSD = 6.33 mm 8-day^{-1} and σ =9.64 mm 8-day^{-1}) in SEVIRI ET_a estimates and lowest (R = 0.79, RMSD = 3.98 mm 8-day^{-1} and σ =6.41 mm 8-day^{-1}) in BESS ET product.

Based on the Taylor diagram results, the SEVIRI satellite was able to achieve the highest (the best) R across all ecosystem types and climate zones and outperformed the other ET products (Fig. 16). However, the lower (better) RMSD and σ values, and therefore, ET estimates closer to the in situ measurements, were observed for PML (in forest and grass ecosystems), MODIS (in crop ecosystem and WT-sdhs climate zone), GLEAM (in forest ecosystem and WT-fhws climate zone) and BESS (in B-sfhcs climate zone) products. In WT-sdhs climate zone, all the ET products had very low correlations, and the majority of them (except MODIS) showed much larger variations than observed, resulting in a relatively large RMSD in the ET estimates indicating the failure of satellite ET products to reproduce the in situ ET in this specific climate zone.

5. Discussion

5.1. Overall diurnal and daily SEVIRI-ET accuracy

The evaluation resulted overall in a reasonably satisfactory agreement between SEVIRI-ET and in situ ET at the individual site level for both diurnal (Table 4) and daily SEVIRI-ET (Table 5). Direct accuracy assessment (i.e., the comparison of satellite observations with in situ measurements) of diurnal SEVIRI-ET_a revealed a KGE value of 0.26 across all 54 sites under investigation. Exploring the KGE components of this study yielded median values of 0.84, 1.51, and 1.5 for correlation, variability, and bias, respectively, for diurnal SEVIRI-ET. In our study, we found a higher correlation (0.84) for diurnal ET compared to the reported correlation (0.73) for diurnal ET by EUMETSAT LSA SAF (Ghilain et al., 2018). Similarly, for the RMSE at the diurnal level, our results showed slightly higher accuracy (median RMSE ≈ 0.07 mm hour^{-1}) compared to the RMSE of 0.08 mm hour^{-1} reported by EUMETSAT LSA SAF for diurnal ET.

Our findings here are in line with previous studies where a range of correlations (R^2: 0.56–0.9) was reported between SEVIRI-ET and in situ ET at hourly time step in Europe (Gellens-Meulenberghs et al., 2012; Ghilain et al., 2011). Moreover, our results demonstrated that one could expect the highest accuracy of diurnal SEVIRI-ET_a during the day, for instance, from 07:00 to 18:00 for the case of grassland and from 10:00 to 16:00 for the case of forest. This might be attributed to the fact that measuring night-time ET can be challenging due to various uncertainties and errors that can occur (Aubinet et al., 2012; Bambach et al., 2022). In particular, the eddy covariance method may not be entirely accurate when turbulence is poorly developed at night, leading to non-turbulent fluxes becoming as significant as turbulent fluxes. Additionally, condensation and dew can form on surfaces, including sensors and vegetation, during night-time, which may affect measurement accuracy, especially for sensors that rely on dry surfaces. In addition, the summer time diurnal SEVIRI-ET_a showed higher accuracy. This might partly be attributed to the complexity of taking reliable measurements during the night and winter time.

For daily SEVIRI-ET_a, validation was initially conducted by EUMETSAT LSA SAF as part of their product development. A mean R^2 of 0.78 and RMSE of 0.73 mm day^{-1} were reported as average statistics in their validation exercise for ET_a across Europe and Africa from March 2007 to December 2011 (Ghilain et al., 2018). It is further concluded in the EUMETSAT validation report that their results fulfilled the defined target accuracy variations range between 55% and 80% for SEVIRI-ET_a. The median statistics found in the current study (median R^2 ≈ 0.77 and RMSE ≈ 0.77 mm day^{-1}) are in line and close to the EUMETSAT validation results of SEVIRI-ET_a. Overall, comparable results were observed

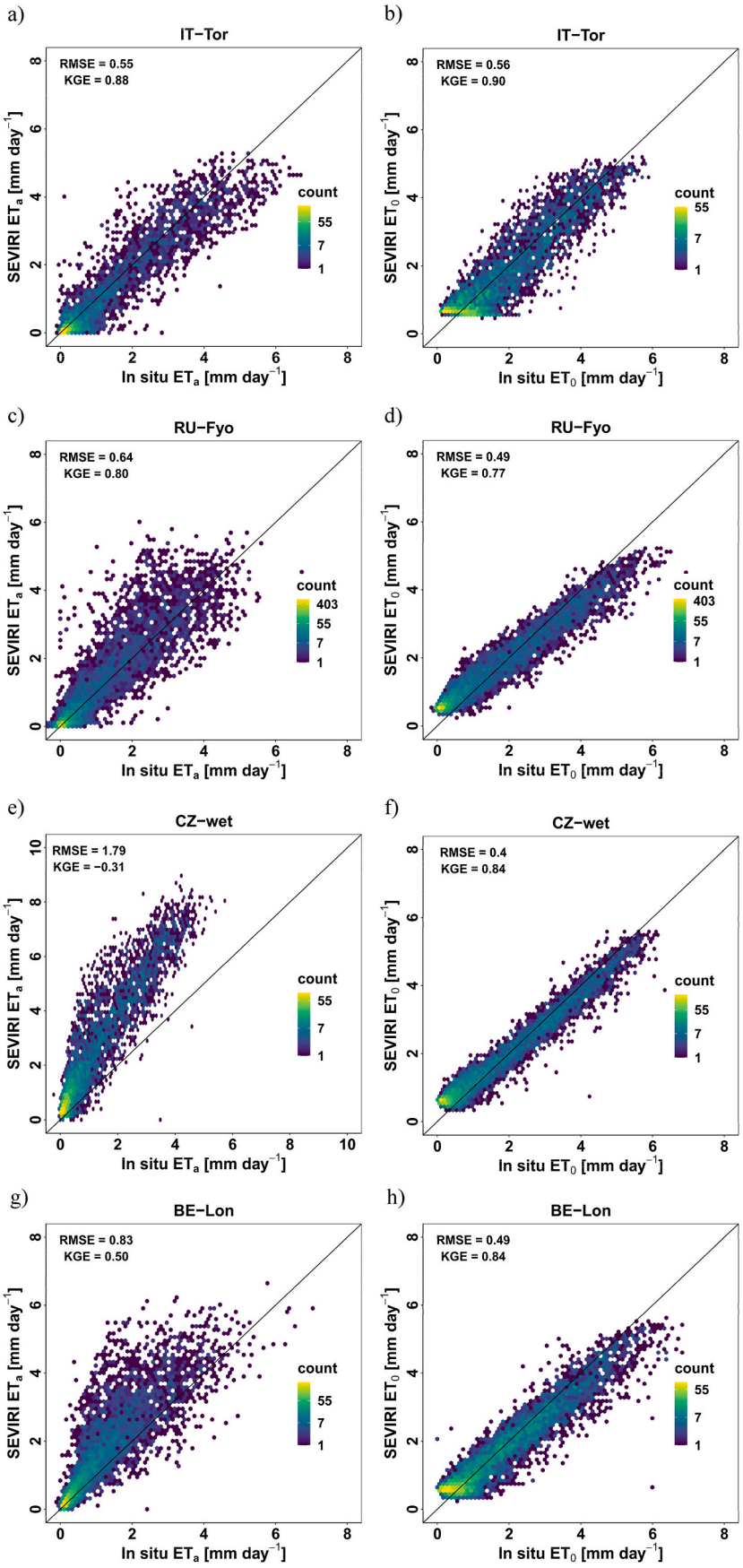

(caption on next page)

Fig. 8. Density scatterplot comparisons of SEVIRI and in situ ET values (ET_a displayed on the left panels and ET_0 on the right panels) over a grassland (IT-Tor site [a & b]), a forest (RU-Fyo [c & d]), a peatland (CZ-wet [e & f]) and a cropland (BE-Lon [g & h]) site. The color representation is based on logarithmically transformed data, using a hexagonal binning approach with 65 bins and a logarithmic color scale, highlighting density patterns within the data distribution. The RMSE, and KGE are shown on the scatterplots.

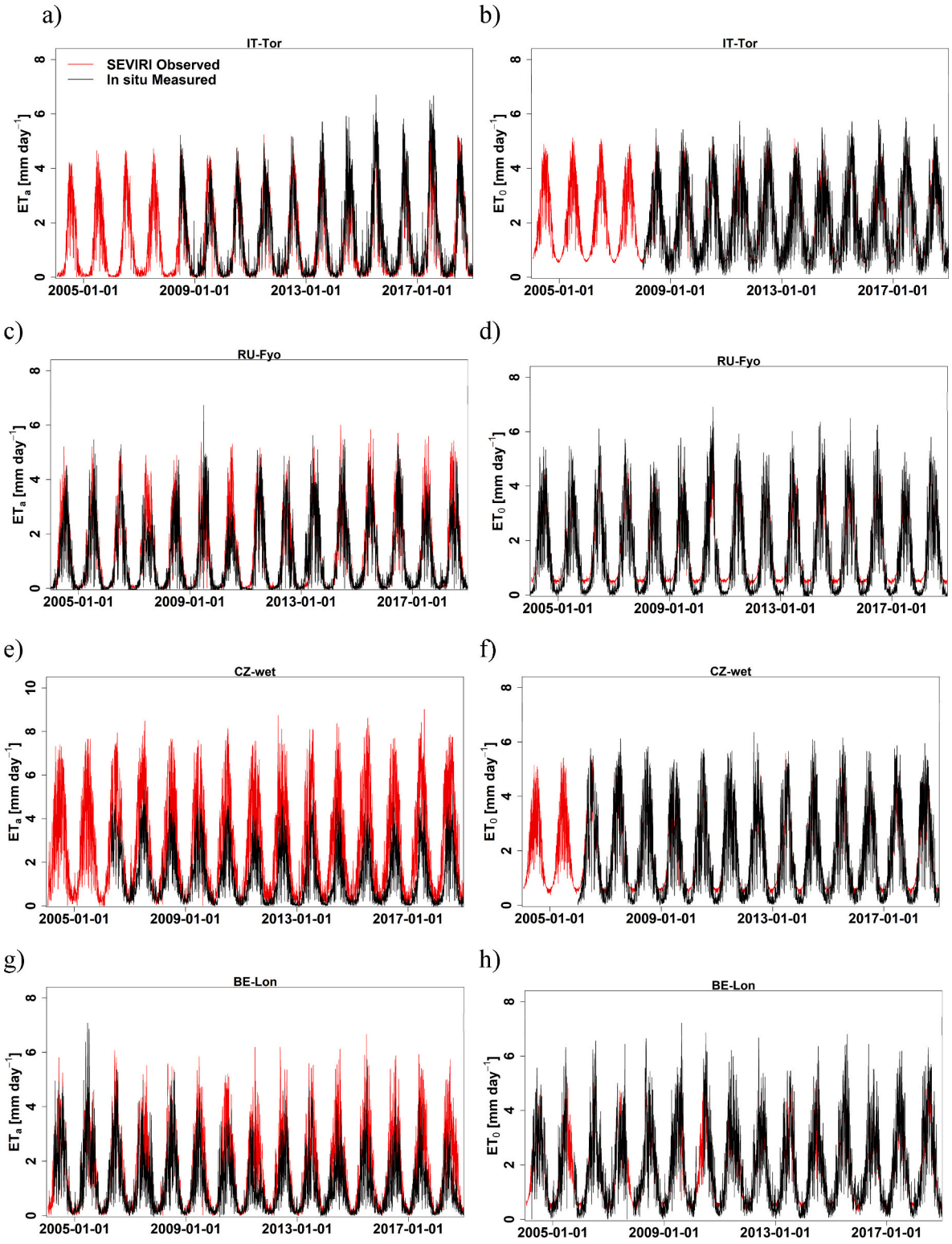

Fig. 9. Temporal profile comparisons of SEVIRI-ET and in situ ET values (ET_a displayed on the left panels and ET_0 on the right panels) over a grassland (IT-Tor site [a & b]), a forest (RU-Fyo [c & d]), a peatland (CZ-wet [e & f]) and a cropland (BE-Lon [g & h]) site.

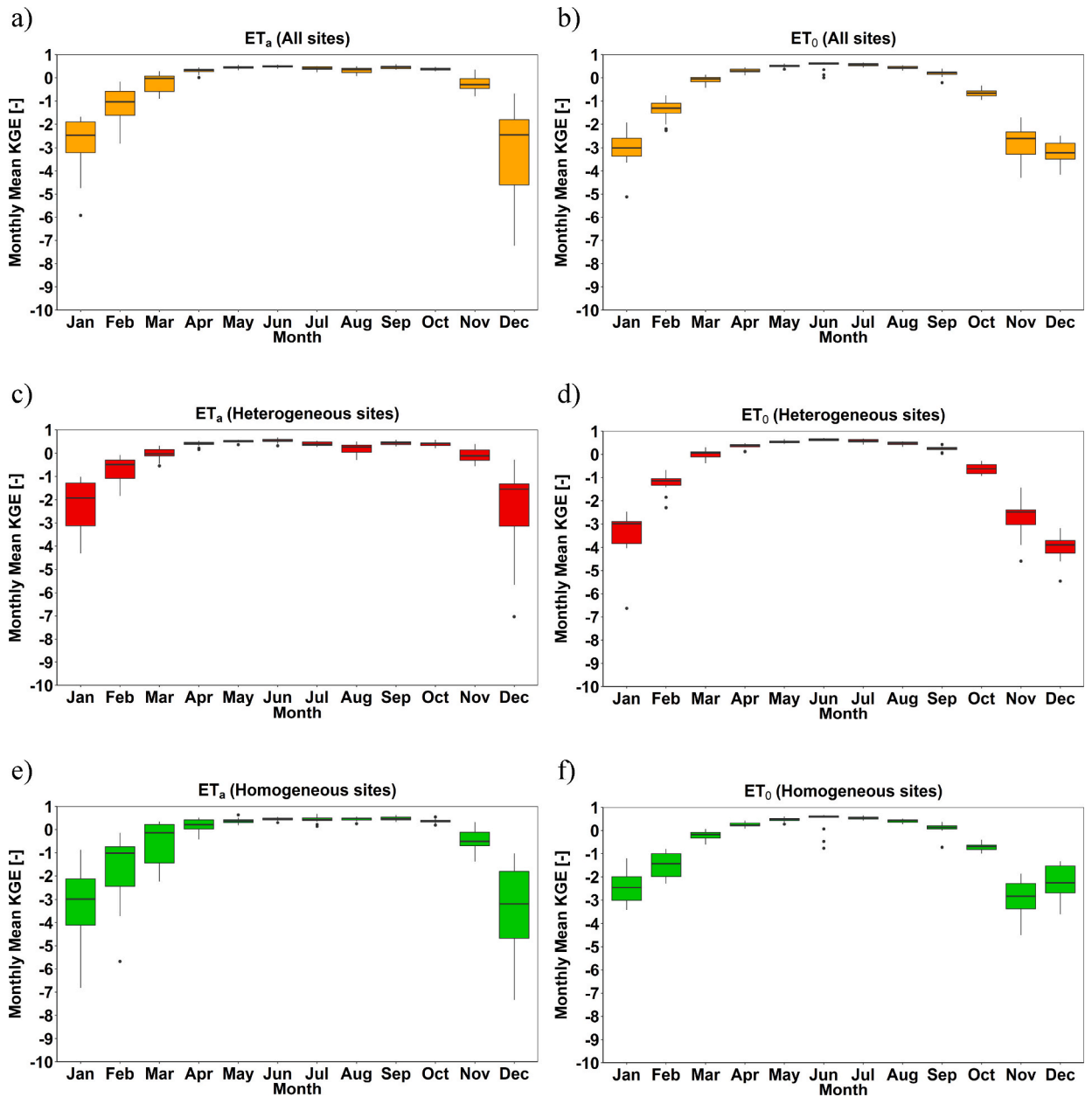

Fig. 10. SEVIRI-ET accuracies in the intra-annual dimension considering all and separated (i.e., heterogeneous and homogeneous) sites; KGE boxplots for SEVIRI-ET_a (left panels) and SEVIRI-ET_0 (right panels).

between the current study and the EUMETSAT initial validation report. Nevertheless, the current study can be considered a supplementary validation practice that can add more value by providing further insight into the quality of the recently published (version 3) data (2004–2018), taking into account more in situ sites (54 sites), albeit all distributed across Europe.

The SEVIRI-ET_0 followed well the in situ ET_0 in almost all sites (the median $R^2 \approx 0.92$ and RMSE ≈ 0.57 mm day^{-1}) (Table 5), and the agreement was better compared to daily SEVIRI-ET_a. This could be explained by the fact that the modeling of ET_0 is more straightforward than ET_a since ET_0 depends only on meteorological factors and, therefore, crop and soil characteristics hardly affect ET_0. However, SEVIRI-ET_0 underestimated in situ ET_0, which might be attributed to the measurement conditions of EC sites. Based on previous studies, if the Penman-Monteith approach uses input data measured on a relatively different surface, for instance, a drier one than what is prescribed as well-watered grass, then the calculated in situ ET_0 are over-estimated (Droogers and Allen, 2002; Temesgen et al., 1999; Trigo et al., 2018). Therefore, we hypothesize that SEVIRI-ET_0 are not under-estimated, but in situ ET_0 estimations are perhaps over-estimated. In contrast to the Penman-Monteith method, SEVIRI-ET_0 products are not influenced by local aridity or advective effects (Trigo and DeBruin, 2016). Our findings are further supported by previous validation exercises where good agreement was explored between daily SEVIRI-ET_0 and in situ ET_0 in various sites in Germany, the Netherlands, and Spain (Trigo et al., 2018).

It is worth mentioning that precise validation of ET_0 is a challenging task. The most important reason is that taking actual measurements of ET_0 over a surface corresponding to the one defined by the FAO as a reference surface is extremely difficult. Therefore, researchers use models to estimate ground-based ET_0. In this study, in situ ET_0 was calculated for 54 sites based on the widely-used Penman-Monteith method. Further, the Penman-Monteith estimated ET_0 had been compared to measured ET_0 at the Cabauw grassland site in the

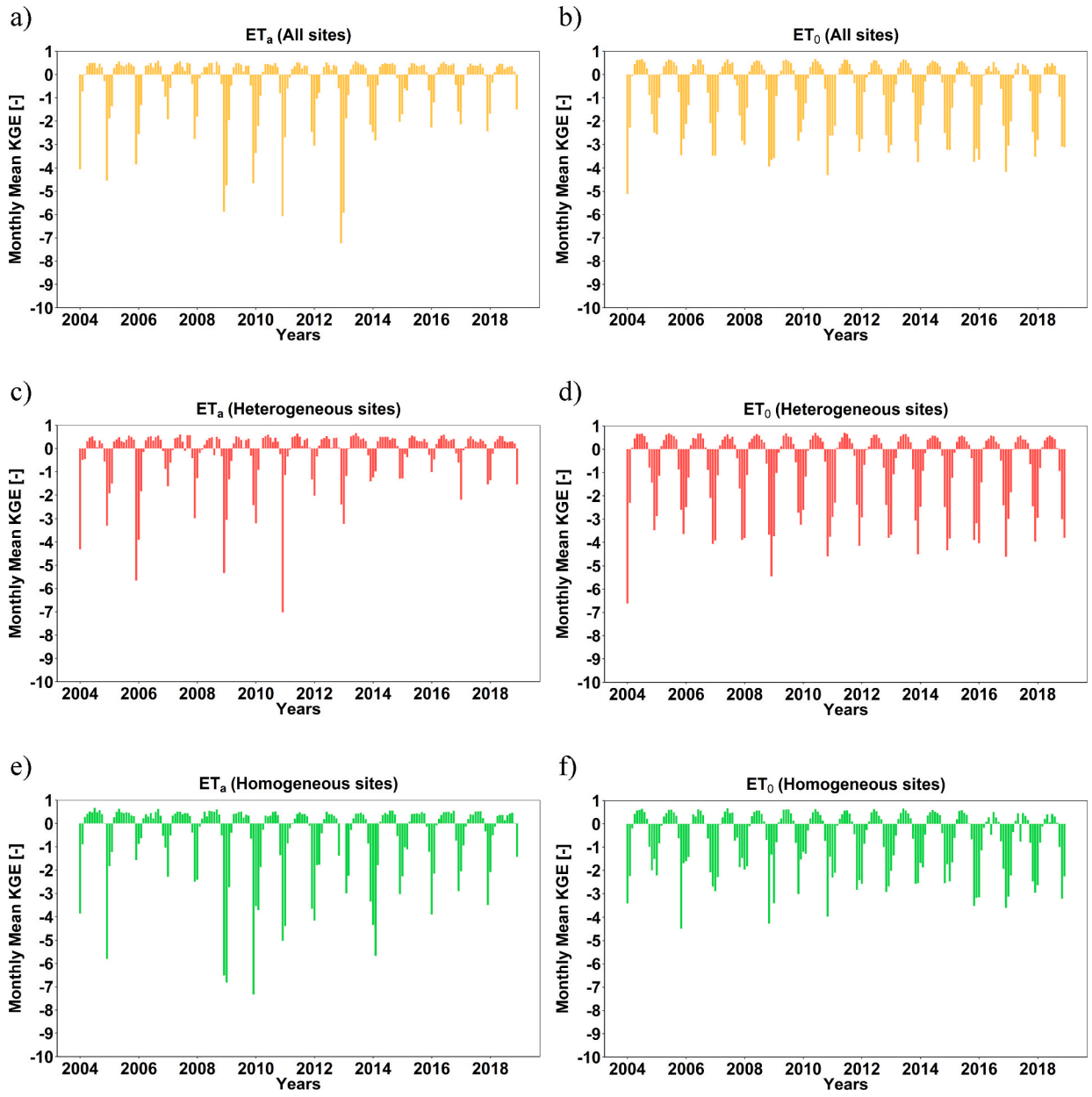

Fig. 11. SEVIRI-ET accuracies in inter-annual dimension considering all and separated (i.e., heterogeneous and homogeneous) sites; KGE barplots for SEVIRI-ET$_a$ (left panels) and SEVIRI-ET$_0$ (right panels).

Netherlands from 2007 to 2012 by Trigo et al. (2018). The Cabauw site has been identified as an ideal site that is very close to the FAO-defined reference grass. The results showed very good agreement between the Penman-Monteith calculated ET$_0$ and measured ET$_0$ at the Cabauw grass site, though Penman-Monteith slightly over-estimated the local measurements; see Fig. 3b in Trigo et al. (2018). This study is significant since it highlighted the accuracy of Penman-Monteith's estimated ET$_0$ at the Cabauw grassland site in the Netherlands (identical to FAO-defined reference grass).

A similar strategy was adopted in the EUMETSAT initial validation of SEVIRI-ET$_0$. Although a few more sites were investigated, the direct validation was performed by comparison of SEVIRI-ET$_0$ and local ET$_a$ measurements, mainly in Cabauw, where local measurements of ET$_a$ were considered identical to ET$_0$ from 2007 to 2012. Their results demonstrated good agreement between SEVIRI-ET$_0$ and measured ET$_a$ at Cabauw site (following well 1:1 line, the bias of 0.1 mm day^{-1} and standard deviation of 0.3 mm day^{-1} (Trigo and DeBruin, 2016). Similar to the SEVIRI-ET$_a$ case, the current study takes one step forward and continues the SEVIRI-ET$_0$ accuracy assessment from 2004 and extends the validation exercise till 2018.

5.2. SEVIRI-ET accuracy in temporal dimensions

The current study further explored the spatial and temporal dimensions aspects of daily SEVIRI-ET accuracy, which were not addressed in existing research. A validation of SEVIRI-ET against in situ ET measurements at selected sites, consistency check with dependent variables (e.g., land surface temperature), and ET products (models) inter-comparisons were widely explored (Ghilain et al., 2011, 2017, 2018; Hu et al., 2015b; Majozi et al., 2017; Trigo et al., 2018). These studies did not investigate the temporal dimension of accuracy, possibly due to the lack of long-term in situ measurements.

The current study separated the SEVIR-ET accuracy into the intra-annual (temporal) dimension. We found that SEVIRI-ET had a lower

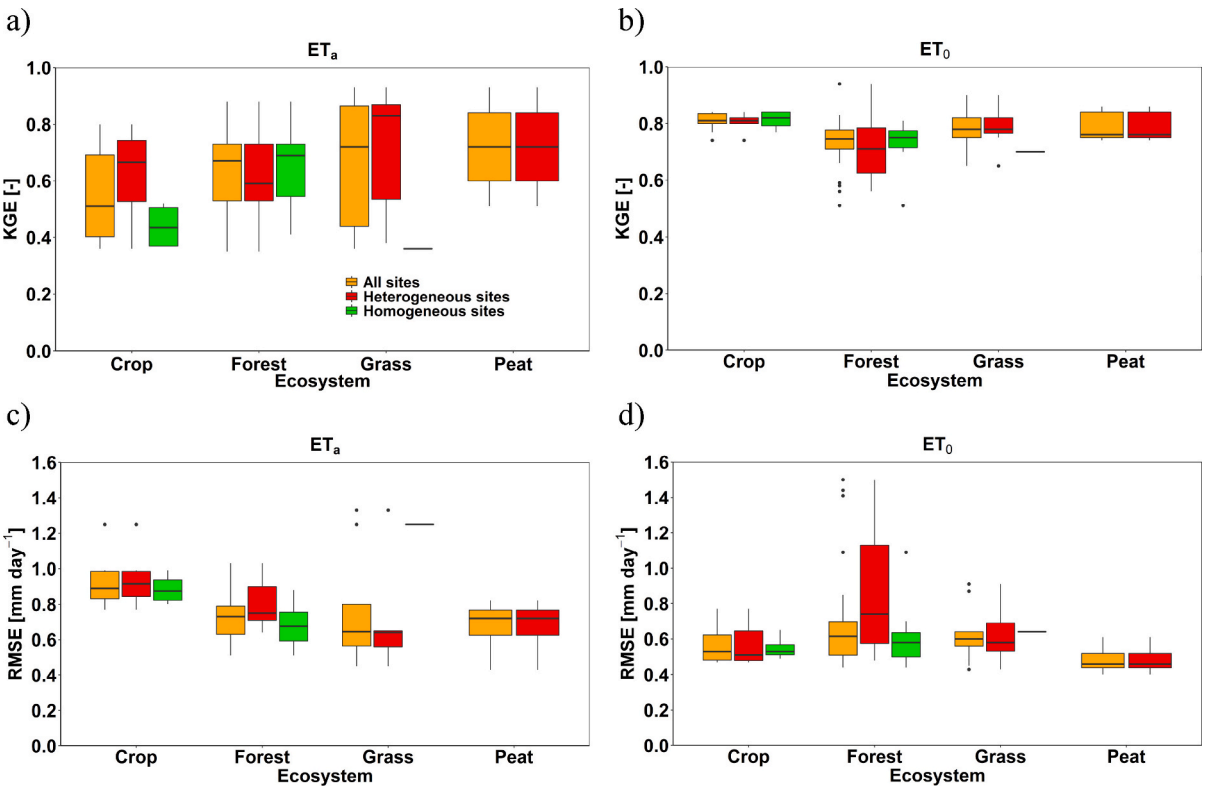

Fig. 12. SEVIRI-ET$_a$ accuracies in the ecosystem dimension considering all and separated (i.e., heterogeneous and homogeneous) sites; KGE and RMSE boxplots for SEVIRI-ET$_a$ (left panels) and SEVIRI-ET$_0$ (right panels).

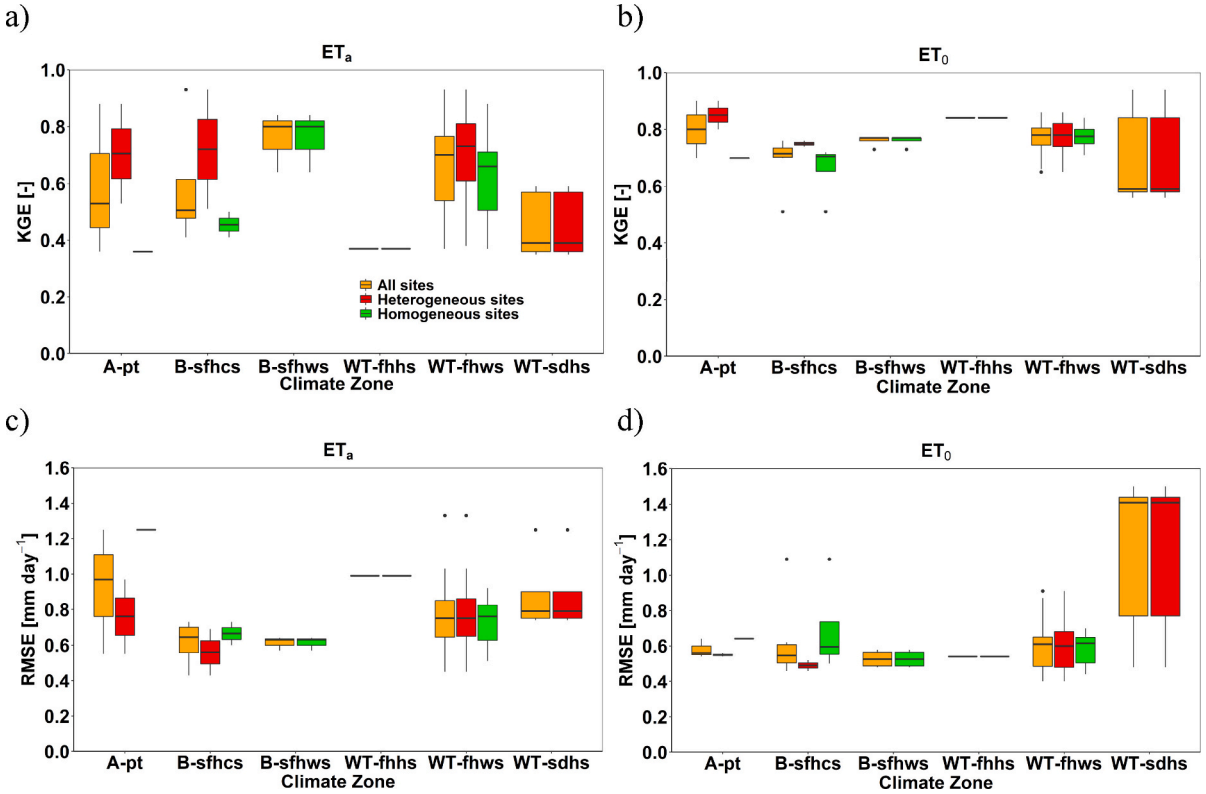

Fig. 13. SEVIRI-ET$_a$ accuracies in climate dimension considering all and separated (i.e., heterogeneous and homogeneous) sites; KGE and RMSE boxplots for SEVIRI-ET$_a$ (left panels) and SEVIRI-ET$_0$ (right panels).

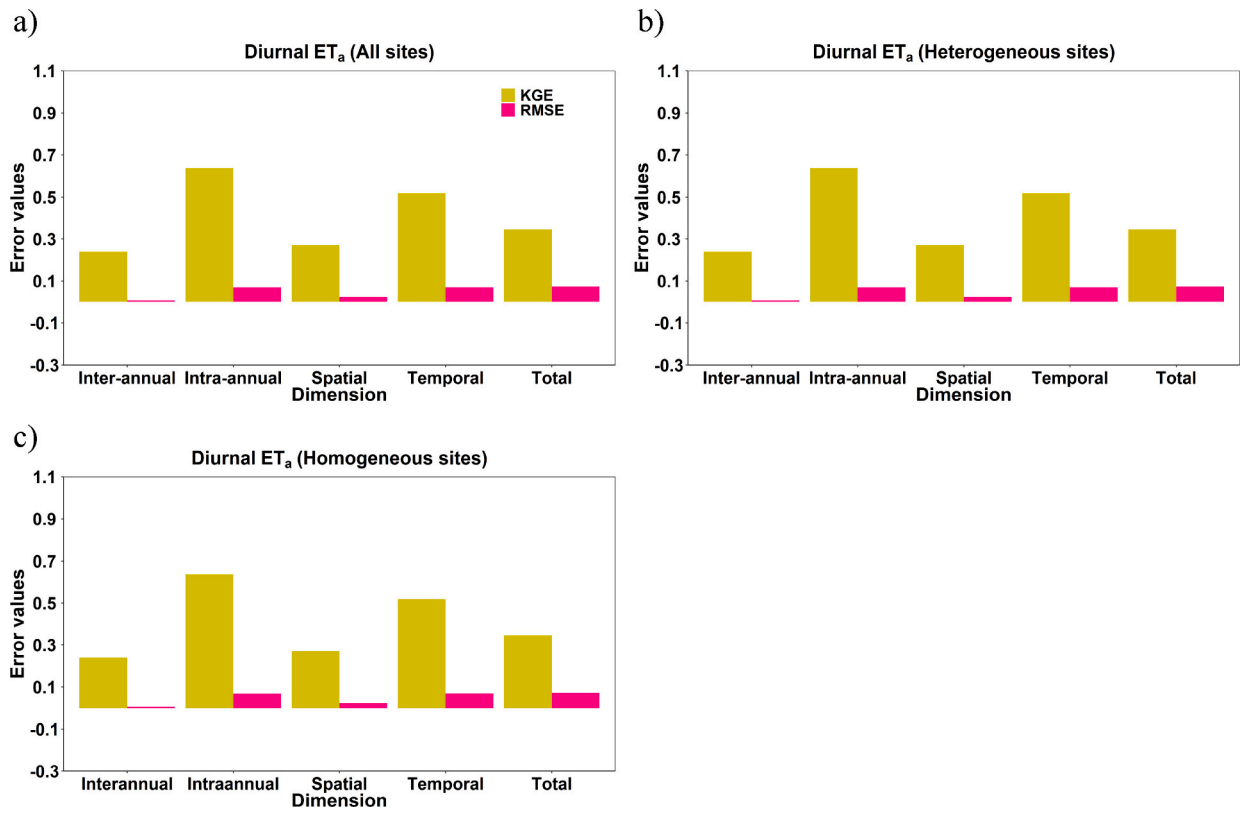

Fig. 14. Sub-daily SEVIRI-ET$_a$ total accuracy (KGE [−] and RMSE [mm hour^{-1}]) decomposition for spatial and temporal dimensions considering (a) all, (b) heterogeneous, and (c) homogeneous sites.

accuracy (larger errors) in the first and the last quarter of the year (Fig. 10) but higher accuracy (lower errors) in mid-year. The SEVIRI-ET data accuracy changed considerably on an annual basis, suggesting that one may not rely on an accuracy report derived from a smaller portion of in situ measurements taken in a shorter episode during the year (e.g., a few consecutive months). Therefore, a fair temporal distribution of the in situ measurements within the year to cover the four quarters is required as the minimum to ensure an unbiased accuracy assessment. Lower accuracy (i.e., lower KGE in Fig. 10) in SEVIRI-ET products in the first and last quarter of the year might be attributed to the weather and environmental conditions in Europe, forcing the absolute values and variability of ET and its drivers to be smaller in winter. However, observing good accuracy for SEVIRI-ET estimates in the mid-year has a practical implication for those applications that require higher accuracy SEVIRI-ET data in the growing season (e.g., crop productivity analysis and agricultural water stress detection).

Investigating inter-annual dimensions of the SEVIRI-ET accuracy from 2004 to 2018, we found that the accuracy of SEVIRI-ET$_a$ varied considerably between years. The change of accuracy was strongly pronounced in the mid-year positive KGE values from one year to another (Fig. 11: left panels). However, this was not the case in the accuracy of SEVIRI-ET$_0$ results since a similar trend and stable temporal profiles were found for SEVIRI-ET$_0$, especially for the mid-year positive KGE values from 2004 to 2018 (Fig. 11: right panels). This demonstrated that SEVIRI-ET$_a$ estimates are being affected by crop characteristics and environmental conditions (as opposed to ET$_0$, which is only affected by atmospheric demand).

5.3. SEVIRI-ET accuracy in spatial dimensions

In the ecosystem dimension, satisfactory agreement (the median $R^2 \approx 0.77$) was observed between SEVIRI-ET$_a$ and in situ ET$_a$ across ecosystems. This is consistent with the mean correlation of 0.78, reported in the initial validation exercise for daily SEVIRI-ET$_a$ (Ghilain et al., 2018). Furthermore, our results are comparable to previously performed validation exercises. For instance, the direct comparison of daily SEVIRI-ET$_a$ and in situ ET$_a$ at six sites located in different ecosystems (e.g., cropland, forest, shrubland, grassland, and diverse forests) of Spain and Italy in 2011 demonstrated a close agreement (index of agreement = 0.75) among all sites (Petropoulos et al., 2015). In another study, a range of acceptable correlations (R^2: 0.56–0.9) was reported for various ecosystems (e.g., grassland and forest) resulting from the comparison between SEVIRI-ET and in situ ET at hourly time step in Europe (Ghilain et al., 2011).

A further validation exercise designed to assess the quality of half-hourly SEVIRI-ET$_a$ over 16 sites in Europe, distributed in different types of land covers (e.g., grassland, various types of forest, and cropland), showed a high correlation ($R^2 > 0.7$) for most of the investigated sites, and error values remained within the range of observations uncertainty (Gellens-Meulenberghs et al., 2012). We found that grasslands, and peatlands (in Fig. 12a) had comparatively higher KGE median values in SEVIRI-ET$_a$ compared to forests and croplands. This could show that natural ecosystems with shorter canopy heights and less vegetation coverage may have higher levels of agreement between SEVIRI-ET$_a$ and measured ET$_a$ compared to ecosystems with closed and denser canopies (greater biomass). Similar findings were also reported for SEVIRI-ET$_a$ in previous studies, though with a limited number of six observations (Petropoulos et al., 2015). Moreover, the highest agreement was found between SEVIRI-ET$_0$ and in situ ET$_0$, in grasslands and croplands ecosystems, while the lowest agreement was obtained in forest ecosystems. In this case, it might be attributed to the fact that grasslands and croplands are closer to the hypothetical FAO-defined surface compared to forests.

Grouping the accuracies based on climate zone, we found that both SEVIRI-ET$_a$ and SEVIRI-ET$_0$ algorithms reproduced in situ ET$_a$ and ET$_0$ variations in most of the climate zones in Europe. This finding is in line

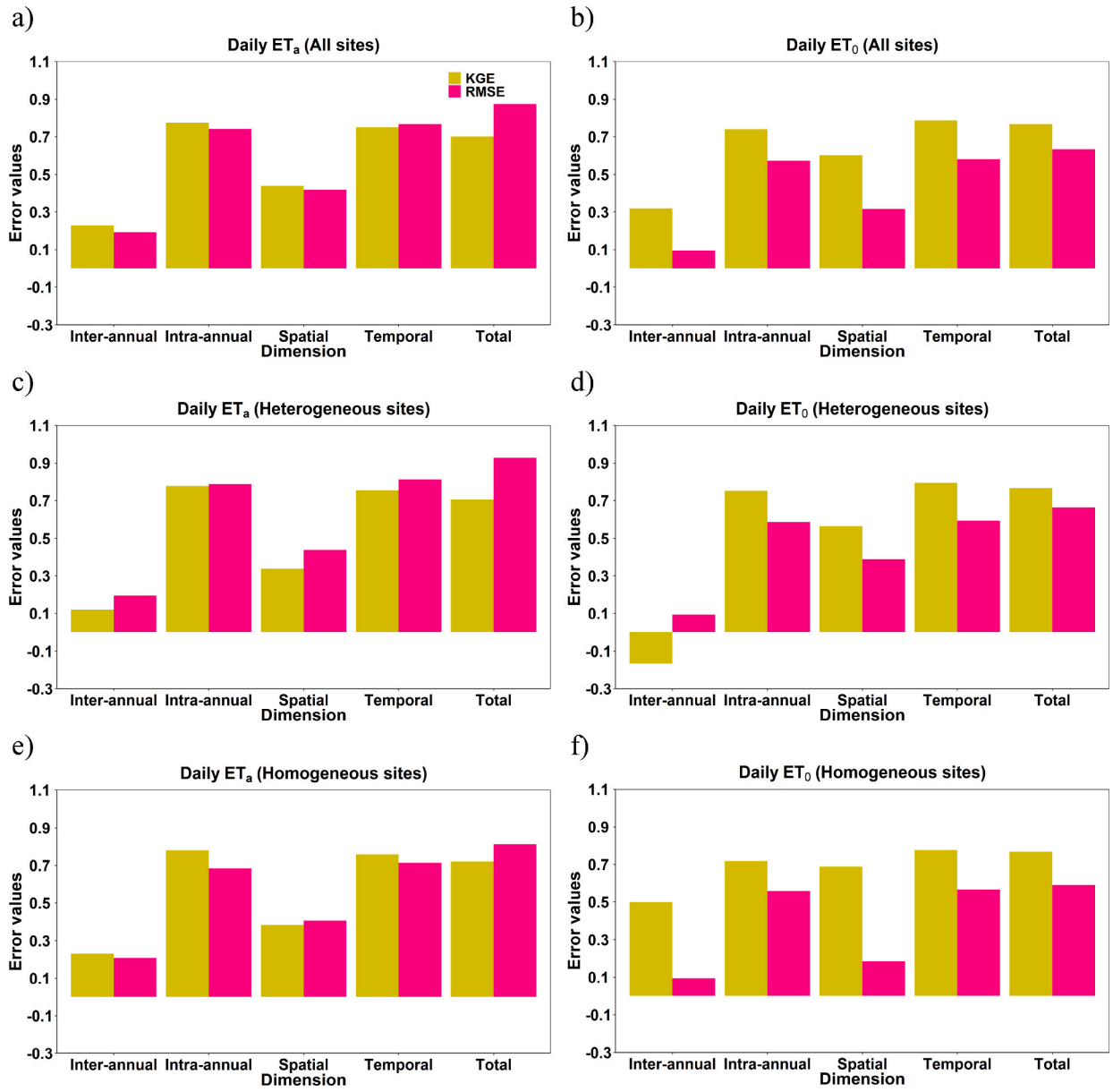

Fig. 15. SEVIRI-ET$_a$ (left panels) and SEVIRI-ET$_0$ (right panels) total accuracy (KGE [−] and RMSE [mm day^{-1}]) decomposition for spatial and temporal dimensions considering all and separated (i.e., heterogeneous and homogeneous) sites.

with the validation exercise performed for SEVIRI-ET$_a$ for 2007–2011 (Ghilain et al., 2018) where good agreement was reported between SEVIRI-observed and ground-measured latent heat flux in sites sampling broad climates (i.e., Mediterranean, Temperate and Boreal climates). However, lower agreement (and high errors) was observed for the Warm Temperate summer dry hot summer (WT-sdhs) for both SEVIRI-ET$_a$ (Fig. 13a) and SEVIRI-ET$_0$ (Fig. 13b). One possible reason, or at least a hint, might be related to the difficulties in the partitioning of sensible and latent heat fluxes in the ET$_a$ algorithm (for SEVIRI-ET$_a$) and the estimation of the net radiation over the (reference) grass surface (for SEVIRI-ET$_0$) in this specific climate zone. Remote sensing ET models, usually do not keep track of the water budget in soil and vegetation and does not contain an explicit parametrization of the effects of soil moisture variations on the stomatal conductance. Therefore, soil moisture effects are only manifest if the lack of soil moisture affects the optical or thermal appearance of the vegetation. Therefore, estimation of ET from optical and thermal satellite observations is more challenging and considerably biased in water-limited regions (Bayat et al., 2019; Gökmen et al., 2012). However, more research is still required to understand the procedure and gain more information.

5.4. *Decomposition of diurnal and daily SEVIRI-ET error*

Decomposition of total RMSE and KGE can provide information about the accuracy of SEVIRI-ET in each of the dimensions by removing the impacts of the other dimensions. A dimension is “better captured” when both RMSE is small, and KGE is high. In most of the cases, for instance, Fig. 14, we obtained lower RMSE and relatively higher KGE in single dimensions. However, there might be some cases where RMSE and KGE are not in agreement (RMSE improved while KGE deteriorated), for instance see the inter-annual dimension in Fig. 15c & d. This basically means that the answer depends on whether minimizing absolute/mean errors ET is more important for the application in question or nicely capturing the relative course/pattern of ET even if values and their differences are small.

Overall, from this decomposition analysis, we learned that SEVIRI-

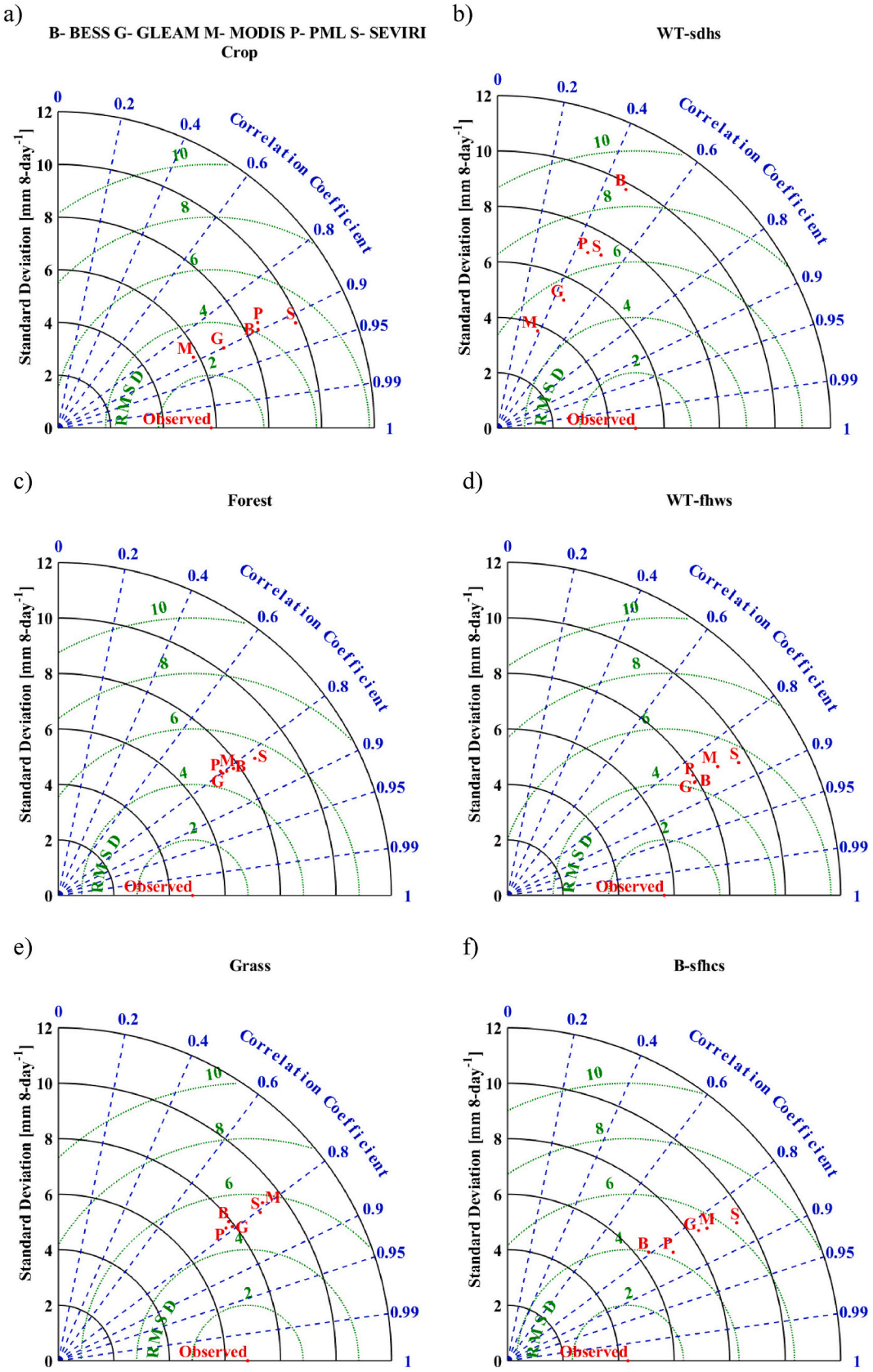

Fig. 16. Taylor diagrams illustrating the error statistics between the 8-day observed (measured) and satellite ET products (MODIS, SEVIRI, PML, GLEAM, and BESS) spanning between 2004 and 2018; Taylor diagrams for assessing the ET products at selected ecosystems (left panels) and climate zones (right panels). The azimuth indicates the correlation coefficient, the radial distance represents the standard deviation, and the semicircles centered on the "Observed" label represent the root mean standard difference (i.e., error standard deviation).

ET estimations (both at diurnal and daily steps) reflect particularly well and have higher accuracy (lower RMSE) on the mean ET per site (i.e., pure spatial dimension) compared to the time series of each site. Therefore, the spatial variability of ET is better explained in SEVIRI estimates. Moreover, SEVIRI-ET estimates showed higher accuracy in explaining the inter-annual variability compared to the intra-annual one. In other cases (e.g., inter-annual dimension for homogeneous diurnal SEVIRI-ET_a (Fig. 14c) and heterogeneous daily SEVIRI-ET_0 (Fig. 15d), particularly small (good) RMSE were accompanied by small (bad) KGE. This means that the absolute magnitude of errors improves mainly because of the small variance in the particular dimension (e.g., small inter-annual variance in contrast to large intra-annual variance), whereas the relative performance of SEVIRI-ET is actually better for the other dimension (in the above example, the intra-annual variability).

5.5. Site representativeness and heterogeneity analysis

Due to limited footprint information across EC sites, the complexity of footprint area quantification, and the limitation in the number of in situ sites, previous studies often used the in situ measurements directly to validate satellite products. They assumed that flux data collected at the tower location can still adequately represent certain fixed areas beyond the measured tower (e.g., 1 to 3 km) (Tramontana et al., 2016; Verma et al., 2015; Xiao et al., 2014). In reality, however, the fluxes measured from the EC system have limited spatial representativeness within hundreds of meters (e.g., 250–500 m), while the resolution of the space-borne observations can be in the order of several km (in the case of SEVIRI-ET, it is about 5 km). Therefore, the spatial mismatch between EC sites and satellite estimates should be considered.

We analyzed the representativeness of EC measurements and computed the SEVIRI-ET pixel purity index for all pixels surrounding the EC in situ sites considering SEVIRI subpixel land use variability. In general, we found 121 (11 × 11) MODIS pixels within each SEVIRI pixel. The results demonstrated that 24 sites out of 54 sites (44.4%) were relatively homogeneous beyond their footprint area extended up to 5 km, SEVIRI-ET spatial resolution. Our finding here is comparable with the results of Chu et al. (2021), who found that only 25% - 39% of AmeriFlux sites had similar land cover types in the areas extending kilometers far from the EC towers. These results highlight the need and the importance of in situ site representativeness analysis when performing an accuracy assessment of remote sensing estimates.

We further compared our heterogeneity analysis based on the pixel purity index with GSI for diversity. We found that GSI is in good agreement and fully supports our pixel purity results for all sites we classified as homogeneous (based on our pixel purity index). We observed that GSI values ranged between 0 and 0.44 for such homogeneous sites. However, the outcome for heterogeneous sites has to be discussed further. If one can assume GSI value of 0.44 as the threshold to define heterogeneity, the number of heterogeneous sites would decrease from 30 sites to 18 sites (and therefore, homogeneous sites would increase from 24 to 36 sites) based on GSI value. In practice, it is challenging to define a threshold to convert continuous numerical GSI values (between 0 and 1) to two discrete heterogeneity groups (i.e., relatively homogeneous and heterogeneous). This might explain the reason why in most previous studies, either all individual GSI values were analyzed (Piles et al., 2015) or at least five groups (i.e., [0–0.164], [0.164–0.304], [0.304–0.444], [0.444–0.585], [0.585–0.878]) were considered for GSI discussions (Ma et al., 2019; Qiao et al., 2022).

The GSI is heavily weighed toward the most dominant class in the pixel, and adding a few new classes with lower land cover fractions will fail to change the index. For instance, at the site DK-Sor, we observed three land covers of forest (23.6%), grass (2.7%), and crop (73.6%) inside the same SEVIRI pixel and, therefore, classified the site as heterogeneous (based on our pixel purity index), while the calculated GSI for this site is 0.40, which can be placed in the mid-range of the third group of GSI based on previous studies (Ma et al., 2019; Qiao et al., 2022). The second example is DE-Gri site, in which three land cover fractions have been detected (forest: 70.1%, crop: 27.7%, and grass: 2%). We classified this site as heterogeneous according to our pixel purity index, while the GSI suggests a value of 0.43. This might explain the reason why it introduces more homogeneous sites compared to our pixel purity index method. Obviously, at SEVIRI pixel resolution (i.e., about 5 km), all the land cover classes contribute to the ET signal, and if there are several land cover classes in a given pixel (even if with a lower fraction), one should still be careful to assign a homogeneity label for that specific pixel.

Identified homogeneous sites in the current study were assumed to be suitable for the accuracy assessment. Therefore, the evaluation of SEVIRI-ET was performed for all these homogeneous sites. However, we considered two more cases for the accuracy assessments in all five dimensions: heterogeneous sites and the combined sites (all sites including homogeneous and heterogeneous sites). This consideration has two key advantages: (i) to understand the impact of the SEVIRI-ET spatial resolution and accuracy results between homogeneous and heterogeneous sites, (ii) to be able to discuss our results in line with previous SEVIRI-ET validation exercises (and perhaps those forthcoming) where all available in situ measurements were used, independent of any representativeness analysis.

Inconsistency between accuracies among homogeneous and heterogeneous sites is related to the varying composition of land covers beyond the site footprint areas. The differences in land cover types may originate from the spatial variations of land surface properties (i.e., topography, ecology, and climatic conditions) and human impacts (i.e., land use change and irrigation). Change in land surface properties together with temporal dynamics of flux footprints, are the most important reasons behind the site heterogeneity and representativeness issue (Chu et al., 2021). Moreover, such inconsistency between the accuracies might additionally be explained by the limited numbers of representative sites in a specific class within the dimension under investigation (representativity limitation). For instance, a difference in the median KGE values and the inconsistency of the KGE trends in ecosystem dimension was observed between homogeneous and heterogonous grasslands and croplands (Fig. 12a). Besides land cover composition, these differences and inconsistencies in KGE may occur because of only a few identified homogeneous sites, which may not be sufficient for representing the grassland and cropland ecosystems. The representativity limitation was mostly an issue for SEVIRI-ET_a analysis that was also pronounced in other dimensions (e.g., climate zones).

Overall, we found that the main trends in the accuracies (median KGEs) of SEVIRI-ET remained almost similar in separated homogeneous and heterogeneous sites and were comparable to combined sites among the dimensions, albeit with possible inter-class variations, as mentioned above. The classification of EC sites as homogeneous and heterogeneous sites in the current study is done according to the criteria set, the objective we defined, the SEVIRI-ET spatial resolution, and the MODIS land cover data at 500 m resolution. Therefore, we advocate that our representativeness results may serve as a guide and could potentially be used in other studies according to the spatial scales of interest. However, the representativeness criteria might need to be adapted for specific research and desired applications. For instance, in current investigation, our emphasis centered on the analysis of pixel heterogeneity, utilizing land cover fractions as the primary foundation. Nevertheless, it is imperative to recognize that other fundamental components of the ecosystem, such as terrain characteristics, soil texture, and vegetation density, can exert significant influence on landscape heterogeneity. Therefore, it is prudent to consider these variables to develop a more comprehensive understanding of spatial heterogeneity.

It should be noted that the focus of our study was the accuracy assessment of SEVIRI-ET products in Europe. Considering SEVIRI's large coverage of data (i.e., Europe, Africa, and the eastern part of South America), the study can be extended to the entire MSG disk region. There can be limitations when it comes to the availability of reliable

ground reference data for the majority of MSG disk coverage, such as Africa and South America.

5.6. ET products intercomparison

The main intention for performing intercomparison in this study is to inform the reader about (dis)similarities between SEVIRI and four widely used open-access satellite ET products and to demonstrate the error budget of a given ET product with respect to in situ ET measurements. The intercomparison between satellite ET products was carried out at the spatial resolution of SEVIRI (0.05°). The weighted average, based on area coverage fraction, of all grid cells of MODIS, PML, and BESS products falling into the SEVIRI pixel, where the in situ station is located, has been taken into account. This is necessary to ensure a certain degree of consistency in the spatial characteristics of MODIS, PML, and BESS products with that of SEVIRI satellite. However, GLEAM ET data has been simply extracted from the pixel in which the in situ station has been located due to the coarse resolution of this product.

In general, reasonable accuracy was obtained for all ET products (i.e., SEVIRI, MODIS, PML, BESS, and GLEAM) in reproducing the in situ ET in various ecosystems and the majority of climate zones under investigation. In WT-sdhs climate zone, however, very low agreements were explored between the majority of satellite ET products and in situ ET. This might be attributed to the difficulties in the partitioning of sensible and latent heat fluxes in the remote sensing ET_a algorithms and models in this specific climate zone (as discussed in section 5.3). Our finding here is in agreement with previous studies where large dissimilarities have been reported for satellite ET estimates in arid regions and water stress conditions, for instance in MODIS, and PML (Elnashar et al., 2021) and MODIS and GLEAM ET products (Miralles et al., 2016; Weerasinghe et al., 2020).

We found that SEVIRI ET_a estimates outperformed other ET products under investigation in this study in terms of higher correlation with the in situ ET_a measurements. This might partly be related to the extensive sampling interval of the SEVIRI satellite due to the fact that SEVIRI 8-day ET_a estimates are based on original higher temporal resolution instantaneous observations that are available at sub-daily (half-hourly) steps. However, the higher standard deviation error of 8-day SEVIRI ET compared to other satellite ET products might also be partially explained by such extensive sampling and their associated errors in the instantaneous SEVIRI ET products.

Taylor diagram results suggest that there is no single satellite product that can perform best for all cases (e.g., ecosystems and climate zones). A similar conclusion has been drawn in previous studies where more global ET products have been evaluated (Elnashar et al., 2021; Li et al., 2018; Vinukollu et al., 2011). This is understandable and can be explained by the fact that satellite ET products cannot detect the whole range of values and the day-to-day variations precisely, and therefore, many satellite ET products carry a considerable amount of bias (Weerasinghe et al., 2020).

6. Conclusions

A comprehensive accuracy assessment were carried out on diurnal (sub-daily) SEVIRI-ET_a and daily SEVIRI-ET estimates, encompassing both ET_a and ET_0, utilizing all available data acquired between 2004 and 2018. This evaluation was conducted across 54 selected EC sites in Europe. In addition to assessing the accuracy of SEVIRI-ET estimates at individual site levels for both diurnal and daily SEVIRI-ET, we also examined accuracy across two spatial dimensions (ecosystem and climate zone), two temporal dimensions (intra-annual and inter-annual), and conducted a general intercomparison with four widely-used satellite ET products (BESS, PML, MODIS, and GLEAM). The evaluation of diurnal and daily SEVIRI-ET products was mainly based on direct validation against corresponding in situ ET_a and ET_0 at diurnal and daily time steps. Prior to our assessment, we conducted a spatial analysis at a sub-pixel level to evaluate the homogeneity and heterogeneity of SEVIRI pixels across all 54 EC sites. This analysis utilized 0.004° resolution MODIS land cover data. The representativeness analysis aimed to quantify the accuracy of SEVIRI-ET_a and SEVIRI-ET_0 within three sub-groups (homogeneous, heterogeneous, and a combined dataset) concerning the spatial and temporal dimensions mentioned earlier.

The validation results demonstrated, in general, close agreement between diurnal and daily in situ ET with their correspondence SEVIRI-ET, for both ET_a and ET_0 products. At the diurnal step, higher accuracy for SEVIRI-ET_a was obtained in the summer and during the day time. The accuracies for daily SEVIRI-ET_a and SEVIRI-ET_0 estimates improved significantly. However, variations were found for SEVIRI-ET accuracy in both temporal and spatial dimensions. For SEVIRI-ET_a, we found that intra-annual accuracy was low in the first quarter of the year, increased in the mid-year (the second and third quarter), and then began to decline in the last quarter. Although accuracy remained relatively stable during the mid-year, it varied considerably in the first and the last quarter. Moreover, inter-annual variations were observed in the mid-year positive median KGE values over time for the period 2004–2018. At spatial dimensions, our findings revealed that the highest accuracy was achieved in the peatland and grassland ecosystems, while the lowest accuracy was observed in the cropland ecosystem. Similarly, the Boreal snow fully humid warm summer climate zone exhibited the highest accuracy, whereas the warm temperate fully humid hot summer climate zone had the lowest accuracy. For SEVIRI-ET_0, we noticed that the intra-annual accuracy displayed a comparable trend to what was observed for SEVIRI-ET_a. Specifically, accuracy was low and unstable during the first quarter and the last quarter of the year but showed high and stable performance in the mid-year. Further, we observed an almost identical pattern in the mid-year positive KGE values, indicating a slight variation in SEVIRI-ET_0 accuracy during the period from 2004 to 2018. At spatial dimensions, we found that the highest accuracy was achieved in crop ecosystem, while the lowest accuracy was observed in forest ecosystem. Similarly, the warm temperate fully humid hot summer climate zone exhibited the highest accuracy, whereas the warm temperate summer dry hot summer climate zone had the lowest accuracy.

The error decomposition results revealed that SEVIRI-ET_a estimates (both diurnal and daily products) performed particularly well in explaining inter-annual and spatial variabilities compared to intra-annual and temporal variabilities. We found variations in the SEVIRI-ET accuracy, separating all (100%) sites into homogeneous (44.4%) and heterogonous (55.6%) ones at SEVIRI-ET_a spatial resolution. However, the main trends in the accuracies (median KGEs) remained similar in separated sites and were comparable to combined sites among the dimensions. ET products intercomparison demonstrated that SEVIRI satellite outperformed the other ET products in terms of achieving the highest (the best) correlation across all ecosystem types and climate zones. However, the lower (better) standard deviation error, and therefore, ET estimates closer to the in situ measurements, were observed for PML (in forest and grass ecosystems), MODIS (in crop ecosystem and WT-sdhs climate zone), GLEAM (in forest ecosystem and WT-fhws climate zone) and BESS (in B-sfhcs climate zone) products.

CRediT authorship contribution statement

Bagher Bayat: Conceptualization, Methodology, Software, Visualization, Writing – original draft, Writing – review & editing. **Rahul Raj:** Methodology, Software, Writing – review & editing. **Alexander Graf:** Methodology, Writing – review & editing. **Harry Vereecken:** Methodology, Writing – review & editing. **Carsten Montzka:** Methodology, Writing – review & editing.

Declaration of Competing Interest

The authors declare that they have no known competing financial

interests or personal relationships that could have appeared to influence the work reported in this paper.

Acknowledgments

This work was supported by the European Commission HORIZON 2020 Program ERA-PLANET/GEOEssential project [grant number: 689443], the German Federal Ministry of Education and Research (BMBF) H_2ATLAS-AFRICA [grant number: 03EW0001A] and the Dragon 5 programme [grant number: 59197]. We would like to thank Dr. Thomas Poméon from (formerly) Forschungszentrum Jülich GmbH and (currently) Deutsche Telekom IT GmbH, for his fruitful discussions and valuable support in the course of this study. Moreover, we would like to acknowledge EUMETSAT LSA SAF for granting us access to the full archive of SEVIRI-ET data. Especial thanks to helpdesk team in the LSA SAF for all their support during this research. The authors extend their gratitude to the editors and three anonymous reviewers for their valuable comments and suggestions, which have significantly contributed to enhancing the quality of our paper.

We extend our appreciation to the developers and contributors of the crucial R packages utilized in this study. The data analysis and visualization processes were significantly facilitated by the implementation of the following packages: ncdf4 (Pierce, 2019), rhdf5 (Fischer et al., 2019), rgeos (Bivand and Rundel, 2019), dplyr (Wickham et al., 2020), ggplot2 (Wickham, 2016), lubridate (Grolemund and Wickham, 2011), tidyverse (Wickham et al., 2019), and hydroGOF (Zambrano-Bigiarini, 2020). Their functionalities enabled comprehensive data extraction, exploration, effective visualization, and error budget analysis throughout the course of our research.

For the in situ station data, the authors thank the Ecosystem Thematic Centre of the ICOS Research Infrastructure and all station PIs, in particular Anne Klosterhalfen, Nicola Arriga, Christian Bernhofer, Frédéric Bornet, Christian Brümmer, Nina Buchmann, Jinshu Chi, Christophe Chipeaux, Edoardo Cremonese, Matthias Cuntz, Jiří Dušek, Tarek S. El-Madany, Silvano Fares, Milan Fischer, Lenka Foltýnová, Mana Gharun, Shiva Ghiasi, Bert Gielen, Pia Gottschalk, Thomas Grünwald, Günther Heinemann, Bernard Heinesch, Michal Heliasz, Jutta Holst, Lukas Hörtnagl, Andreas Ibrom, Joachim Ingwersen, Gerald Jurasinski, Janina Klatt, Alexander Knohl, Franziska Koebsch, Jan Konopka, Mika Korkiakoski, Natalia Kowalska, Pascal Kremer, Bart Kruijt, Sebastien Lafont, Joël Léonard, Anne De Ligne, Bernard Longdoz, Denis Loustau, Vincenzo Magliulo, Ivan Mammarella, Giovanni Manca, Matthias Mauder, Mirco Migliavacca, Meelis Mölder, Johan Neirynck, Patrizia Ney, Mats Nilsson, Eugénie Paul-Limoges, Matthias Peichl, Andrea Pitacco, Arne Poyda, Corinna Rebmann, Marilyn Roland, Torsten Sachs, Marius Schmidt, Frederik Schrader, Lukas Siebicke, Ladislav Šigut, Eeva-Stiina Tuittila, Andrej Varlagin, Nadia Vendrame, Caroline Vincke, Ingo Völksch, Stephan Weber, Christian Wille, Hans-Dieter Wizemann, Matthias Zeeman and the funding sources French National Research Agency ANR (ANR-11-LABX-0002-01, ANR-16-SUMF-0001-01, LabEx ARBRE), AnaEE-France (https://www.anaee-france.fr/en/) including ACBB (Agro-écosystèmes, Cycles Biogéochimiques et Biodiversité, http://www.soere-acbb.com/), Alexander von Humbold Stiftung (MaNiP), German Federal Ministry of Education and Research BMBF (01LN1313A), German Federal Ministry of Food and Agriculture BMEL (ERA-NET FACCE ERAGAS), German Research Foundation DFG (BE1721/23, PAK 346, FOR 1695, INST 186/1118-1 FUGG), GIP Ecofor SOERE F-ORE-T, Finnish Center of Excellence (307331), Research Foundation-Flanders FWO (G0H3317N), Hainich National Park, Helmholtz Association HGF (TERENO, VH-NG-821), Horizon 2020 (696356), ICOS-FINLAND (281255), Kempe Foundation (SMK-1743), Knut and Alice Wallenberg Foundation (2015.0047), Max-Planck Institute for Biogeochemistry, Russian Foundation for Basic Research RFBR (19-04-01234-a), Swiss National Science Foundation (ICOS-CH Phase 2 20FI20_173691, InnoFarm 407340_172433), European Commission (SUPER-G, RINGO, ERA-NET Sumforest No. 606803), Service Public de Wallonie (DGO6, 1217769), SustES (CZ.02.1.01/0.0/0.0/16_019/0000797), the Czech Ministry of Education, Youth and Sports (CzeCOS grant no. LM2018123), Swedish Research Council FORMAS (2016-01289, 942-2015-49) and University of Padua (CDPA148553, 2014).

Appendix A. Additional information and extra details

Table A1 provides an overview of the 54 sites included in this study (Section 2.2), along with their essential characteristics. Tables A2 and A3 contain legend descriptions for the MODIS land cover map (Fig. 4a) and the climate zone map (Fig. 4b), respectively. Table A4 presents the results of the SEVIRI pixel homogeneity analysis (Section 4.1) conducted on the 54 selected sites across Europe. Finally, Table A5 presents information on extracted ecosystem types and climate zones (Section 4.2) for the same 54 European sites.

Table A1
Overview of 54 sites used in this study and their essential characteristics, adopted from (Graf et al., 2020). The period of the in situ measurements is 2004–2018.

Site	Longitude (°)	Latitude (°)	Ecosystem	Mean annual temperature (°C)	Mean annual precipitation (mm)	Elevation (m)	Reference
BE-Bra	4.52	51.31	forest	9.8	750	16	(Gielen et al., 2013)
BE-Lon	4.75	50.55	crop	10	800	167	(Buysse et al., 2017)
BE-Vie	6	50.3	forest	7.8	1062	493	(Aubinet et al., 2018)
CH-Aws	9.79	46.58	grass	2.3	918	1978	(Zeeman et al., 2010)
CH-Cha	8.41	47.21	grass	9.5	1136	400	(Hörtnagl et al., 2018)
CH-Dav	9.86	46.82	forest	3.5	1046	1639	(Haeni et al., 2017)
CH-Fru	8.54	47.12	grass	7.2	1651	982	(Zeeman et al., 2010)
CH-Lae	8.36	47.48	forest	8.7	1211	689	(Haeni et al., 2017)
CH-Oe2	7.73	47.29	crop	9.8	1155	452	(Emmel et al., 2018)
CZ-BK1	18.54	49.5	forest	6.7	1316	875	(Krupková et al., 2017)
CZ-Lnz	16.95	48.68	forest	9.3	550	150	(Acosta et al., 2017)
CZ-RAJ	16.7	49.44	forest	7.1	681	625	(McGloin et al., 2018)
CZ-Stn	17.97	49.04	forest	8.7	685	550	(Krupková et al., 2019)
CZ-wet	14.77	49.02	peatland	7.7	604	425	(Dušek et al., 2012)
DE-BER	13.32	52.46	grass	9.4	525	61	(Heusinger and Weber, 2017)
DE-EC2	8.71	48.93	crop	9.4	889	318	(Poyda et al., 2019)
DE-EC4	9.77	48.53	crop	7.5	1064	687	(Wizemann et al., 2015)
DE-Fen	11.06	47.83	grass	8.4	1081	595	(Kiese et al., 2018)
DE-Geb	10.91	51.1	crop	8.5	470	162	(Anthoni et al., 2004)
DE-Gri	13.51	50.95	grass	7.8	901	385	(Prescher et al., 2010)

(continued on next page)

Table A1 (*continued*)

Site	Longitude (°)	Latitude (°)	Ecosystem	Mean annual temperature (°C)	Mean annual precipitation (mm)	Elevation (m)	Reference
DE-Hai	10.45	51.08	forest	8.3	720	440	(Knohl et al., 2003)
DE-HoH	11.22	52.09	forest	9.1	563	193	(Wollschläger et al., 2017)
DE-Kli	13.52	50.89	crop	7.6	842	478	(Prescher et al., 2010)
DE-Obe	13.72	50.79	forest	5.5	996	734	(Prescher et al., 2010)
DE-RbW	10.97	47.73	grass	9.0	1160	769	(Kiese et al., 2018)
DE-RuR	6.3	50.62	grass	7.7	1033	515	(Post et al., 2015)
DE-RuS	6.45	50.87	crop	10.2	718	103	(Klosterhalfen et al., 2019)
DE-RuW	6.33	50.5	forest	7.5	1250	610	(Ney et al., 2019)
DE-SfS	11.33	47.81	peatland	8.6	1127	590	(Hommeltenberg et al., 2014)
DE-Tha	13.57	50.96	forest	8.2	843	380	(Prescher et al., 2010)
DE-ZRK	12.89	53.88	peatland	8.7	584	1	(Franz et al., 2016)
DK-Sor	11.64	55.49	forest	8.2	660	40	(Wu et al., 2013)
ES-Abr	−6.79	38.7	forest	16	400	280	(Luo et al., 2018)
ES-LM1	−5.78	39.94	forest	16	700	265	(El-Madany et al., 2018)
ES-LM2	−5.78	39.93	forest	16	700	270	(El-Madany et al., 2018)
FI-Hyy	24.29	61.85	forest	3.8	709	180	(Mammarella et al., 2009)
FI-Let	23.96	60.64	forest	4.6	627	0	(Launiainen et al., 2016)
FI-Sii	24.19	61.83	peatland	3.5	701	160	(Rinne et al., 2018)
FI-Var	29.61	67.75	forest	−0.5	601	395	(Kulmala et al., 2019)
FR-Bil	−0.96	44.49	forest	12.8	930	0	(Moreaux et al., 2011)
FR-EM2	3.02	49.87	crop	10.8	680	84	(Domeignoz-Horta et al., 2015)
FR-Hes	7.06	48.67	forest	9.2	820	300	(Granier et al., 2008)
IT-BCi	14.96	40.52	crop	18	600	15	(Vitale et al., 2009)
IT-Lsn	12.75	45.74	crop	13.1	1083	1	(Tezza et al., 2019)
IT-SR2	10.29	43.73	forest	14.2	920	4	(Hoshika et al., 2017)
IT-Tor	7.58	45.84	grass	2.9	920	2160	(Galvagno et al., 2013)
NL-Loo	5.74	52.17	forest	9.8	786	25	(Elbers et al., 2011)
RU-Fy2	32.9	56.45	forest	3.9	711	265	(Esquinas-Requena et al., 2020)
RU-Fyo	32.92	56.46	forest	3.9	711	265	(Kurbatova et al., 2013)
SE-Deg	19.56	64.18	peatland	1.2	523	270	(Nilsson et al., 2008)
SE-Htm	13.42	56.1	forest	7.4	707	115	(van Meeningen et al., 2017)
SE-Nor	17.48	60.09	forest	5.5	527	46	(Lindroth et al., 2018)
SE-Ros	19.74	64.17	forest	1.8	614	160	(Jocher et al., 2018)
SE-Svb	19.77	64.26	forest	1.8	614	270	(Chi et al., 2019)

Table A2
The legend descriptions of MODIS land cover map (Fig. 2b), adopted from (https://developers.google.com/earth-engine/datasets/catalog/MODIS_006_MCD12Q1#bands; last access: 1 July 2023).

Land cover class on the map	Description of the class
WB	Water Bodies: at least 60% of area is covered by permanent water bodies
ENT	Evergreen Needleleaf Trees: dominated by evergreen conifer trees (>2 m). Tree cover >10%
EBT	Evergreen Broadleaf Trees: dominated by evergreen broadleaf and palmate trees (>2 m). Tree cover >10%.
DNT	Deciduous Needleleaf Trees: dominated by deciduous needleleaf (larch) trees (>2 m). Tree cover >10%.
DBT	Deciduous Broadleaf Trees: dominated by deciduous broadleaf trees (>2 m). Tree cover >10%.
S	Shrub: Shrub (1-2 m) cover >10%.
G	Grass: dominated by herbaceous annuals (<2 m) that are not cultivated.
CC	Cereal Croplands: dominated by herbaceous annuals (<2 m). At least 60% cultivated cereal crops.
BC	Broadleaf Croplands: dominated by herbaceous annuals (<2 m). At least 60% cultivated broadleaf crops.
UBL	Urban and Built-up Lands: at least 30% impervious surface area including building materials, asphalt, and vehicles.
PSI	Permanent Snow and Ice: at least 60% of area is covered by snow and ice for at least 10 months of the year.
NVL	Non-Vegetated Lands: at least 60% of area is non-vegetated barren (sand, rock, soil) with <10% vegetation.

Table A3
The legend descriptions of Koppen-Geiger climate zone version 2017 (Fig. 3b), adopted from (http://koeppen-geiger.vu-wien.ac.at/present.htm; last access: 1 July 2023).

Land cover class on the map	Description of the class
BSh	Arid_Steppe_hot arid
BSk	Arid_Steppe_cold arid
BWh	Arid_desert_hot arid
BWk	Arid_desert_cold arid
Cfa	Warm Temperate_fully humid_hot summer
Cfb	Warm Temperate_fully humid_warm summer
Cfc	Warm Temperate_fully humid_cool summer
Csa	Warm Temperate_steppe_hot summer
Csb	Warm Temperate_summer dry_warm summer

(*continued on next page*)

Table A3 (*continued*)

Land cover class on the map	Description of the class
Csc	Warm Temperate_ summer dry _cool summer
Dfa	Boreal (Snow_fully humid_hot summer)
Dfb	Boreal (Snow_fully humid_warm summer)
Dfc	Boreal (Snow_fully humid_cool summer)
Dsb	Boreal (Snow_summer dry_warm summer)
Dsc	Boreal (Snow_ summer dry_cool summer)
ET	Alpine (Polar_polar tundra)
Ocean	Ocean

Table A4
SEVIRI pixel homogeneity analysis of 54 sites selected across Europe. The pixel purity index and GSI for diversity were calculated for the SEVIRI pixels surrounding flux towers using MODIS land cover data. The heterogeneity status of the sites was identified based on the pixel purity index and criteria set (section 3.2). The homogeneity failed criteria was also identified in this Table as: (1) more than two natural land cover types found within the SEVIRI pixel, (2) pixel purity was lower than 65%, (3) both more than two natural land cover types found within the SEVIRI pixel and pixel purity was lower than 65%, (4) MODIS-derived dominant land cover type was different than reported ecosystem type for the given site.

Site	Site ecosystem	Pixel purity index (%)	Gini-Simpson index (−)	Homogeneous
BE-Bra	forest	66.67	0.44	Yes
BE-Lon	crop	93.75	0.12	Yes
BE-Vie	forest	99.31	0.01	Yes
CH-Aws	grass	86.11	0.24	Yes
CH-Cha	grass	70.83	0.43	No[1]
CH-Dav	forest	50.69	0.50	No[2]
CH-Fru	grass	89.58	0.19	No[4]
CH-Lae	forest	65.97	0.52	No[1]
CH-Oe2	crop	64.58	0.47	No[3]
CZ-BK1	forest	100.00	0.00	Yes
CZ-Lnz	forest	97.92	0.04	Yes
CZ-RAJ	forest	60.42	0.56	No[3]
CZ-Stn	forest	100.00	0.00	Yes
CZ-wet	peatland	40.28	0.69	No[3]
DE-BER	grass	100.00	0.00	No[4]
DE-EC2	crop	64.58	0.52	No[3]
DE-EC4	crop	52.08	0.56	No[3]
DE-Fen	grass	72.22	0.40	No[4]
DE-Geb	crop	100.00	0.00	Yes
DE-Gri	grass	70.14	0.43	No[1]
DE-Hai	forest	94.44	0.10	Yes
DE-HoH	forest	52.08	0.50	No[2]
DE-Kli	crop	50.00	0.59	No[3]
DE-Obe	forest	89.58	0.19	Yes
DE-RbW	grass	72.92	0.39	No[4]
DE-RuR	grass	83.33	0.28	No[4]
DE-RuS	crop	59.03	0.55	No[3]
DE-RuW	forest	100.00	0.00	Yes
DE-SfS	peatland	79.86	0.33	No[4]
DE-Tha	forest	49.31	0.58	No[3]
DE-ZRK	peatland	58.33	0.57	No[3]
DK-Sor	forest	73.61	0.40	No[1]
ES-Abr	forest	100.00	0.00	No[4]
ES-LM1	forest	68.06	0.45	No[1]
ES-LM2	forest	68.06	0.45	No[1]
FI-Hyy	forest	100.00	0.00	Yes
FI-Let	forest	100.00	0.00	Yes
FI-Sii	peatland	90.97	0.16	No[4]
FI-Var	forest	100.00	0.00	Yes
FR-Bil	forest	88.89	0.20	Yes
FR-EM2	crop	96.53	0.07	Yes
FR-Hes	forest	54.86	0.59	No[3]
IT-BCi	crop	47.22	0.57	No[3]
IT-Lsn	crop	75.00	0.38	Yes
IT-SR2	forest	70.14	0.47	No[1]
IT-Tor	grass	72.22	0.40	No[4]
NL-Loo	forest	100.00	0.00	Yes
RU-Fy2	forest	99.31	0.01	Yes
RU-Fyo	forest	100.00	0.00	Yes
SE-Deg	peatland	100.00	0.00	No[4]
SE-Htm	forest	100.00	0.00	Yes
SE-Nor	forest	97.22	0.05	Yes
SE-Ros	forest	100.00	0.00	Yes
SE-Svb	forest	100.00	0.00	Yes

Table A5
Ecosystem and climate zone dimensions were extracted from the related references for 54 sites selected across Europe.

Site	Ecosystem type[1]	Climate zone[2]	Köppen-Geiger classification code	Adopted acronym
BE-Bra	forest	Warm Temperate fully humid warm summer	Cfb	WT-fhws
BE-Lon	crop	Warm Temperate fully humid warm summer	Cfb	WT-fhws
BE-Vie	forest	Warm Temperate fully humid warm summer	Cfb	WT-fhws
CH-Aws	grass	Alpine (polar tundra)	ET	A-pt
CH-Cha	grass	Warm Temperate fully humid warm summer	Cfb	WT-fhws
CH-Dav	forest	Alpine (polar tundra)	ET	A-pt
CH-Fru	grass	Warm Temperate fully humid warm summer	Cfb	WT-fhws
CH-Lae	forest	Warm Temperate fully humid warm summer	Cfb	WT-fhws
CH-Oe2	crop	Warm Temperate fully humid warm summer	Cfb	WT-fhws
CZ-BK1	forest	Boreal (Snow fully humid warm summer)	Dfb	B-sfhws
CZ-Lnz	forest	Warm Temperate fully humid warm summer	Cfb	WT-fhws
CZ-RAJ	forest	Warm Temperate fully humid warm summer	Cfb	WT-fhws
CZ-Stn	forest	Warm Temperate fully humid warm summer	Cfb	WT-fhws
CZ-wet	peatland	Warm Temperate fully humid warm summer	Cfb	WT-fhws
DE-BER	grass	Warm Temperate fully humid warm summer	Cfb	WT-fhws
DE-EC2	crop	Warm Temperate fully humid warm summer	Cfb	WT-fhws
DE-EC4	crop	Warm Temperate fully humid warm summer	Cfb	WT-fhws
DE-Fen	grass	Warm Temperate fully humid warm summer	Cfb	WT-fhws
DE-Geb	crop	Warm Temperate fully humid warm summer	Cfb	WT-fhws
DE-Gri	grass	Warm Temperate fully humid warm summer	Cfb	WT-fhws
DE-Hai	forest	Warm Temperate fully humid warm summer	Cfb	WT-fhws
DE-HoH	forest	Warm Temperate fully humid warm summer	Cfb	WT-fhws
DE-Kli	crop	Warm Temperate fully humid warm summer	Cfb	WT-fhws
DE-Obe	forest	Warm Temperate fully humid warm summer	Cfb	WT-fhws
DE-RbW	grass	Warm Temperate fully humid warm summer	Cfb	WT-fhws
DE-RuR	grass	Warm Temperate fully humid warm summer	Cfb	WT-fhws
DE-RuS	crop	Warm Temperate fully humid warm summer	Cfb	WT-fhws
DE-RuW	forest	Warm Temperate fully humid warm summer	Cfb	WT-fhws
DE-SfS	peatland	Warm Temperate fully humid warm summer	Cfb	WT-fhws
DE-Tha	forest	Warm Temperate fully humid warm summer	Cfb	WT-fhws
DE-ZRK	peatland	Warm Temperate fully humid warm summer	Cfb	WT-fhws
DK-Sor	forest	Warm Temperate fully humid warm summer	Cfb	WT-fhws
ES-Abr	forest	Warm Temperate summer dry hot summer	Csa	WT-sdhs
ES-LM1	forest	Warm Temperate summer dry hot summer	Csa	WT-sdhs
ES-LM2	forest	Warm Temperate summer dry hot summer	Csa	WT-sdhs
FI-Hyy	forest	Boreal (Snow fully humid cool summer)	Dfc	B-sfhcs
FI-Let	forest	Boreal (Snow fully humid warm summer)	Dfb	B-sfhws
FI-Sii	peatland	Boreal (Snow fully humid cool summer)	Dfc	B-sfhcs
FI-Var	forest	Boreal (Snow fully humid cool summer)	Dfc	B-sfhcs
FR-Bil	forest	Warm Temperate fully humid warm summer	Cfb	WT-fhws
FR-EM2	crop	Warm Temperate fully humid warm summer	Cfb	WT-fhws
FR-Hes	forest	Warm Temperate fully humid warm summer	Cfb	WT-fhws
IT-BCi	crop	Warm Temperate summer dry hot summer	Csa	WT-sdhs
IT-Lsn	crop	Warm Temperate fully humid hot summer	Cfa	WT-fhhs
IT-SR2	forest	Warm Temperate summer dry hot summer	Csa	WT-sdhs
IT-Tor	grass	Alpine (polar tundra)	ET	A-pt
NL-Loo	forest	Warm Temperate fully humid warm summer	Cfb	WT-fhws
RU-Fy2	forest	Boreal (Snow fully humid warm summer)	Dfb	B-sfhws
RU-Fyo	forest	Boreal (Snow fully humid warm summer)	Dfb	B-sfhws
SE-Deg	peatland	Boreal (Snow fully humid cool summer)	Dfc	B-sfhcs
SE-Htm	forest	Warm Temperate fully humid warm summer	Cfb	WT-fhws
SE-Nor	forest	Warm Temperate fully humid warm summer	Cfb	WT-fhws
SE-Ros	forest	Boreal (Snow fully humid cool summer)	Dfc	B-sfhcs
SE-Svb	forest	Boreal (Snow fully humid cool summer)	Dfc	B-sfhcs

1. Adapted from (Graf et al., 2020).
2. Extracted from climate zone data (Fig. 4b).

References

Acosta, M., Darenova, E., Dušek, J., Pavelka, M., 2017. Soil carbon dioxide fluxes in a mixed floodplain forest in the Czech Republic. Eur. J. Soil Biol. 82, 35–42.

Allen, R.G., Pereira, L.S., Raes, D., Smith, M., 1998. Crop evapotranspiration: Guidelines for computing crop requirements. In: Irrig. Drain. Pap. No. 56, FAO 300. https://doi.org/10.1016/j.eja.2010.12.001.

Anthoni, P.M., Freibauer, A., Kolle, O., Schulze, E.-D., 2004. Winter wheat carbon exchange in Thuringia, Germany. Agric. For. Meteorol. 121, 55–67.

Aubinet, M., Vesala, T., Papale, D., 2012. Eddy Covariance: A Practical Guide to Measurement and Data Analysis. Springer Science & Business Media.

Aubinet, M., Hurdebise, Q., Chopin, H., Debacq, A., De Ligne, A., Heinesch, B., Manise, T., Vincke, C., 2018. Inter-annual variability of Net Ecosystem Productivity for a temperate mixed forest: a predominance of carry-over effects? Agric. For. Meteorol. 262, 340–353.

Balsamo, G., Beljaars, A., Scipal, K., Viterbo, P., van den Hurk, B., Hirschi, M., Betts, A.K., 2009. A revised hydrology for the ECMWF model: verification from field site to terrestrial water storage and impact in the Integrated Forecast System. J. Hydrometeorol. 10, 623–643.

Bambach, N., Kustas, W., Alfieri, J., Prueger, J., Hipps, L., McKee, L., Castro, S.J., Volk, J., Alsina, M.M., McElrone, A.J., 2022. Evapotranspiration uncertainty at micrometeorological scales: the impact of the eddy covariance energy imbalance and correction methods. Irrig. Sci. 40, 445–461.

Bastiaanssen, W.G.M., Menenti, M., Feddes, R.A., Holtslag, A.A.M., 1998. A remote sensing surface energy balance algorithm for land (SEBAL). 1. Formulation. J. Hydrol. 212, 198–212.

Bayat, B., van der Tol, C., Verhoef, W., 2018. Integrating satellite optical and thermal infrared observations for improving daily ecosystem functioning estimations during a drought episode. Remote Sens. Environ. 209, 375–394. https://doi.org/10.1016/j.rse.2018.02.027.

Bayat, B., van der Tol, C., Yang, P., Verhoef, W., 2019. Extending the SCOPE model to combine optical reflectance and soil moisture observations for remote sensing of ecosystem functioning under water stress conditions. Remote Sens. Environ. 221, 286–301.

Bayat, B., Camacho, F., Nickeson, J., Cosh, M., Bolten, J., Vereecken, H., Montzka, C., 2021. Toward operational validation systems for global satellite-based terrestrial essential climate variables. Int. J. Appl. Earth Obs. Geoinf. 95, 102240.

Bayat, B., Montzka, C., Graf, A., Giuliani, G., Santoro, M., Vereecken, H., 2022. One decade (2011-2020) of European agricultural water stress monitoring by MSG-SEVIRI: Workflow implementation on the Virtual Earth Laboratory (VLab) platform. Int. J. Digit. Earth. https://doi.org/10.1080/17538947.2022.2061617.

Beckers, J.-M., Rixen, M., 2003. EOF calculations and data filling from incomplete oceanographic datasets. J. Atmos. Ocean. Technol. 20, 1839–1856.

Bivand, R., Rundel, C., 2019. rgeos: Interface to Geometry Engine - Open Source ('GEOS'), 2019. R Packag. version 0.5-2. https//CRAN.R-project.org/package=rgeos.

Buysse, P., Bodson, B., Debacq, A., De Ligne, A., Heinesch, B., Manise, T., Moureaux, C., Aubinet, M., 2017. Carbon budget measurement over 12 years at a crop production site in the silty-loam region in Belgium. Agric. For. Meteorol. 246, 241–255.

Carlson, T.N., Capehart, W.J., Gillies, R.R., 1995. A new look at the simplified method for remote sensing of daily evapotranspiration. Remote Sens. Environ. 54, 161–167.

Chi, J., Nilsson, M.B., Kljun, N., Wallerman, J., Fransson, J.E.S., Laudon, H., Lundmark, T., Peichl, M., 2019. The carbon balance of a managed boreal landscape measured from a tall tower in northern Sweden. Agric. For. Meteorol. 274, 29–41.

Chu, H., Luo, X., Ouyang, Z., Chan, W.S., Dengel, S., Biraud, S.C., Torn, M.S., Metzger, S., Kumar, J., Arain, M.A., Arkebauer, T.J., Baldocchi, D., Bernacchi, C., Billesbach, D., Black, T.A., Blanken, P.D., Bohrer, G., Bracho, R., Brown, S., Brunsell, N.A., Chen, J., Chen, X., Clark, K., Desai, A.R., Duman, T., Durden, D., Fares, S., Forbrich, I., Gamon, J.A., Gough, C.M., Griffis, T., Helbig, M., Hollinger, D., Humphreys, E., Ikawa, H., Iwata, H., Ju, Y., Knowles, J.F., Knox, S.H., Kobayashi, H., Kolb, T., Law, B., Lee, X., Litvak, M., Liu, H., Munger, J.W., Noormets, A., Novick, K., Oberbauer, S.F., Oechel, W., Oikawa, P., Papuga, S.A., Pendall, E., Prajapati, P., Prueger, J., Quinton, W.L., Richardson, A.D., Russell, E.S., Scott, R.L., Starr, G., Staebler, R., Stoy, P.C., Stuart-Haëntjens, E., Sonnentag, O., Sullivan, R.C., Suyker, A., Ueyama, M., Vargas, R., Wood, J.D., Zona, D., 2021. Representativeness of Eddy-Covariance flux footprints for areas surrounding AmeriFlux sites. Agric. For. Meteorol. 301–302 https://doi.org/10.1016/j.agrformet.2021.108350.

Colaizzi, P.D., Agam, N., Tolk, J.A., Evett, S.R., Howell, T.A., Gowda, P.H., O'Shaughnessy, S.A., Kustas, W.P., Anderson, M.C., 2014. Two-source energy balance model to calculate E, T, and ET: comparison of Priestley-Taylor and Penman-Monteith formulations and two time scaling methods. Trans. ASABE 57, 479–498.

De Bruin, H.A.R., 1983. A model for the Priestley-Taylor parameter $α$. J. Appl. Meteorol. Climatol. 22, 572–578.

De Bruin, H.A.R., Trigo, I.F., Bosveld, F.C., Meirink, J.F., 2016. Thermodynamically based model for actual evapotranspiration of an extensive grass field close to FAO reference, suitable for remote sensing application. J. Hydrometeorol. 17, 1373–1382. https://doi.org/10.1175/JHM-D-15-0006.1.

Dhungel, R., Allen, R.G., Trezza, R., Robison, C.W., 2014. Comparison of latent heat flux using aerodynamic methods and using the Penman–Monteith method with satellite-based surface energy balance. Remote Sens. 6, 8844–8877.

Domeignoz-Horta, L., Spor, A., Bru, D., Bizouard, F., Leonard, J., Philippot, L., et al., 2015. The diversity of the N2O reducers matters for the N2O: N2 denitrification end-product ratio across an annual and a perennial cropping system. Front. Microbiol. 6, 971.

Droogers, P., Allen, R.G., 2002. Estimating reference evapotranspiration under inaccurate data conditions. Irrig. Drain. Syst. 16, 33–45.

Dušek, J., Č'ižková, H., Stellner, S., Czern`y, R., Květ, J., 2012. Fluctuating water table affects gross ecosystem production and gross radiation use efficiency in a sedge-grass marsh. Hydrobiologia 692, 57–66.

Elbers, J.A., Jacobs, C.M.J., Kruijt, B., Jans, W.W.P., Moors, E.J., 2011. Assessing the uncertainty of estimated annual totals of net ecosystem productivity: a practical approach applied to a mid latitude temperate pine forest. Agric. For. Meteorol. 151, 1823–1830.

El-Madany, T.S., Reichstein, M., Perez-Priego, O., Carrara, A., Moreno, G., Martin, M.P., Pacheco-Labrador, J., Wohlfahrt, G., Nieto, H., Weber, U., et al., 2018. Drivers of spatio-temporal variability of carbon dioxide and energy fluxes in a Mediterranean savanna ecosystem. Agric. For. Meteorol. 262, 258–278.

Elnashar, A., Wang, L., Wu, B., Zhu, W., Zeng, H., 2021. Synthesis of global actual evapotranspiration from 1982 to 2019. Earth Syst. Sci. Data 13, 447–480. https://doi.org/10.5194/essd-13-447-2021.

Emmel, C., Winkler, A., Hörtnagl, L., Revill, A., Ammann, C., D'Odorico, P., Buchmann, N., Eugster, W., 2018. Integrated management of a Swiss cropland is not sufficient to preserve its soil carbon pool in the long term. Biogeosciences 15, 5377–5393.

Ershadi, A., McCabe, M.F., Evans, J.P., Wood, E.F., 2015. Impact of model structure and parameterization on Penman–Monteith type evaporation models. J. Hydrol. 525, 521–535.

Esquinas-Requena, J.L., Lozoya-Moreno, S., Garcia-Nogueras, I., Atienzar-Núñez, P., Sánchez-Jurado, P.M., Abizanda, P., 2020. La anemia aumenta el riesgo de mortalidad debido a fragilidad y discapacidad en mayores: Estudio FRADEA. Aten. Primaria 52, 452–461.

Fischer, M., Trnka, M., Kučera, J., Deckmyn, G., Orság, M., Sedlák, P., Žalud, Z., Ceulemans, R., 2013. Evapotranspiration of a high-density poplar stand in comparison with a reference grass cover in the Czech–Moravian Highlands. Agric. For. Meteorol. 181, 43–60.

Fischer, B., Pau, G., Smith, M., 2019. rhdf5: R Interface to HDF5. R Packag. version 2.30.1 2.

Franz, D., Koebsch, F., Larmanou, E., Augustin, J., Sachs, T., 2016. High net CO 2 and CH 4 release at a eutrophic shallow lake on a formerly drained fen. Biogeosciences 13, 3051–3070.

Gallego-Elvira, B., Olioso, A., Mira, M., Reyes-Castillo, S., Boulet, G., Marloie, O., Garrigues, S., Courault, D., Weiss, M., Chauvelon, P., et al., 2013. EVASPA (EVapotranspiration Assessment from SPAce) tool: an overview. Procedia Environ. Sci. 19, 303–310.

Galvagno, M., Wohlfahrt, G., Cremonese, E., Rossini, M., Colombo, R., Filippa, G., Julitta, T., Manca, G., Siniscalco, C., Di Cella, U.M., et al., 2013. Phenology and carbon dioxide source/sink strength of a subalpine grassland in response to an exceptionally short snow season. Environ. Res. Lett. 8, 25008.

Garcia, M., Fernández, N., Villagarcia, L., Domingo, F., Puigdefábregas, J., Sandholt, I., 2014. Accuracy of the Temperature–Vegetation Dryness Index using MODIS under water-limited vs. energy-limited evapotranspiration conditions. Remote Sens. Environ. 149, 100–117.

Gellens-Meulenberghs, F., Ghilain, N., Arboleda, A., 2012. Land surface evapotranspiration as seen from Meteosat Second Generation Satellites: LSA-SAF developments and perspectives. Int. Geosci. Remote Sens. Symp. 1018–1021 https://doi.org/10.1109/IGARSS.2012.6351228.

Ghilain, N., Arboleda, A., Gellens-Meulenberghs, F., 2011. Evapotranspiration modelling at large scale using near-real time MSG SEVIRI derived data. Hydrol. Earth Syst. Sci. 15, 771–786. https://doi.org/10.5194/hess-15-771-2011.

Ghilain, N., Arboleda, A., Sepulcre-Cantò, G., Batelaan, O., Ardö, J., Gellens-Meulenberghs, F., 2012. Improving evapotranspiration in a land surface model using biophysical variables derived from MSG/SEVIRI satellite. Hydrol. Earth Syst. Sci. 16, 2567–2583.

Ghilain, N., De Roo, F., Gellens-Meulenberghs, F., 2014. Evapotranspiration monitoring with Meteosat Second Generation satellites: improvement opportunities from moderate spatial resolution satellites for vegetation. Int. J. Remote Sens. 35, 2654–2670.

Ghilain, N., Gellens-Meulenberghs, F., Arboleda, A., 2017. Continuous Monitoring of Evapotranspiration (ET) Overview of LSA-SAF Evapotranspiration Products, p. 13. https://doi.org/10.1117/12.2278249.

Ghilain, N., Arboleda, A., Meulenberghs, F., 2018. Validation Report Evapotranspiration & Surface Fluxes (ET & SF v2) PRODUCTS : LSA-311, MET V2. LSA-312 (DMET V2) LSA-304 (MH), LSA-305 (MLE).

Gielen, B., De Vos, B., Campioli, M., Neirynck, J., Papale, D., Verstraeten, A., Ceulemans, R., Janssens, I.A., 2013. Biometric and eddy covariance-based assessment of decadal carbon sequestration of a temperate Scots pine forest. Agric. For. Meteorol. 174, 135–143.

Glenn, E.P., Huete, A.R., Nagler, P.L., Hirschboeck, K.K., Brown, P., 2007. Integrating remote sensing and ground methods to estimate evapotranspiration. CRC. Crit. Rev. Plant Sci. 26, 139–168. https://doi.org/10.1080/07352680701402503.

Glenn, E.P., Nagler, P.L., Huete, A.R., 2010. Vegetation index methods for estimating evapotranspiration by remote sensing. Surv. Geophys. 31, 531–555. https://doi.org/10.1007/s10712-010-9102-2.

Glenn, E.P., Neale, C.M.U., Hunsaker, D.J., Nagler, P.L., 2011. Vegetation index-based crop coefficients to estimate evapotranspiration by remote sensing in agricultural and natural ecosystems. Hydrol. Process. 25, 4050–4062.

Gökmen, M., Vekerdy, Z., Verhoef, A., Verhoef, W., Batelaan, O., van der Tol, C., 2012. Integration of soil moisture in SEBS for improving evapotranspiration estimation under water stress conditions. Remote Sens. Environ. 121, 261–274. https://doi.org/10.1016/j.rse.2012.02.003.

Graf, A., 2017. Gap-filling meteorological variables with Empirical Orthogonal Functions. In: EGU General Assembly Conference Abstracts, p. 8491.

Graf, A., Bogena, H.R., Drüe, C., Hardelauf, H., Pütz, T., Heinemann, G., Vereecken, H., 2014. Spatiotemporal relations between water budget components and soil water content in a forested tributary catchment. Water Resour. Res. 50, 4837–4857.

Graf, A., Klosterhalfen, A., Arriga, N., Bernhofer, C., Bogena, H., Bornet, F., Brüggemann, N., Brümmer, C., Buchmann, N., Chi, J., et al., 2020. Altered energy partitioning across terrestrial ecosystems in the European drought year 2018. Philos. Trans. R. Soc. B 375, 20190524.

Granier, A., Bréda, N., Longdoz, B., Gross, P., Ngao, J., 2008. Ten years of fluxes and stand growth in a young beech forest at Hesse, North-eastern France. Ann. For. Sci. 65, 1.

Grolemund, G., Wickham, H., 2011. Dates and times made easy with lubridate. J. Stat. Softw. 40, 1–25.

Gupta, H.V., Kling, H., Yilmaz, K.K., Martinez, G.F., 2009. Decomposition of the mean squared error and NSE performance criteria: Implications for improving hydrological modelling. J. Hydrol. 377, 80–91. https://doi.org/10.1016/j.jhydrol.2009.08.003.

Haeni, M., Zweifel, R., Eugster, W., Gessler, A., Zielis, S., Bernhofer, C., Carrara, A., Grünwald, T., Havránková, K., Heinesch, B., et al., 2017. Winter respiratory C losses provide explanatory power for net ecosystem productivity. J. Geophys. Res. Biogeosci. 122, 243–260.

Heusinger, J., Weber, S., 2017. Surface energy balance of an extensive green roof as quantified by full year eddy-covariance measurements. Sci. Total Environ. 577, 220–230.

Hommeltenberg, J., Schmid, H.P., Drösler, M., Werle, P., 2014. Can a bog drained for forestry be a stronger carbon sink than a natural bog forest? Biogeosciences 11, 3477–3493.

Hörtnagl, L., Barthel, M., Buchmann, N., Eugster, W., Butterbach-Bahl, K., Diaz-Pinés, E., Zeeman, M., Klumpp, K., Kiese, R., Bahn, M., et al., 2018. Greenhouse gas fluxes over managed grasslands in Central Europe. Glob. Chang. Biol. 24, 1843–1872.

Hoshika, Y., Fares, S., Savi, F., Gruening, C., Goded, I., De Marco, A., Sicard, P., Paoletti, E., 2017. Stomatal conductance models for ozone risk assessment at canopy level in two Mediterranean evergreen forests. Agric. For. Meteorol. 234, 212–221.

Hu, G., Jia, L., Menenti, M., 2015a. Comparison of MOD16 and LSA-SAF MSG evapotranspiration products over Europe for 2011. Remote Sens. Environ. 156, 510–526. https://doi.org/10.1016/j.rse.2014.10.017.

Hu, G., Jia, L., Menenti, M., 2015b. Comparison of MOD16 and LSA-SAF MSG evapotranspiration products over Europe for 2011. Remote Sens. Environ. 156, 510–526. https://doi.org/10.1016/j.rse.2014.10.017.
Jacobs, C.M.J., De Bruin, H.A.R., 1992. The sensitivity of regional transpiration to land-surface characteristics: significance of feedback. J. Clim. 5, 683–698.
Jia, Z., Liu, S., Xu, Z., 2010. Validation of remotely sensed evapotranspiration: a case study. In: 2010 IEEE International Geoscience and Remote Sensing Symposium, pp. 2119–2122.
Jiang, L., Islam, S., 1999. A methodology for estimation of surface evapotranspiration over large areas using remote sensing observations. Geophys. Res. Lett. 26, 2773–2776.
Jocher, G., Marshall, J., Nilsson, M.B., Linder, S., De Simon, G., Hörnlund, T., Lundmark, T., Näsholm, T., Ottosson Löfvenius, M., Tarvainen, L., et al., 2018. Impact of canopy decoupling and subcanopy advection on the annual carbon balance of a boreal scots pine forest as derived from eddy covariance. J. Geophys. Res. Biogeosci. 123, 303–325.
Kiese, R., Fersch, B., Baessler, C., Brosy, C., Butterbach-Bahl, K., Chwala, C., Dannenmann, M., Fu, J., Gasche, R., Grote, R., et al., 2018. The TERENO Pre-Alpine Observatory: integrating meteorological, hydrological, and biogeochemical measurements and modeling. Vadose Zo. J. 17, 1–17.
Klosterhalfen, A., Moene, A.F., Schmidt, M., Scanlon, T.M., Vereecken, H., Graf, A., 2019. Sensitivity analysis of a source partitioning method for H2O and CO2 fluxes based on high frequency eddy covariance data: findings from field data and large eddy simulations. Agric. For. Meteorol. 265, 152–170.
Knoben, W.J.M., Freer, J.E., Woods, R.A., 2019. Technical note: inherent benchmark or not? Comparing Nash-Sutcliffe and Kling-Gupta efficiency scores. Hydrol. Earth Syst. Sci. 23, 4323–4331. https://doi.org/10.5194/hess-23-4323-2019.
Knohl, A., Schulze, E.-D., Kolle, O., Buchmann, N., 2003. Large carbon uptake by an unmanaged 250-year-old deciduous forest in Central Germany. Agric. For. Meteorol. 118, 151–167.
Krupková, L., Marková, I., Havránková, K., Pokorny, R., Urban, O., Šigut, L., Pavelka, M., Cienciala, E., Marek, M.V., 2017. Comparison of different approaches of radiation use efficiency of biomass formation estimation in Mountain Norway spruce. Trees 31, 325–337.
Krupková, L., Havránková, K., Krejza, J., Sedlák, P., Marek, M.V., 2019. Impact of water scarcity on spruce and beech forests. J. For. Res. 30, 899–909.
Kulmala, L., Pumpanen, J., Kolari, P., Dengel, S., Berninger, F., Köster, K., Matkala, L., Vanhatalo, A., Vesala, T., Bäck, J., 2019. Inter-and intra-annual dynamics of photosynthesis differ between forest floor vegetation and tree canopy in a subarctic Scots pine stand. Agric. For. Meteorol. 271, 1–11.
Kurbatova, J., Tatarinov, F., Molchanov, A., Varlagin, A., Avilov, V., Kozlov, D., Ivanov, D., Valentini, R., 2013. Partitioning of ecosystem respiration in a paludified shallow-peat spruce forest in the southern taiga of European Russia. Environ. Res. Lett. 8, 45028.
Kustas, W.P., Norman, J.M., 1999. Evaluation of soil and vegetation heat flux predictions using a simple two-source model with radiometric temperatures for partial canopy cover. Agric. For. Meteorol. 94, 13–29.
Launiainen, S., Katul, G.G., Kolari, P., Lindroth, A., Lohila, A., Aurela, M., Varlagin, A., Grelle, A., Vesala, T., 2016. Do the energy fluxes and surface conductance of boreal coniferous forests in Europe scale with leaf area? Glob. Chang. Biol. 22, 4096–4113.
Li, Z.L., Tang, R., Wan, Z., Bi, Y., Zhou, C., Tang, B., Yan, G., Zhang, X., 2009. A review of current methodologies for regional Evapotranspiration estimation from remotely sensed data. Sensors 9, 3801–3853. https://doi.org/10.3390/s90503801.
Li, S., Wang, G., Sun, S., Chen, H., Bai, P., Zhou, S., Huang, Y., Wang, J., Deng, P., 2018. Assessment of multi-source evapotranspiration products over China using Eddy covariance observations. Remote Sens. 10, 1692. https://doi.org/10.3390/rs10111692.
Li, B., Ryu, Y., Jiang, C., Dechant, B., Liu, J., Yan, Y., Li, X., 2023. BESSv2.0: A satellite-based and coupled-process model for quantifying long-term global land–atmosphere fluxes. Remote Sens. Environ. 295, 113696 https://doi.org/10.1016/j.rse.2023.113696.
Lindroth, A., Holst, J., Heliasz, M., Vestin, P., Lagergren, F., Biermann, T., Cai, Z., Mölder, M., 2018. Effects of low thinning on carbon dioxide fluxes in a mixed hemiboreal forest. Agric. For. Meteorol. 262, 59–70.
Liou, Y.-A., Kar, S.K., 2014. Evapotranspiration estimation with remote sensing and various surface energy balance algorithms—A review. Energies 7, 2821–2849.
Luo, Y., El-Madany, T.S., Filippa, G., Ma, X., Ahrens, B., Carrara, A., Gonzalez-Cascon, R., Cremonese, E., Galvagno, M., Hammer, T.W., et al., 2018. Using near-infrared-enabled digital repeat photography to track structural and physiological phenology in Mediterranean tree–grass ecosystems. Remote Sens. 10, 1293.
Ma, H., Zeng, J., Chen, N., Zhang, X., Cosh, M.H., Wang, W., 2019. Satellite surface soil moisture from SMAP, SMOS, AMSR2 and ESA CCI: a comprehensive assessment using global ground-based observations. Remote Sens. Environ. 231, 111215 https://doi.org/10.1016/j.rse.2019.111215.
Majozi, N.P., Mannaerts, C.M., Ramoelo, A., Mathieu, R., Mudau, A.E., Verhoef, W., 2017. An intercomparison of satellite-based daily evapotranspiration estimates under different eco-climatic regions in South Africa. Remote Sens. 9 https://doi.org/10.3390/rs9040307.
Mammarella, I., Launiainen, S., Gronholm, T., Keronen, P., Pumpanen, J., Rannik, Ü., Vesala, T., 2009. Relative humidity effect on the high-frequency attenuation of water vapor flux measured by a closed-path eddy covariance system. J. Atmos. Ocean. Technol. 26, 1856–1866.
Martens, B., Miralles, D.G., Lievens, H., Van Der Schalie, R., De Jeu, R.A.M., Fernández-Prieto, D., Beck, H.E., Dorigo, W.A., Verhoest, N.E.C., 2017. GLEAM v3: Satellite-based land evaporation and root-zone soil moisture. Geosci. Model Dev. 10, 1903–1925. https://doi.org/10.5194/gmd-10-1903-2017.
Martínez, B., Gilabert, M.A., Sánchez-Ruiz, S., Campos-Taberner, M., García-Haro, F.J., Brümmer, C., Carrara, A., Feig, G., Grünwald, T., Mammarella, I., Tagesson, T., 2020. Evaluation of the LSA-SAF gross primary production product derived from SEVIRI/MSG data (MGPP). ISPRS J. Photogramm. Remote Sens. 159 (February 2019), 220–236.
Mauder, M., Cuntz, M., Drüe, C., Graf, A., Rebmann, C., Schmid, H.P., Schmidt, M., Steinbrecher, R., 2013. A quality assessment strategy for long-term eddy-covariance measurements. Agric. For. Meteorol. 169, 122–135.
McGloin, R., Šigut, L., Havránková, K., Dušek, J., Pavelka, M., Sedlák, P., 2018. Energy balance closure at a variety of ecosystems in Central Europe with contrasting topographies. Agric. For. Meteorol. 248, 418–431.
McNaughton, K.G., Spriggs, T.W., 1986. A mixed-layer model for regional evaporation. Boundary-Layer Meteorol. 34, 243–262.
Menenti, M., 1993. Parameterization of land surface evaporation by means of location dependent potential evaporation and surface temperature range. In: Exch. Process. L. Surf. a Range Sp. Time Scales.
Merlin, O., Chirouze, J., Olioso, A., Jarlan, L., Chehbouni, G., Boulet, G., 2014. An image-based four-source surface energy balance model to estimate crop evapotranspiration from solar reflectance/thermal emission data (SEB-4S). Agric. For. Meteorol. 184, 188–203.
Miralles, D.G., Holmes, T.R.H., De Jeu, R.A.M., Gash, J.H., Meesters, A., Dolman, A.J., 2011. Global land-surface evaporation estimated from satellite-based observations. Hydrol. Earth Syst. Sci. 15, 453–469.
Miralles, D.G., Jiménez, C., Jung, M., Michel, D., Ershadi, A., Mccabe, M.F., Hirschi, M., Martens, B., Dolman, A.J., Fisher, J.B., Mu, Q., Seneviratne, S.I., Wood, E.F., Fernández-Prieto, D., 2016. The WACMOS-ET project - Part 2: Evaluation of global terrestrial evaporation data sets. Hydrol. Earth Syst. Sci. 20, 823–842. https://doi.org/10.5194/hess-20-823-2016.
Moreaux, V., Lamaud, É., Bosc, A., Bonnefond, J.-M., Medlyn, B.E., Loustau, D., 2011. Paired comparison of water, energy and carbon exchanges over two young maritime pine stands (Pinus pinaster Ait.): effects of thinning and weeding in the early stage of tree growth. Tree Physiol. 31, 903–921.
Mu, Q., Zhao, M., Running, S.W., 2011. Improvements to a MODIS global terrestrial evapotranspiration algorithm. Remote Sens. Environ. 115, 1781–1800. https://doi.org/10.1016/j.rse.2011.02.019.
Nagler, P.L., Cleverly, J., Glenn, E., Lampkin, D., Huete, A., Wan, Z., 2005. Predicting riparian evapotranspiration from MODIS vegetation indices and meteorological data. Remote Sens. Environ. 94, 17–30. https://doi.org/10.1016/j.rse.2004.08.009.
Nemani, R.R., Running, S.W., 1989. Estimation of regional surface resistance to evapotranspiration from NDVI and thermal-IR AVHRR data. J. Appl. Meteorol. Climatol. 28, 276–284.
Ney, P., Graf, A., Bogena, H., Diekkrüger, B., Drüe, C., Esser, O., Heinemann, G., Klosterhalfen, A., Pick, K., Pütz, T., et al., 2019. CO2 fluxes before and after partial deforestation of a Central European spruce forest. Agric. For. Meteorol. 274, 61–74.
Nilsson, M., Sagerfors, J., Buffam, I., Laudon, H., Eriksson, T., Grelle, A., Klemedtsson, L., Weslien, P.E.R., Lindroth, A., 2008. Contemporary carbon accumulation in a boreal oligotrophic minerogenic mire–a significant sink after accounting for all C-fluxes. Glob. Chang. Biol. 14, 2317–2332.
Nishida, K., Nemani, R.R., Glassy, J.M., Running, S.W., 2003. Development of an evapotranspiration index from Aqua/MODIS for monitoring surface moisture status. IEEE Trans. Geosci. Remote Sens. 41, 493–501.
Norman, J.M., Kustas, W.P., Humes, K.S., 1995. Source approach for estimating soil and vegetation energy fluxes in observations of directional radiometric surface temperature (vol 77, pg 263, 1995). Agric. For. Meteorol. 80, 297. https://doi.org/10.1016/0168-1923(96)02344-1.
Pastorello, G., Trotta, C., Canfora, E., Chu, H., Christianson, D., Cheah, Y.-W., Poindexter, C., Chen, J., Elbashandy, A., Humphrey, M., et al., 2020. The FLUXNET2015 dataset and the ONEFlux processing pipeline for eddy covariance data. Sci. Data 7 (1), 1–27.
Petropoulos, G.P., Ireland, G., Cass, A., Srivastava, P.K., 2015. Performance assessment of the SEVIRI evapotranspiration operational product: Results over diverse mediterranean ecosystems. IEEE Sensors J. 15, 3412–3423. https://doi.org/10.1109/JSEN.2015.2390031.
Petropoulos, G.P., Ireland, G., Lamine, S., Griffiths, H.M., Ghilain, N., Anagnostopoulos, V., North, M.R., Srivastava, P.K., Georgopoulou, H., 2016. Operational evapotranspiration estimates from SEVIRI in support of sustainable water management. Int. J. Appl. Earth Obs. Geoinf. 49, 175–187. https://doi.org/10.1016/j.jag.2016.02.006.
Pierce, D., 2019. ncdf4: Interface to unidata netCDF (version 4 or earlier) format data files. R Packag. version 1.17. https//CRAN.R-project.org/package=ncdf4, pp. 1–35.
Piles, M., McColl, K.A., Entekhabi, D., Das, N., Pablos, M., 2015. Sensitivity of aquarius active and passive measurements temporal covariability to land surface characteristics. IEEE Trans. Geosci. Remote Sens. 53, 4700–4711. https://doi.org/10.1109/TGRS.2015.2407611.
Post, H., Hendricks Franssen, H.-J., Graf, A., Schmidt, M., Vereecken, H., 2015. Uncertainty analysis of eddy covariance CO 2 flux measurements for different EC tower distances using an extended two-tower approach. Biogeosciences 12, 1205–1221.
Poyda, A., Wizemann, H.-D., Ingwersen, J., Eshonkulov, R., Högy, P., Demyan, M.S., Kremer, P., Wulfmeyer, V., Streck, T., 2019. Carbon fluxes and budgets of intensive crop rotations in two regional climates of southwest Germany. Agric. Ecosyst. Environ. 276, 31–46.
Prescher, A.-K., Grünwald, T., Bernhofer, C., 2010. Land use regulates carbon budgets in eastern Germany: from NEE to NBP. Agric. For. Meteorol. 150, 1016–1025.
Priestley, C.H.B., Taylor, R.J., 1972. On the assessment of surface heat flux and evaporation using large-scale parameters. Mon. Weather Rev. 100, 81–92.

Qiao, D., Li, Z., Zeng, J., Liang, S., McColl, K.A., Bi, H., Zhou, J., Zhang, P., 2022. Uncertainty characterization of ground-based, satellite, and reanalysis snow depth products using extended triple collocation. Water Resour. Res. 58 e2021WR030895.
R Core Team, 2020. R: A language and environment for statistical computing. R Foundation for Statistical Computing, Vienna, Austria. URL: https://www.R-project.org/.
Rinne, J., Tuittila, E.-S., Peltola, O., Li, X., Raivonen, M., Alekseychik, P., Haapanala, S., Pihlatie, M., Aurela, M., Mammarella, I., et al., 2018. Temporal variation of ecosystem scale methane emission from a boreal fen in relation to temperature, water table position, and carbon dioxide fluxes. Glob. Biogeochem. Cycles 32, 1087–1106.
Rubel, F., Brugger, K., Haslinger, K., Auer, I., 2017. The climate of the European Alps: Shift of very high resolution Köppen-Geiger climate zones 1800-2100. Meteorol. Z. 26, 115–125. https://doi.org/10.1127/metz/2016/0816.
Running, S., Mu, Q., Zhao, M., 2021. MODIS/terra net evapotranspiration 8-day L4 global 500m SIN grid V061. In: NASA EOSDIS L. Process. DAAC doi: 10 5067.
Schmidt, W., 1915. Strahlung und Verdunstung an freien Wasserflächen; ein Beitrag zum Wärmehaushalt des Weltmeers und zum Wasserhaushalt der Erde Radiation and evaporation over open water surfaces; a contribution to the heat budget of the world ocean and to the water budge. Ann. Calender Hydrogr. und Marit. Meteorol. 43, 111–124.
Seguin, B., Itier, B., 1983. Using midday surface temperature to estimate daily evaporation from satellite thermal IR data. Int. J. Remote Sens. 4, 371–383.
Simpson, E.H., 1949. Measurement of diversity. Nature 163, 688.
Stoy, P.C., Mauder, M., Foken, T., Marcolla, B., Boegh, E., Ibrom, A., Arain, M.A., Arneth, A., Aurela, M., Bernhofer, C., et al., 2013. A data-driven analysis of energy balance closure across FLUXNET research sites: The role of landscape scale heterogeneity. Agric. For. Meteorol. 171, 137–152.
Su, Z., 2002. The Surface Energy Balance System (SEBS) for estimation of turbulent heat fluxes. Hydrol. Earth Syst. Sci. 6, 85–99. https://doi.org/10.5194/hess-6-85-2002.
Sun, G., Noormets, A., Gavazzi, M.J., McNulty, S.G., Chen, J., Domec, J.-C., King, J.S., Amatya, D.M., Skaggs, R.W., 2010. Energy and water balance of two contrasting loblolly pine plantations on the lower coastal plain of North Carolina, USA. For. Ecol. Manage. 259, 1299–1310.
Szilagyi, J., Parlange, M.B., Katul, G.G., 2014. Assessment of the Priestley-Taylor parameter value from ERA-Interim global reanalysis data. J. Hydro Environ. Res. 2, 1–7.
Taylor, K.E., 2001. in a single diagram. J. Geophys. Res. 106, 7183–7192. https://doi.org/10.1029/2000JD900719.
Temesgen, B., Allen, R.G., Jensen, D.T., 1999. Adjusting temperature parameters to reflect well-watered conditions. J. Irrig. Drain. Eng. 125, 26–33.
Tezza, L., Vendrame, N., Pitacco, A., 2019. Disentangling the carbon budget of a vineyard: the role of soil management. Agric. Ecosyst. Environ. 272, 52–62.
Tramontana, G., Jung, M., Schwalm, C.R., Ichii, K., Camps-Valls, G., Ráduly, B., Reichstein, M., Arain, M.A., Cescatti, A., Kiely, G., Merbold, L., Serrano-Ortiz, P., Sickert, S., Wolf, S., Papale, D., 2016. Predicting carbon dioxide and energy fluxes across global FLUXNET sites with regression algorithms. Biogeosciences 13, 4291–4313. https://doi.org/10.5194/bg-13-4291-2016.
Trigo, I.F., DeBruin, H., 2016. VALIDATION REPORT Reference Evapotranspiration METREF (LSA-303), pp. 1–38.
Trigo, I.F., de Bruin, H., Beyrich, F., Bosveld, F.C., Gavilán, P., Groh, J., López-Urrea, R., 2018. Validation of reference evapotranspiration from Meteosat Second Generation (MSG) observations. Agric. For. Meteorol. 259, 271–285. https://doi.org/10.1016/j.agrformet.2018.05.008.
van den Hurk, B.J.J.M., Viterbo, P., Beljaars, A.C.M., Betts, A.K., 2000. Offline Validation of the ERA40 Surface Scheme. European Centre for Medium-Range Weather Forecasts Reading, UK.
Van Heerwaarden, C.C., de Arellano, J.V.-G., Gounou, A., Guichard, F., Couvreux, F., 2010. Understanding the daily cycle of evapotranspiration: a method to quantify the influence of forcings and feedbacks. J. Hydrometeorol. 11, 1405–1422.
van Meeningen, Y., Wang, M., Karlsson, T., Seifert, A., Schurgers, G., Rinnan, R., Holst, T., 2017. Isoprenoid emission variation of Norway spruce across a European latitudinal transect. Atmos. Environ. 170, 45–57.
Verma, M., Friedl, M.A., Law, B.E., Bonal, D., Kiely, G., Black, T.A., Wohlfahrt, G., Moors, E.J., Montagnani, L., Marcolla, B., Toscano, P., Varlagin, A., Roupsard, O., Cescatti, A., Arain, M.A., D'Odorico, P., 2015. Improving the performance of remote sensing models for capturing intra- and inter-annual variations in daily GPP: an analysis using global FLUXNET tower data. Agric. For. Meteorol. 214–215, 416–429. https://doi.org/10.1016/j.agrformet.2015.09.005.
Vinukollu, R.K., Meynadier, R., Sheffield, J., Wood, E.F., 2011. Multi-model, multi-sensor estimates of global evapotranspiration: climatology, uncertainties and trends. Hydrol. Process. 25, 3993–4010.
Vitale, L., Di Tommasi, P., Arena, C., Riondino, M., Forte, A., Verlotta, A., Fierro, A., De Santo, A.V., Fuggi, A., Magliulo, V., 2009. Growth and gas exchange response to water shortage of a maize crop on different soil types. Acta Physiol. Plant. 31, 331–341.
Wang, K., Dickinson, R.E., 2012. A review of global terrestrial evapotranspiration: observation, modeling, climatology, and climatic variability. Rev. Geophys. 50.
Wang, K., Liang, S., 2008. An improved method for estimating global evapotranspiration based on satellite determination of surface net radiation, vegetation index, temperature, and soil moisture. J. Hydrometeorol. 9, 712–727.
Weerasinghe, I., Bastiaanssen, W., Mul, M., Jia, L., Van Griensven, A., 2020. Can we trust remote sensing evapotranspiration products over Africa. Hydrol. Earth Syst. Sci. 24, 1565–1586. https://doi.org/10.5194/hess-24-1565-2020.
Westerhoff, R.S., 2015. Using uncertainty of Penman and Penman–Monteith methods in combined satellite and ground-based evapotranspiration estimates. Remote Sens. Environ. 169, 102–112.
Wickham, H., 2016. ggplot2: Elegant Graphics for Data Analysis, 2. Springer-Verlag New York, pp. 1–189.
Wickham, H., Averick, M., Bryan, J., Chang, W., McGowan, L., François, R., Grolemund, G., Hayes, A., Henry, L., Hester, J., et al., 2019. Welcome to the tidyverse. J. Open Source Softw. 4, 1686.
Wickham, H., François, R., Henry, L., Müller, K., 2020. dplyr: A Grammar of Data Manipulation. R Packag. version 1.0.2 https//CRAN.R-project.org/package=dplyr.
Wilson, K., Goldstein, A., Falge, E., Aubinet, M., Baldocchi, D., Berbigier, P., Bernhofer, C., Ceulemans, R., Dolman, H., Field, C., et al., 2002. Energy balance closure at FLUXNET sites. Agric. For. Meteorol. 113, 223–243.
Wizemann, H.-D., Ingwersen, J., Högy, P., Warrach-Sagi, K., Streck, T., Wulfmeyer, V., 2015. Three year observations of water vapor and energy fluxes over agricultural crops in two regional climates of Southwest Germany. Meteorol. Z. 24, 39–59.
Wollschläger, U., Attinger, S., Borchardt, D., Brauns, M., Cuntz, M., Dietrich, P., Fleckenstein, J.H., Friese, K., Friesen, J., Harpke, A., et al., 2017. The Bode hydrological observatory: a platform for integrated, interdisciplinary hydro-ecological research within the TERENO Harz/Central German Lowland Observatory. Environ. Earth Sci. 76, 29.
Wu, J., Larsen, K.S., van der Linden, L., Beier, C., Pilegaard, K., Ibrom, A., 2013. Synthesis on the carbon budget and cycling in a Danish, temperate deciduous forest. Agric. For. Meteorol. 181, 94–107.
Wutzler, T., Lucas-Moffat, A., Migliavacca, M., Knauer, J., Sickel, K., Šigut, L., Menzer, O., Reichstein, M., 2018. Basic and extensible post-processing of eddy covariance flux data with REddyProc. Biogeosciences 15, 5015–5030.
Xiao, J., Ollinger, S.V., Frolking, S., Hurtt, G.C., Hollinger, D.Y., Davis, K.J., Pan, Y., Zhang, X., Deng, F., Chen, J., Baldocchi, D.D., Law, B.E., Arain, M.A., Desai, A.R., Richardson, A.D., Sun, G., Amiro, B., Margolis, H., Gu, L., Scott, R.L., Blanken, P.D., Suyker, A.E., 2014. Data-driven diagnostics of terrestrial carbon dynamics over North America. Agric. For. Meteorol. 197, 142–157. https://doi.org/10.1016/j.agrformet.2014.06.013.
Zambrano-Bigiarini, M., 2020. hydroGOF: Goodness-of-fit functions for comparison of simulated and observed hydrological time series. R Packag. version 0.4-0. URL https//github.com/hzambran/hydroGOF. DOI10.5281/zenodo.839854 3.
Zeeman, M.J., Hiller, R., Gilgen, A.K., Michna, P., Plüss, P., Buchmann, N., Eugster, W., 2010. Management and climate impacts on net CO2 fluxes and carbon budgets of three grasslands along an elevational gradient in Switzerland. Agric. For. Meteorol. 150, 519–530.
Zhang, K., Kimball, J.S., Running, S.W., 2016. A review of remote sensing based actual evapotranspiration estimation. Wiley Interdiscip. Rev. Water. https://doi.org/10.1002/wat2.1168.
Zhang, Y., Kong, D., Gan, R., Chiew, F.H.S., McVicar, T.R., Zhang, Q., Yang, Y., 2019. Coupled estimation of 500 m and 8-day resolution global evapotranspiration and gross primary production in 2002–2017. Remote Sens. Environ. 222, 165–182. https://doi.org/10.1016/j.rse.2018.12.031.